

**ULTRAFAST OPTICAL DEVICES FOR PHOTONIC INTEGRATED CIRCUIT
APPLICATIONS**

by

Mingshan Li

B.S., Tsinghua University, 2007

M.S., Tsinghua University, 2009

Submitted to the Graduate Faculty of
Swanson School of Engineering in partial fulfillment
of the requirements for the degree of
Doctor of Philosophy

University of Pittsburgh

2014

UNIVERSITY OF PITTSBURGH
SWANSON SCHOOL OF ENGINEERING

This dissertation was presented

by

Mingshan Li

It was defended on

September 25, 2014

and approved by

Sung Kwon Cho, PhD, Associate Professor, Department of Mechanical Engineering and
Material Science

Mahmoud El Nokali, PhD, Associate Professor, Department of Electrical and Computer
Engineering

Guangyong Li, PhD, Assistant Professor, Department of Electrical and Computer Engineering

William Stanchina, PhD, Chairman and Professor, Department of Electrical and Computer
Engineering

Dissertation Director: Kevin P. Chen, PhD, Associate Professor, Department of Electrical and
Computer Engineering

Copyright © by Mingshan Li

2014

ULTRAFAST OPTICAL DEVICES FOR PHOTONIC INTEGRATED CIRCUIT

APPLICATIONS

Mingshan Li, PhD

University of Pittsburgh, 2014

The transmission bandwidth of a modern fiber-optic communication systems depends on the modulation bandwidth of optical signal transmitters, as well as the computation speed of photonic components for optical signal processing. Nowadays, the rapid development of various bandwidth-hungry network products urges the research on optical transmitters and photonic circuits that could support high bit-rate optical signal communication and computation. The objective of this dissertation is to investigate on laser transmitters that allow ultrafast modulations, as well as on photonic integrated circuits components in nonlinear chalcogenide glass substrates that are capable of ultrafast all-optical signal processing.

Vertical cavity surface emitting lasers (VCSELs) offers superior properties as signal transmitters in the fiber-optic communication network, such as large modulation bandwidth, low coupling loss with optical fibers, and low fabrication cost. As the modulation bandwidth of VCSELs are limited due to their relaxation modulation frequency up to 20GHz, transverse mode lock of VCSEL is proposed to reach modulation bandwidth beyond 100GHz. Both the static emission and ultrafast dynamics of VCSELs' transverse modes were studied to explore their potential for mode locking.

All-optical signal processing with nonlinear photonic integrated circuits (PIC) is an effective solution to overcome the speed limitation arising from opto-electronic conversions in the modern communication network. Performance of individual components in a PIC and its

scale of integration are influenced by its substrate material and its fabrication method. In this dissertation, nonlinear PIC components written in ChG substrates by ultrafast laser writing are studied, taking advantages of the unique material traits of chalcogenide glasses (ChGs), and the capability of ultrafast laser writing to fabricate 3D arbitrary structures in nearly any transparent materials. The fabrication challenges arising from the laser-material interaction were overcome, and basic nonlinear PIC components including waveguide Bragg gratings, nonlinear directional couplers and one dimensional waveguide arrays were designed and fabricated. Functionalities of these devices were demonstrated at a reduced power required for nonlinear operations, as compared to similar devices in silica substrates.

The results presented in this dissertation provide the basics for the realization of on-chip optical network for largely increased data transmission bandwidth and signal processing speed.

TABLE OF CONTENTS

PREFACE.....	XII
1.0 INTRODUCTION.....	1
1.1 MOTIVATIONS.....	1
1.2 PHOTONIC INTEGRATED CIRCUITS.....	2
1.3 ON-CHIP OPTICAL NETWORK.....	4
1.4 OVERVIEW OF THE DISSERTATION.....	6
2.0 ULTRAFAST MODULATION OF VCSEL.....	8
2.1 INTRODUCTION.....	8
2.2 CHARACTERIZATION OF VCSEL MODES.....	10
2.2.1 VCSEL Cavity.....	10
2.2.2 Spatially and Spectrally Resolved VCSEL Modes.....	12
2.2.3 Internal Index Profile of VCSELS.....	15
2.2.3.1 Effective Index Model.....	15
2.2.3.2 Refractive Index Profile of VCSEL.....	16
2.3 ULTRAFAST DYNMAICS OF VCSEL.....	19
2.3.1 LG Modes of VCSELS.....	19
2.3.2 Transverse Mode Lock.....	22
2.3.3 Pump Probe Experiment.....	24
2.4 SUMMARY.....	31

3.0	ULTRAFAST LASER WRITING IN CHALCOGENIDE GLASS.....	32
3.1	CHALCOGENIDE GLASS.....	32
3.1.1	Introduction	32
3.1.2	Material Nonlinearity and Application in All Optical Signal Processing	34
3.2	ULTRAFAST LASER WRITING	35
3.2.1	Background and Mechanism.....	35
3.2.2	Fabrication Challenges in ChG	37
3.2.3	Spatial Beam Shaping	40
3.3	PRELIMINARY TESTS ON CHG WAVEGUIDES.....	40
3.3.1	Temporal Pulse Tuning.....	41
3.3.2	Pulse Propagation in ChG Waveguides.....	43
3.4	MODE COUPLING IN WAVEGUIDE STRUCTURES AND NONLINEAR SWITCHING	45
3.5	SUMMARY	47
4.0	ULTRAFAST SWITCHING WITH WAVEGUIDE BRAGG GRATING	48
4.1	INTRODUCTION	48
4.2	SWITCHING PRINCIPLES	50
4.3	WAVEGUIDE BRAGG GRATING IN CHG	53
4.3.1	Waveguide Bragg Grating Written by Ultrafast Laser	53
4.3.2	Guiding Performance and Grating Transmission	55
4.4	NONLINEAR SWITCHING RESULTS.....	57
4.4.1	Pump Probe Experiment.....	57
4.4.2	Output Signal Modulations	58
4.4.3	Detuning of the Signal Wavelength.....	61
4.5	SUMMARY	63

5.0	NONLINEAR DIRECTIONAL COUPLER.....	64
5.1	INTRODUCTION	64
5.2	NLDC WRITTEN IN CHG SUBSTRATE BY ULTRAFAST LASER	66
5.3	PERFORMANCE OF THE NLDC	69
5.3.1	Insertion Loss.....	69
5.3.2	Nonlinear Switching	70
5.3.3	Spectral and Temporal Changes	72
5.4	SUMMARY	74
6.0	NONLINEAR WAVEGUIDE ARRAYS	75
6.1	INTRODUCTION	75
6.2	PRINCIPLES	77
6.3	WAVEGUIDE ARRAY IN CHG.....	78
6.4	NONLINEAR OPTICAL LOCALIZATION IN WG ARRAY	80
6.4.1	Experiment Setup	80
6.4.2	Nonlinear Localization in ChG WG Array	83
6.4.3	Nonlinear Absorption in ChG WG Array.....	84
6.5	SUMMARY	86
7.0	CONCLUSIONS AND FUTURE WORK	89
	APPENDIX A	92
	BIBLIOGRAPHY	93

LIST OF FIGURES

Figure 1. Example schematic of an on-chip optical network.....	5
Figure 2. Microscope image of the emission window of VCSEL.	10
Figure 3. Estimation of VCSEL’s numerical aperture by linear fitting of its beam sizes with increasing distance.	11
Figure 4. Schematic of the scanning confocal setup.....	12
Figure 5. Optical spectrum at the injection current of 8.5 mA (inset: Intensity pattern, unit of the axes: pixel). Emission peaks (a-f) correspond to transverse modes LG ₀₀ -LG ₀₅	13
Figure 6. Spatial-spectral images of LG ₀₁ , LG ₀₃ -LG ₀₅ modes of an oxide confined VCSEL.	14
Figure 7. Effective refractive index profile of the oxide-confined area of the VCSEL extracted from the spectrally resolved near-field mode images in Figure 6.....	18
Figure 8. Intensity patterns of LG modes with $l = 1, 3-5$, and $p = 0$. For each LG mode, the top row shows the experimental results and the bottom row shows the calculated results.21	21
Figure 9. Circulation of the lasing spot around the VCSEL cavity	23
Figure 10. The emission spectra of VCSEL operating at 1 mA and 7 mA.....	25
Figure 11. Pump probe experiment setup to measure the ultrafast dynamics of VCSEL.	26
Figure 12. Pump-probe experiment results when the VCSEL operates at $I = 1$ mA and $I = 7$ mA respectively.	29
Figure 13. FFT of the time trace after the dissipation of injection energy for VCSEL operate at $I = 7.0$ mA	30
Figure 14. Transverse configuration for ultrafast laser writing.	38
Figure 15. Simulated ChG waveguide cross section without spatial beam shaping.....	38

Figure 16. Ultrafast laser writing setup with spatial beam shaping.	39
Figure 17. Simulated ChG waveguide cross section with spatial beam shaping.	39
Figure 18. Guiding profile at 1040nm of a waveguide written with 300 fs pulse width and its cross section.	42
Figure 19. Guiding profile at 1040nm of a waveguide written with 1.8 ps pulse width and its cross section.	42
Figure 20. Spectral broadening with increasing input intensity.	44
Figure 21. Pulse stretching with increasing input intensity.	45
Figure 22. Microscope images of the WBG: (a) periodic structure; (b) cross section.	54
Figure 23. Near field guiding mode profile of the pump pulses centered at 1040 nm.	55
Figure 24. The measured transmission spectrum of the ChG WBG and simulation.	56
Figure 25. Schematic of the experimental setup using a cross phase modulation scheme.	57
Figure 26. ‘Switch-on’ modulations for probe wavelength at 1551.70nm.	59
Figure 27. ‘Switch-off’ modulations for probe wavelength at 1551.62nm.	59
Figure 28. Probe wavelengths and the WBG bandgap.	60
Figure 29. Modulation depths for the ‘switch-on’ and ‘switch -off’ cases.	60
Figure 30. Dependence of modulation depth and direction on the probe wavelength.	61
Figure 31. Schematic of the nonlinear directional coupler and microscope images of the merging region (inset (a)), and the output facet (inset (b)).	67
Figure 32. Schematic of the experimental setup for NLDC characterization.	68
Figure 33. Mode profiles of an ultrafast laser written waveguide in GLS glass with: (a) p-polarized input; (b) s-polarized input.	69
Figure 34. Output mode profiles and power switching curve for different experiment conditions: input to port 1 (a) p-polarized, (b) s-polarized; input to port 2 (c) p-polarized; (d) s-polarized.	71
Figure 35. (a) Autocorrelation traces of the input pulse and output pulses from the two coupler channels with the peak intensity of the input being 90 GW/cm ² . (b, c) Spectral evolution of the two coupler outputs, (b) Bar; (c) Cross. The input is p-polarized and	

coupled to port 2 of the NLDC. Each trace in the spectra is marked with the corresponding input peak intensity (unit: GW/cm ²).	73
Figure 36. Microscope images of (a) the output facet of the waveguide array; (b) the top view of the array structure; (c) symmetric waveguide cross section formed with a shaped writing beam; (d) elongated waveguide cross section formed with an un-shaped writing beam. Scale bar in (c) and (d): 10 μm.	79
Figure 37. Schematic of the experiment setup for characterization of WG array.	80
Figure 38. Guided mode profiles of an individual waveguide (a) formed with spatially shaped writing beam; (b) formed with un-shaped writing beam.	81
Figure 39. (a) Autocorrelation traces and (b) output spectra of individual waveguide outputs with input pulse energies of 2nJ and 10nJ.	82
Figure 40. Measured output patterns of the ChG waveguide array with various input peak power.	84
Figure 41. Fractional powers of outputs from ChG waveguide array. (a) Measured results; (b) Simulated results with two photon absorption; (c) Simulated results without two photon absorption.....	88

PREFACE

I am very grateful for the tremendous help and financial support from Professor Kevin P. Chen. His patient guidance and expertise in photonics has led me through my PhD study, without which none of the work in this thesis would have been possible.

I'd like to thank Dr. Sung Kwon Cho from Department of Mechanical Engineering, Dr. Mahmoud El Nokali, Dr. Guangyong Li and Dr. William Stanchina from our department for joining my PhD dissertation committee.

Many thanks to Professor Hrvoje Petek, Professor David Snoke and Dr. Albert Heberle for their help and suggestions.

I would also like to express my gratitude to my colleagues in the lab, Rongzhang Chen, Sheng Huang, Aidong Yan, Dr. Qingqing Wang, Dr. Tong Chen, Dr. Ben McMillen, Dr. Chuck Jewart, Dr. Brian Nelson, and Dr. Botao Zhang, for the great help and inspiring discussions all along.

Last but not least, I could not have finished this important journey of my life without the love, care, support and encouragement from my friends and my family.

1.0 INTRODUCTION

The aim of this dissertation is to provide the basics for realization of an on-chip optical network capable of high-bit-rate signal transportation. It integrates a fast modulated laser source, together with other elements for all-optical signal processing. To aid in this goal, this dissertation respectively investigate into the ultrafast modulation of vertical cavity surface-emitting lasers (VCSEL) and the fabrication of optical waveguide components in nonlinear materials by ultrafast laser writing. This chapter includes an introduction to integrated lightwave circuits and an overview of the dissertation outline.

1.1 MOTIVATIONS

Modern information network thrives from optical fiber communication technology, which has evolved rapidly in the past few decades and reached single channel line rates of up to terabit per second both in research [1, 2] and in practice [3], or even petabit per second line rates in multicore fiber channels [4-6]. In these network systems, optical fibers have served as the links among network elements and have allowed high bit-rate data transportation in the form of modulated optical carrier waves. However, nowadays these high-capacity optical channels are usually fed with lower-bitrate signals generated and processed by integrated circuit (IC) devices. These electronic devices fulfill essential functionalities in the communication network, such as

signal monitoring and tracking, data stream switching, network, as well as fault detection and protection to prevent service outages. However, IC devices also have limitations which are becoming more and more notable, with the fast growing demands on data transmission bandwidth and signal processing speed. Firstly, the cost of optical-electrical-optical (OEO) conversion scales with the capacity of the communication network; Secondly, signal integrity degrades and signal intensity seriously attenuates at high bit rates $> 10\text{Gb/s}$ [7, 8]. The cost and deteriorated performance of IC devices with increasing transmission bitrates have become an obstacle in the further development of modern communication network.

Photonic integrated circuit (PIC) is a straight forward solution to deal with this situation. With a few or even many optical components integrated on a single substrate, PIC devices can fulfill functionalities as their IC counterparts. Meanwhile, as the OEO conversion is eliminated, PIC devices can be much more cost-effective in network systems with large transmission capacity. The implementation of PIC devices could effectively increase the bandwidth limit of the communication network while retaining advantages such as compactness, robustness, and stability.

1.2 PHOTONIC INTEGRATED CIRCUITS

Photonic integrated circuits (PICs) are formed with optical components integrated in a single substrate. Optical waveguides are the key elements in PICs. Their functionalities are not limited to optical guiding, but also manipulations of optical signals governed by their structural characteristics. A wide range of optical components can be formed based on optical waveguides, such as power splitters, directional couplers, Bragg gratings, sources, detectors, and etc. These

optical components are basic elements in a PIC, and they can be used as functional blocks to build more complex photonic circuits with a wide range of functions to accommodate different application needs.

PIC devices provides larger transmission bandwidth and higher processing speed as compared to IC electronic devices. Their advantages over free-space and fiber optics are also prominent, including availability for high-volume and low cost fabrication by sharing tools in IC manufacturing, compact and light-weight devices with integration of optical components, and alignment free operations and stable performance with fixed chip-scale optical components.

Integrated photonics have experience a long history of development since the first planar optical waveguide fabricated at the end of 1960s [9]. In more than half a century, PIC devices have evolved from simple optical waveguides to integration of many optical components. Aiming at different fabrication requirements, device functionalities, and material properties, PIC devices have been demonstrated in a variety of the material systems, including lithium niobate (LiNbO_3) [10], Indium Phosphide (InP) [11], Silicon (Si) [12, 13] , and Silica-on-Silicon [14]. These PIC devices are usually two dimensional planar structures due to the limitations of available fabrication methodologies. Photonic waveguide structures in micrometer scales [8] are generally obtained by photolithography, with the detailed fabrication process varied among substrate materials.

Large scale integration of photonic components in a single substrate is an inevitable trend of PIC development. Reduction in structure feature sizes is a straight forward solution for device miniaturization and dense integration, then high refractive index materials are required and feature sizes are within diffraction limits. Another way to large scale integration is to expand the integration or structure dimension. However, with photolithographic fabrication, extra efforts in

layer alignments are required to make three dimensional (3D) circuit structures, resulting in additional cost and difficulty in 3D fabrication to expand the dimension of integration. Ultrafast laser writing [15] is a new micro-fabrication technique that shows significant superiority over conventional photolithography-based methods in 3D material processing [16], and its application in fabricating both photonics and MEMS structures in a large variety of transparent materials are under extensive research. A more detailed introduction to the ultrafast laser writing technique will be provided in Chapter 3.

1.3 ON-CHIP OPTICAL NETWORK

The fast development of PIC industry and their applications in optical communication network is driven by increasing demands for broader optical bandwidth and faster signal processing speed. With optical fibers serving as the links for data transportation, and through the integration of basic functional blocks for generation, processing, and detection of optical signals, an on-chip optical networks can be built with PICs. Optical network elements with PIC components integrated in a single chip have been reported to support data rates up to 500 Gb/s [17]. While this high data rate is achieved by multiplexing of several signal streams, and manipulations of optical signal in these network systems have been realized by electro-optic effects, further increased data rates can be expected by using all optical signal processing schemes.

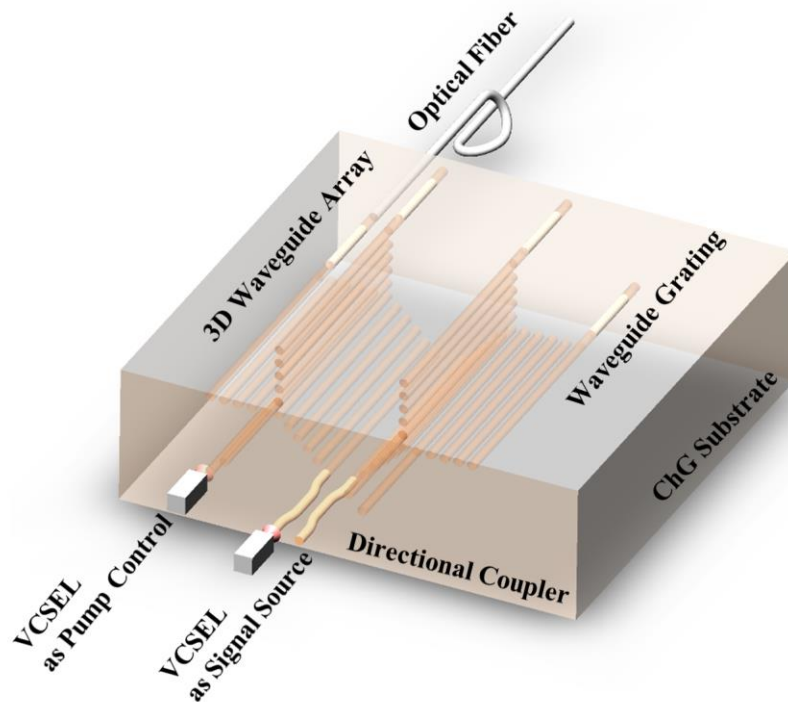


Figure 1. Example schematic of an on-chip optical network.

The basic idea for all optical signal processing is to use light to control light, which is only possible through the χ_3 nonlinear optical properties of materials. Operations in these optical structures are triggered by input intensity levels, and the required intensity level and hence power consumption for the nonlinear operation can be reduced by careful design of the optical structures, as well as by using substrate materials with large nonlinear refractive indices and low nonlinear absorptions. Of all the substrate materials that have been studied for nonlinear optical devices, chalcogenide glasses presents superior nonlinearity and also some other material traits that make it stand out in this application. In this dissertation, chalcogenide glasses are used as substrate materials and nonlinear optical components are fabricated by ultrafast laser writing.

Figure 1 shows an example of an on-chip optical network with a photonic integrated circuit chip that modulates and outputs signals to an optical fiber. In this simplified transmitter, an external laser source (VCSEL) provides optical signal at high bit rates as input to the chip. And photonic structures are integrated in this chalcogenide glass chip for all optical signal processing, with high intensity pump controls that steer optical signals to the selected output ports.

1.4 OVERVIEW OF THE DISSERTATION

This dissertation describes an on-chip optical network with a high data-rate optical transmitter and the photonic lightwave circuit for all-optical signal processing. The optical transmitter is a transverse mode-locked vertical cavity surface emitting laser (VCSEL) that produces optical signal with bit rates beyond 100 Gb/s, while the photonic lightwave circuit consist of nonlinear PIC components fabricated by ultrafast laser writing in highly nonlinear materials. These two parts of the network system are investigated independently in this dissertation, serving as the fundamentals to build the integrated optical network on-chip.

The dissertation is organized as follows.

Chapter 2 investigates the ultrafast dynamics of vertical cavity surface emitting laser (VCSEL). The static emission of the VCSEL and its ultrafast dynamics upon injections of the ultrafast laser pulses are measured. Conditions for transverse mode locking VCSEL are discussed.

Chapter 3 through chapter 6 investigates chalcogenide photonic integrated circuit components that are fabricated by ultrafast laser writing. Chapter 3 first gives a brief introduction

to the ultrafast laser writing technique, the chalcogenide glass that is used as the device substrate in the work, and the challenge of its processing due to the large nonlinearity. Preliminary test results on the ultrafast laser written waveguides in the chalcogenide glass are presented.

Chapter 4 introduces a nonlinear switch based on an ultrafast laser written Bragg grating in chalcogenide glass. A pump probe experiment is carried out to study the power switching of the probe output by injection of ultrafast pump pulses. Nonlinear switching is influenced by both the pump power and the detuning of probe wavelength from the grating's resonant wavelength.

Chapter 5 presents a nonlinear directional coupler written by ultrafast laser. Power switching between the two coupler outputs is demonstrated with reduced input power compared to devices in silica. Both the spectral and temporal change of the ultrafast laser pulse propagated through the coupler are studied.

Chapter 6 focuses on a one dimensional nonlinear waveguide array written by ultrafast laser. With the optimized configuration of the waveguide array, spatial soliton formation is studied, and the effects of nonlinear absorption are also considered.

Chapter 7 discusses possible directions for future research and summarizes the dissertation.

2.0 ULTRAFAST MODULATION OF VCSEL

Vertical cavity surface emitting lasers are investigated in the chapter as the high bit-rate signal sources in the on-chip optical network. The static emission of VCSEL transverse modes are first measured, and its internal index profile is extracted based on these experiment results. With the internal structures of the VCSEL obtained, a set of Laguerre-Gaussian modes is simulated and discussions on their transverse mode locking are made. The ultrafast dynamics of VCSEL is also studied by a pump probe experiment and synchronization of VCSEL transverse modes are achieved.

2.1 INTRODUCTION

Semiconductor lasers are one of the successful examples of the integration of photonic lightwave circuits and electronic circuits, and it is also one of the essential components in optical communication systems [18]. Vertical cavity surface emitting lasers (VCSEL) are semiconductor lasers whose emission direction is perpendicular to the active region, different from conventional edge emitting semiconductor lasers, where laser emissions are in the planes of active regions. Some appealing characteristics arise from this unique structural configuration of VCSELs, such as single longitudinal mode operation, on-die testing, and the possibility for dense two-dimensional integration [19]. For applications in optical communication in particular, VCSELs

are attractive devices owing to their larger modulation bandwidth [20-23]. However, the relaxation modulation frequency up to 20GHz [24-26] sets the limit for the bandwidth of direct modulated VCSELs.

Another option for high speed optical transmitters are mode-locked semiconductor lasers that produce short pulses at high repetition rates. The laser cavities of mode-locked devices are relatively long so as to support multiple longitudinal modes in equidistant spacing and short pulse generations are achieved by phase locking of these modes. As the lasing cavity of VCSEL is formed by the back and front distributive Bragg reflectors that are usually λ or 1.5λ apart, VCSELs supports only one longitudinal mode, making it impossible of longitudinal mode locking. However, the large transverse area of the laser cavity results in multiple transverse mode emission. Moreover, a VCSEL with parabolic index profile can support Laguerre-Gaussian transverse modes that are equally spaced with appropriate driving currents and set temperatures [27]. In this case, the transverse modes of VCSEL can be locked to enable short pulse emission by synchronizing the phase of the equidistant modes. As the transverse mode spacing of VCSEL is usually about 0.2 nm, for a VCSEL operating at around 800 nm, this mode spacing suggests a repetition rate over 100 GHz, which is a great enhancement of the direct modulation of state-of-the-art VCSELs.

In this chapter, we demonstrate the transverse mode-locking VCSEL by studying its ultrafast switching dynamics. To that end, the transverse modes of VCSEL are first characterized and its internal refractive index profile is extracted.

2.2 CHARACTERIZATION OF VCSEL MODES

2.2.1 VCSEL Cavity

A commercially available oxide-confined multimode VCSEL with center emission wavelength at 850 nm is used in the experiment. The threshold current is 1.8 mA at 25 °C and its slope efficiency is 0.3 mW/mA. The oxide aperture of the VCSEL is 14 μm in diameter. Figure 2 shows the microscope image of the VCSEL's emission window.

The numerical aperture (NA) of this VCSEL is estimated by measuring its output beam divergence. The far field mode patterns are measured at increasing propagation distances. By fitting the beam sizes at different distances, NA of the VCSEL under test is found to be 0.21 (Figure 3). Assuming that the VCSEL cavity can be treated as a step-index waveguide, the effective index step was estimated by $\delta n = 0.0063$, given the refractive index of the AlGaAs active area $n_0 = 3.5$.



Figure 2. Microscope image of the emission window of VCSEL.

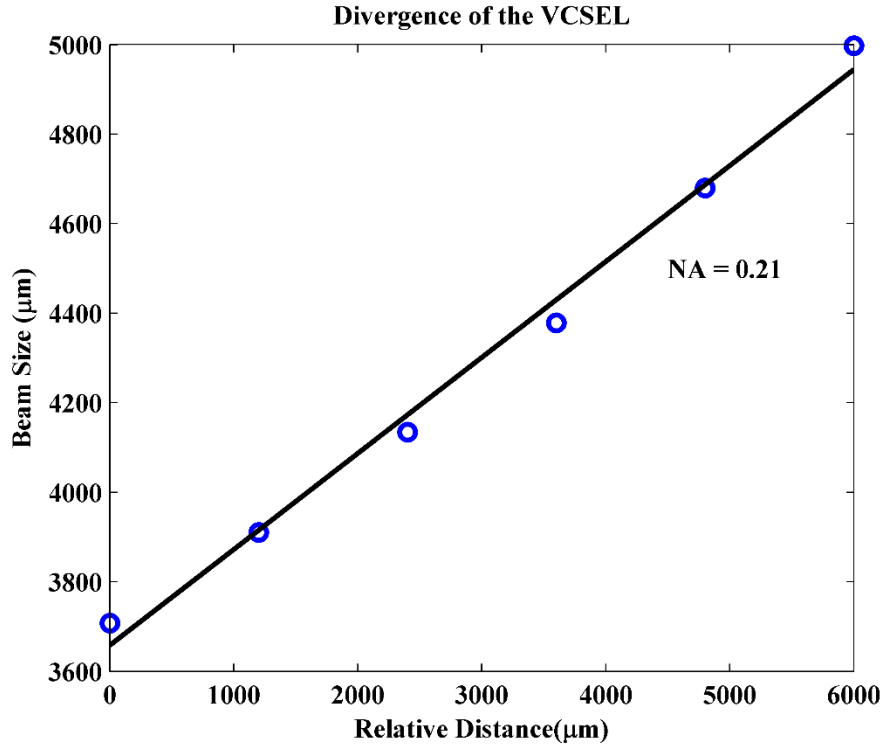


Figure 3. Estimation of VCSEL’s numerical aperture by linear fitting of its beam sizes with increasing distance.

A scanning confocal microscope with an optical spectrum analyzer (OSA) is used to obtain spectrally resolved near-field images of the VCSEL transverse modes. Figure 4 shows the schematic of the experimental setup. The VCSEL under test is driven by a constant injection current of 8.5 mA and its temperature is maintained at 25 °C. It is mounted on a 3-axis stage that scans the VCSEL in the plane of its emission window with a spatial resolution of 1 μm. The laser emission is collected by a 20X microscope objective (NA = 0.4, f = 10 mm). With the collimated beam collected and magnified by another lens (f = 30 cm), the VCSEL transverse modes are projected onto a CMOS camera (5.2 μm/pixel). The magnification of this imaging system is calibrated to be 27X. A clear image of VCSEL’s emission window is first obtained to determine the plane of scanning (Figure 2). A single mode fiber (Corning SMF-28) connected to an optical

spectrum analyzer (OSA) is used to probe the image plane, so that the 9- μm fiber core works as a pin hole in the confocal microscope. The VCSEL emission window is scanned with a 1- μm step size in a 20 $\mu\text{m} \times 20 \mu\text{m}$ area in the object plane, corresponding to a 540 $\mu\text{m} \times 540 \mu\text{m}$ area with a 27- μm pixel size in the image plane. At each scanning point, the OSA acquires the emission spectrum of 1001 points in a 5-nm bandwidth.

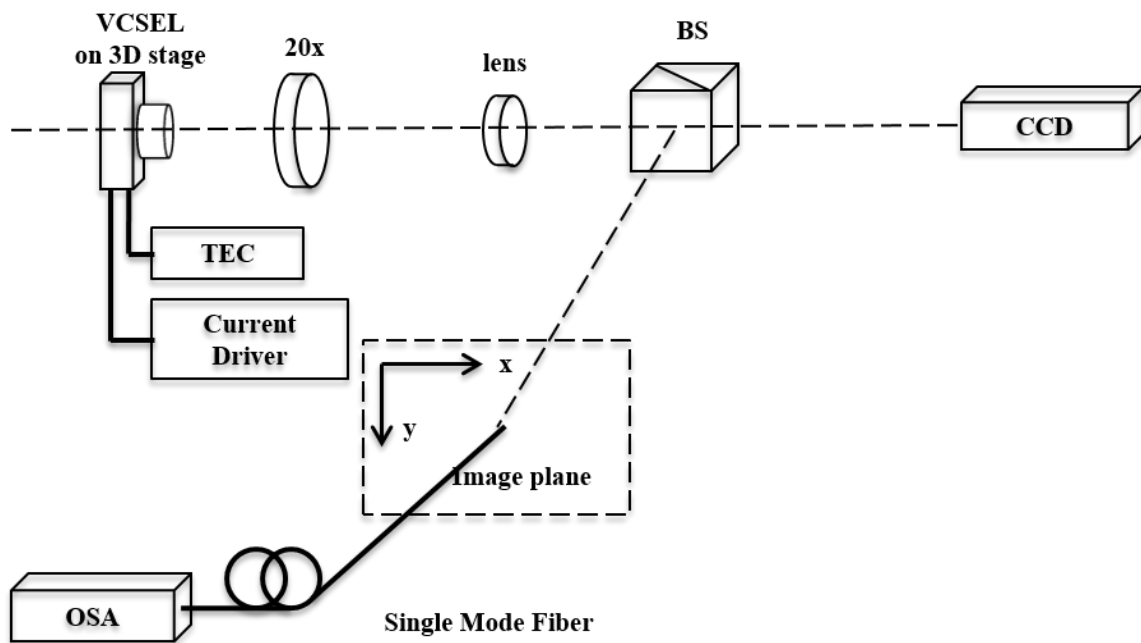


Figure 4. Schematic of the scanning confocal setup

2.2.2 Spatially and Spectrally Resolved VCSEL Modes

Figure 5 (inset) shows an intensity pattern of VCSEL operating with 8.5 mA injection current at 25 $^{\circ}\text{C}$. The intensity pattern is a superposition of all the transverse modes supported by VCSEL at this operating condition. The emission spectrum is also shown in Figure 5, with each peak in

the figure corresponding to a lasing transverse mode of this VCSEL. The lasing peaks to be considered in this experiment are marked in the VCSEL spectrum.

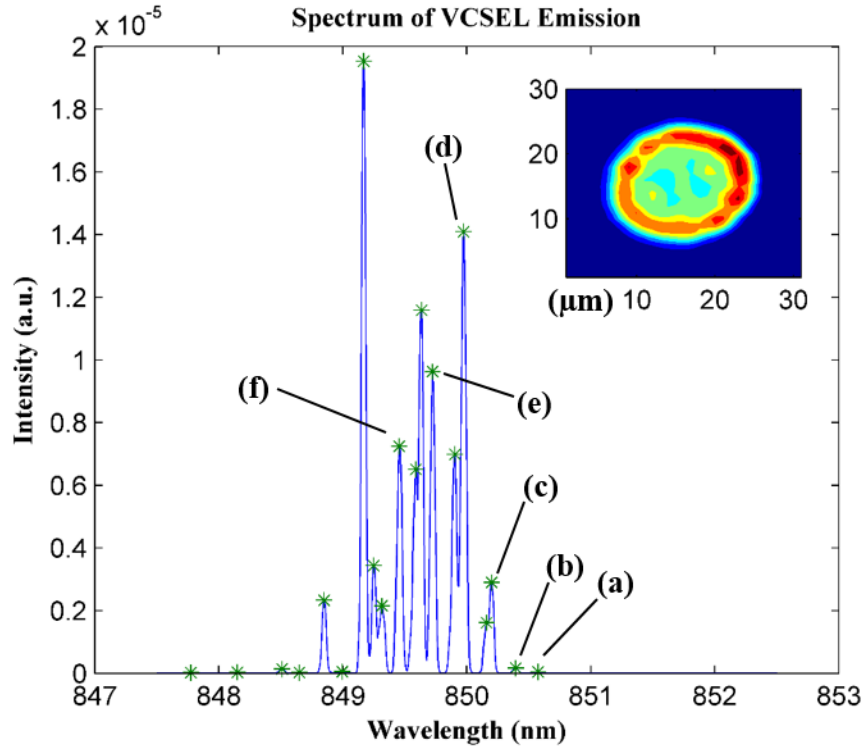


Figure 5. Optical spectrum at the injection current of 8.5 mA (inset: Intensity pattern, unit of the axes: pixel). Emission peaks (a-f) correspond to transverse modes LG_{00} - LG_{05} .

To resolve individual transverse modes of the VCSEL with respect to its emission wavelengths, mode patterns at each wavelength are reconstructed with the collected spectra at each scanning point. Emission peaks at each point were identified and plotted. Figure 6 shows the mode patterns that associate with intensity peaks (b, d-f) in Figure 5. Since these mode patterns are similar to those of Laguerre-Gaussian (LG) modes, which are circularly symmetric

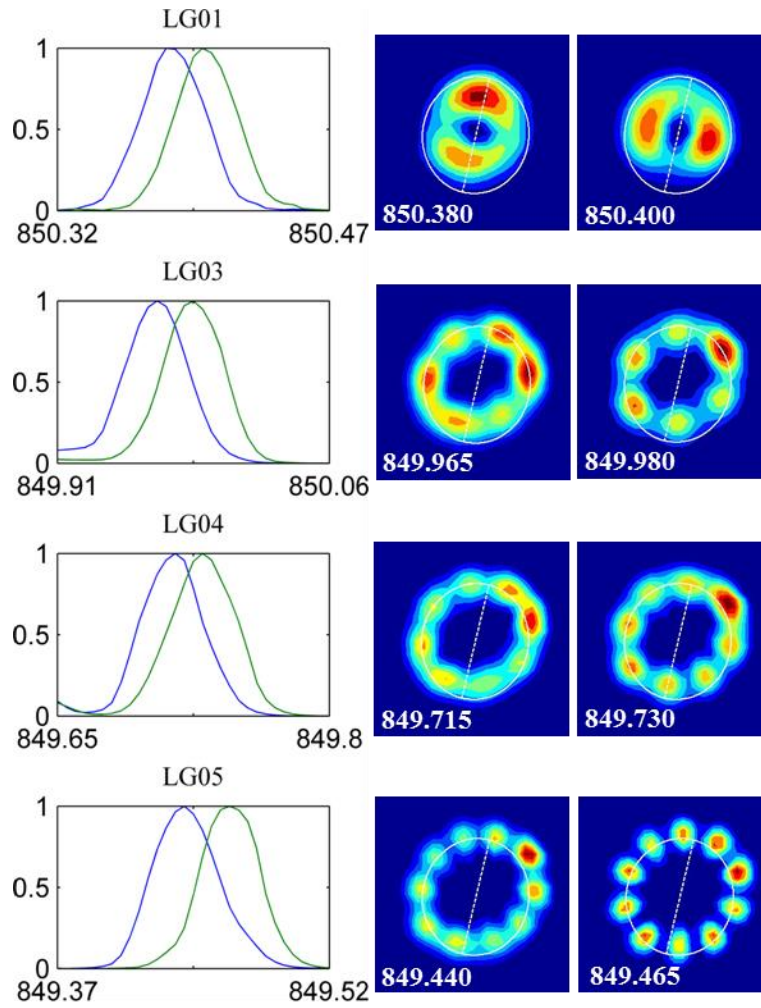


Figure 6. Spatial-spectral images of LG₀₁, LG₀₃-LG₀₅ modes of an oxide confined VCSEL.

emission patterns from a parabolic index profile, for approximate representations, they are described as LG modes with azimuthal indices $l = 1, 3-5$, and radial mode number $p = 0$. The mode spacing of these LG modes are about 0.2 nm. The intensity peaks that are not designated are high order LG modes with radial mode number $p > 0$. These modes are not considered here since mode degeneracy is not obvious for these modes.

For a circularly symmetric VCSEL structure, LG modes of the same order each support two degenerate modes with the same emission wavelength, and similar mode patterns in different orientations. The near-field emission pattern of degenerate LG modes for the VCSEL under test are shown in Figure 6 (right). These experimental results reveal the breakdown of degeneracy, as each pair of the degenerate LG modes show small splitting in emission wavelength, as shown in Figure 6 (left). The splitting is about 0.02 nm, much smaller than the 0.2 nm mode spacing. The mode splitting was further confirmed by the spectrally resolved near-field emission patterns shown in Figure 6 (right) for transverse modes $LG_{01}, LG_{03}-LG_{05}$.

2.2.3 Internal Index Profile of VCSELs

2.2.3.1 Effective Index Model

The effective index model has been widely used to simplify complex problems in waveguide optics and proved to be successful. Since the cavity of an oxide-confined VCSEL is formed by the top and bottom distributed Bragg reflectors as longitudinal confinement, and by an oxidized aperture as transverse confinement, for analysis of supported modes by the cavity, the internal structure of VCSEL can be equivalent to an optical waveguide, with the active area as waveguide core, and the oxidized layer as cladding. Thus the relation between the internal effective index profile of the VCSEL and its mode wavelengths are described by [28],

$$\frac{\Delta n_m}{\Delta \lambda_m} = \frac{n_{ref}}{\lambda_{ref}} \quad (2.1)$$

where n_{ref} is a reference effective index corresponding to the reference wavelength λ_{ref} , Δn_m is the effective index change of VCSEL mode m with respect to n_{ref} , and $\Delta \lambda_m$ is its wavelength change with respect to λ_{ref} .

The effective index of each VCSEL mode, which is a weighted average of the internal refractive index profile $n(x,y)$ by its intensity distribution $I(x,y)$, can be obtained based on its intensity pattern,

$$n_m = \frac{\int I(x,y)n(x,y)dxdy}{\int I(x,y)dxdy} \quad (2.2)$$

As we have obtained the intensity patterns and wavelengths associated with each transverse modes in the previous section, we are able to find out the refractive index profile $n(x,y)$ from the above equations by numerical fitting, given the geometry of VCSEL's emission aperture and model of its index profile.

2.2.3.2 Refractive Index Profile of VCSEL

From the experiment results, the splitting of degenerate LG modes suggests that the oxide-defined aperture of the VCSEL under test is not circular. This can be attributed to the asymmetric oxidation rate observed along different crystalline directions [29]. To explain the observed LG mode splitting shown in Figure 6, an elliptical index profile should be considered. For an operating device, it's also necessary to take into account the temperature effects. A parabolic profile is therefore superposed across the active region. Using the second-order Taylor approximation of the refractive index model of quadratic-index media [30], the internal index profile of VCSEL is described,

$$n(x, y) = \begin{cases} n_0(1 + \frac{1}{2}g^2) - \frac{1}{2}g^2n_0(\frac{x^2}{a^2} + \frac{y^2}{b^2}) & \frac{x^2}{a^2} + \frac{y^2}{b^2} \leq 1 \\ n_0 - \delta n_0 & \frac{x^2}{a^2} + \frac{y^2}{b^2} > 1 \end{cases} \quad (2.3)$$

where δn_0 is the index step at the edge of the oxide aperture, and g is a fitting parameter to include the temperature effects.

To find the elliptical parabolic index profile, numerical fitting is started from using a circular step index model ($a = b, g = 0$), where ($a, \delta n$) are the parameters to be determined. Based on the optimized result in the circular step model, another fitting with the elliptical step model is followed to find the fitting parameters ($a, b, \delta n$), where a, b are the semi-major and minor axes respectively, and δn is the index step. When the elliptical step model is determined, the fitting parameter g is added so that the elliptical parabolic index profile can be obtained. The numerical fitting results show that $a = 6.89 \mu m, b = 6.15 \mu m, \delta n = 0.0058, g = 0.0269$. The correlation coefficient and the RMS error for the fitting using the elliptical step-index model are respectively 0.9994 and 1.4562×10^{-5} .

The internal refractive index distribution of this oxide confined VCSEL is most accurately described by an elliptical parabolic profile. The calculated elliptical parabolic index profile is shown in Figure 7. The temperature induced parabolic refractive index profile on top of the index step peaks at the center of the VCSEL with 1.27×10^{-3} above the step index. This value is consistent with the carrier dynamics of oxide-guiding VCSELs. When temperature effects are included, the calculated effective index step is reduced, while the total guiding inside the VCSEL cavity is unchanged. These calculation results suggest that non-uniform temperature distribution attributes to laser guiding inside the VCSEL cavity, which is consistent with previous reports [31, 32].

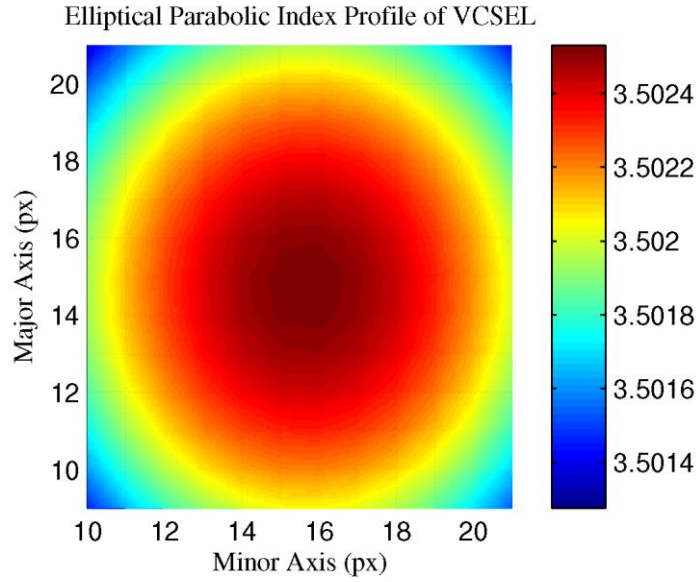


Figure 7. Effective refractive index profile of the oxide-confined area of the VCSEL extracted from the spectrally resolved near-field mode images in Figure 6.

The most important feature resulted from the elliptical index profile is the degenerate mode splits, which cannot be explained with the circular index model. A simulation of field distributions and effective refractive indices of different modes for the elliptical parabolic index profile obtained above is carried out by a commercial finite element solver COMSOL. The effective index difference between the two degenerate modes of LG_{01} is 8.7×10^{-5} , which corresponds to a wavelength difference of 0.021 nm. This is consistent with the observed splitting of 0.02 nm.

2.3 ULTRAFAST DYNMAICS OF VCSEL

2.3.1 LG Modes of VCSELS

By measuring the spatially and spectrally resolve mode patterns of an oxide-confined multimode VCSEL, we find that an index profile with a step-like index change at the oxide aperture and a parabolic profile in the active area best describes the internal index distribution of the VCSEL under test. The parabolic profile is induced from the thermal gradient due to carrier heating when the device is operating above threshold current, thus it is an intrinsic characteristic of the index profile of a running VCSEL. However, as this cylindrical asymmetry of the VCSEL cavity arises from the anisotropic lateral oxidation rate in $\text{Al}_x\text{Ga}_{1-x}\text{As}$, the strain induced by different fabrication steps, as well as material birefringence, the ellipticity of the oxide aperture could vary from device to device. Hence, for a general case, we consider the transverse modes of a VCSEL with a circular step-like index change at the oxide aperture and a parabolic profile in the active area, and such an index profile is described by,

$$n(x, y) = \begin{cases} n_0(1 + \frac{1}{2}g^2) - \frac{1}{2}\frac{g^2n_0}{a^2}(x^2 + y^2) & x^2 + y^2 \leq a^2 \\ n_0 - \delta n_0 & x^2 + y^2 > a^2 \end{cases} \quad (2.4)$$

where $n_0 = 3.5$ is the refractive index of the active area, a is the radius of the oxide aperture, δn_0 is the index step at the edge of the oxide aperture, and g is a fitting parameter to include the temperature effects. Using this model to calculate the internal index profile of the VCSEL tested in the previous section, the best numerical fitting results shows that $a = 6.52 \mu\text{m}$, $\delta n = 0.0058$, and $g = 0.0269$.

To find out the supported modes of a VCSEL with an refractive index profile described above, we consider an even simpler case: light propagation in the medium with parabolic index profile, i.e.

$$n(x, y) = n_0 \left(1 + \frac{1}{2} g^2 \right) - \frac{1}{2} \frac{g^2 n_0}{a^2} \rho^2, \rho^2 = x^2 + y^2 \quad (2.5)$$

So the Helmholtz equation in cylindrical coordinate becomes,

$$\frac{\partial^2 E}{\partial \rho^2} + \frac{1}{\rho} \frac{\partial E}{\partial \rho} + \frac{1}{\rho^2} \frac{\partial^2 E}{\partial \phi^2} + \frac{\partial^2 E}{\partial z^2} + k_0^2 \left[n_1^2 - n_1 n_2 \frac{\rho^2}{a^2} \right] E = 0 \quad (2.6)$$

where $n_1 = n_0 \left(1 + \frac{g^2}{2} \right)$, $n_2 = n_0 g^2$, and the fourth order term of g is neglected, given $g \ll 1$. The expected laser modes in this case are Laguerre-Gauss (LG) modes. Corresponding to the experiment results shown in the previous section, we consider only the LG modes with azimuthal indices $l = 1, 2, 3, \dots$ and radial mode number $p=0$. The normalized intensity pattern of these LG modes are [33],

$$I_{0l}(r, \theta) = I(r)I(\theta) = \begin{cases} \left[\frac{4}{l!} \frac{1}{w^2} \left(\frac{2r^2}{w^2} \right)^l \exp \left(-\frac{2r^2}{w^2} \right) \right] \left[\frac{1}{\pi} \cos^2(l\theta) \right] \\ \left[\frac{4}{l!} \frac{1}{w^2} \left(\frac{2r^2}{w^2} \right)^l \exp \left(-\frac{2r^2}{w^2} \right) \right] \left[\frac{1}{\pi} \sin^2(l\theta) \right] \end{cases} \quad (2.7)$$

where w is the Gaussian waist parameter, given by $w^{-2} = gk_0/2a$. The equations with $\cos^2(l\theta)$ and $\sin^2(l\theta)$ terms are the two degenerate modes with the same propagation constant.

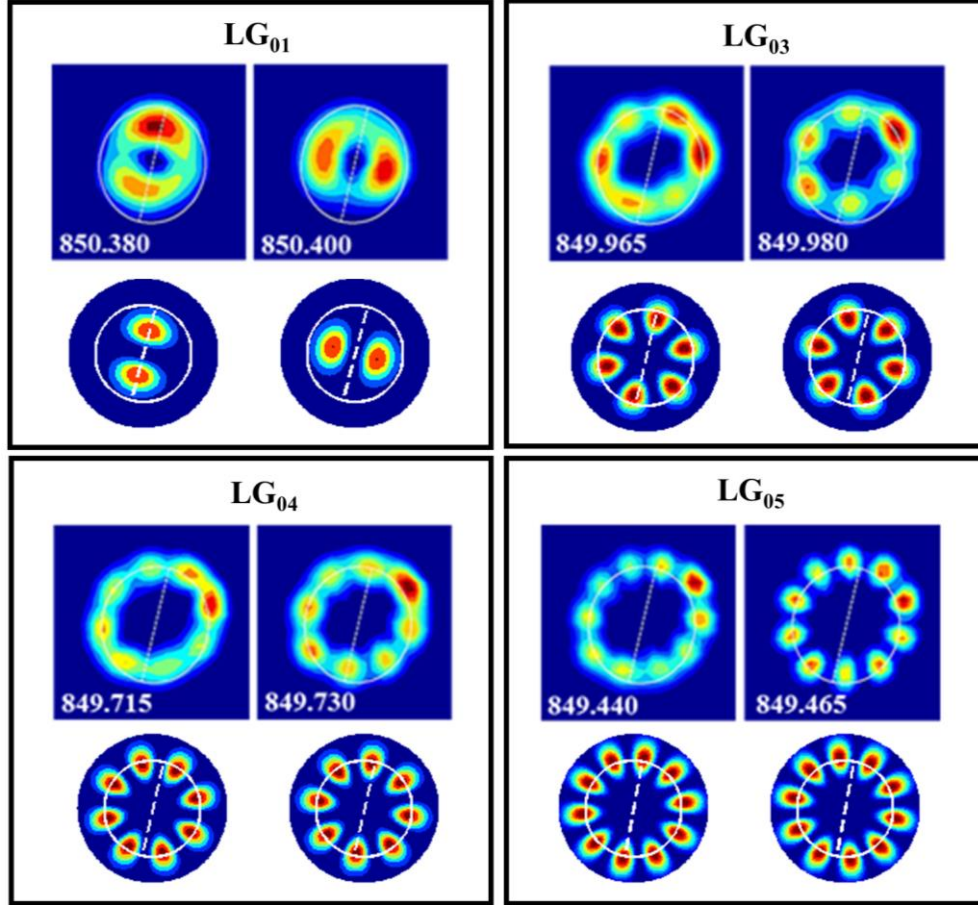


Figure 8. Intensity patterns of LG modes with $l = 1, 3-5$, and $p = 0$. For each LG mode, the top row shows the experimental results and the bottom row shows the calculated results.

While LG modes are general solutions to the paraxial field propagation through dielectric medium with a parabolic index profile, i.e., square law medium, the index step considered here imposes a boundary condition to refine the solutions. In other words, the transverse modes of a VCSEL cavity can be described by LG modes, but the supported mode orders are refined by the oxide aperture. We can infer from the experiment results that the degenerate LG modes with radial mode number $p=0$, and with azimuthal mode numbers $l=1\sim 5$ are supported by the VCSEL cavity as they were observed in the experiment. Using the parameters obtained from numerical

fitting, the calculated intensity patterns of both degenerate LG modes with $p = 0$, $l = 1\sim 5$ are shown in Figure 8, in comparison with the experimental results.

2.3.2 Transverse Mode Lock

To consider transverse mode lock of VCSELs, we need to consider the time variation of the emission fields, which can be described by,

$$E_{0l}(r, \theta, t) = \frac{2}{\sqrt{l!}} \frac{1}{w} \left(\frac{\sqrt{2}r}{w} \right)^l \exp\left(-\frac{r^2}{w^2}\right) \exp(il\theta + i\omega_{0l}t + i\psi) \quad (2.8)$$

where ω_{0l} is the angular frequency of LG_{0l} mode. The frequency separation between consecutive LG modes with increasing l and $p = 0$ is constant at $\delta\omega = \frac{2cg}{n_0a}$, where c is the speed of light. Due

to this constant frequency separation, with a well-defined initial phase, the superposition of the LG modes forms a lasing spot that steadily circulates around the VCSEL aperture. The period of

this circulation is given by $T = \frac{2\pi}{\delta\omega} = \frac{\pi n_0 a}{cg}$.

Figure 9 shows the simulated circulation of a lasing spot in one period. The simulation results prove that locking of VCSEL transverse modes occurs when the equidistant modes have synchronized phases. Phase synchronization can be achieved by injecting resonant pulses into the VCSEL cavity, as will be demonstrated in the pump probe experiment in the following section. Using the experiment and numerical fitting results, the period T is estimated by 8.9 ps, corresponding to a repetition rate of 113 GHz, which is a significant improvement on the modulation speed of conventional methods.

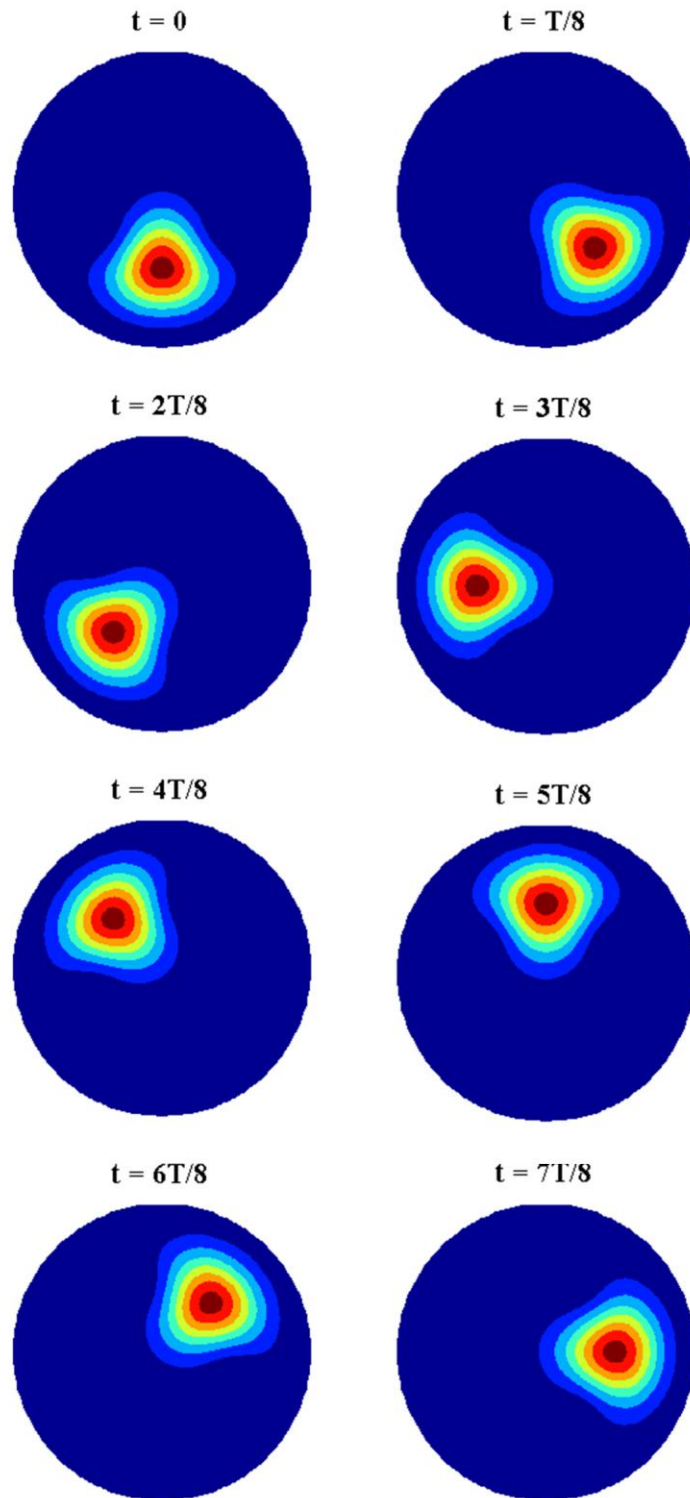


Figure 9. Circulation of the lasing spot around the VCSEL cavity

2.3.3 Pump Probe Experiment

To consider a simplified condition to reach a straight forward conclusion, we studied a VCSEL with a small oxide aperture that supports no more than three transverse modes above threshold. The VCSEL under test here is a commercially available oxide-confined single mode device with a center wavelength of 795 nm. The threshold current is 0.5 mA at 25 °C. The emission spectra of this VCSEL operating at 1 mA and 7 mA are shown in Figure 10. When the VCSEL is driven slightly above threshold at $I = 1$ mA, it shows only the fundamental mode emission at 794.24 nm. When the bias current is increased to 7 mA, the VCSEL emissions shift to the longer wavelength, and two higher order modes are excited besides the fundamental mode, the three peaks shown in the spectrum are 795.56 nm, 796.32 nm, and 797.19 nm. The frequency difference between the two strong peaks (i.e., the two peaks at 797.19 nm and 796.32 nm) is 351.5 GHz.

To measure the ultrafast dynamics of VCSEL, a pump probe setup as shown in Figure 11 is built. Ultrafast pulses are generated by a mode-lock Ti: Sapphire oscillator (Coherent Mira 900), which is pumped by an 18.5 W continuous wave (CW) laser (Coherent Verdi 18) at 512 nm. The pulses are 100 fs in width, and the repetition rate is 76 MHz. These pulses are tuned such that their spectrum covers the spectral span of VCSEL emission. These ultrafast pulses plays two roles in this pump probe experiment: (1) pump pulses injected into the VCSEL cavity to provide coherent control; (2) probe pulses to measure the ultrafast dynamics of VCSEL emission upon injection, with a time resolution comparable with the pulse width.

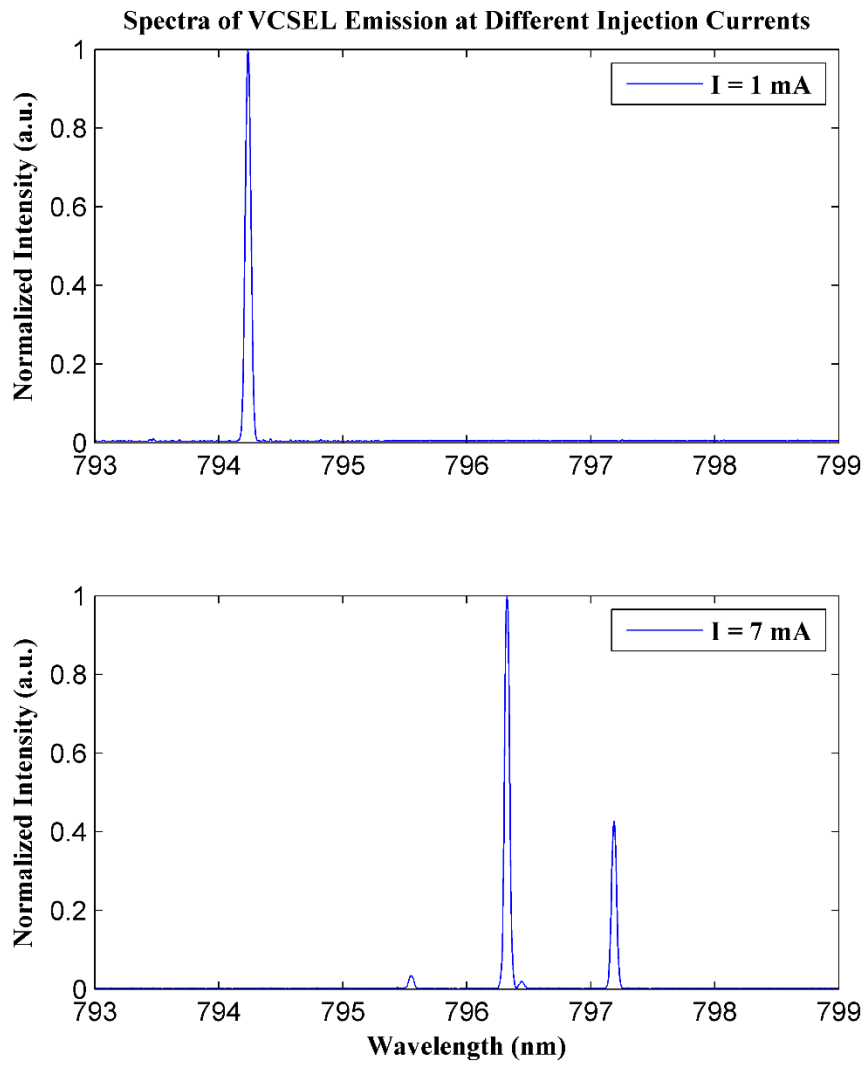


Figure 10. The emission spectra of VCSEL operating at 1 mA and 7 mA.

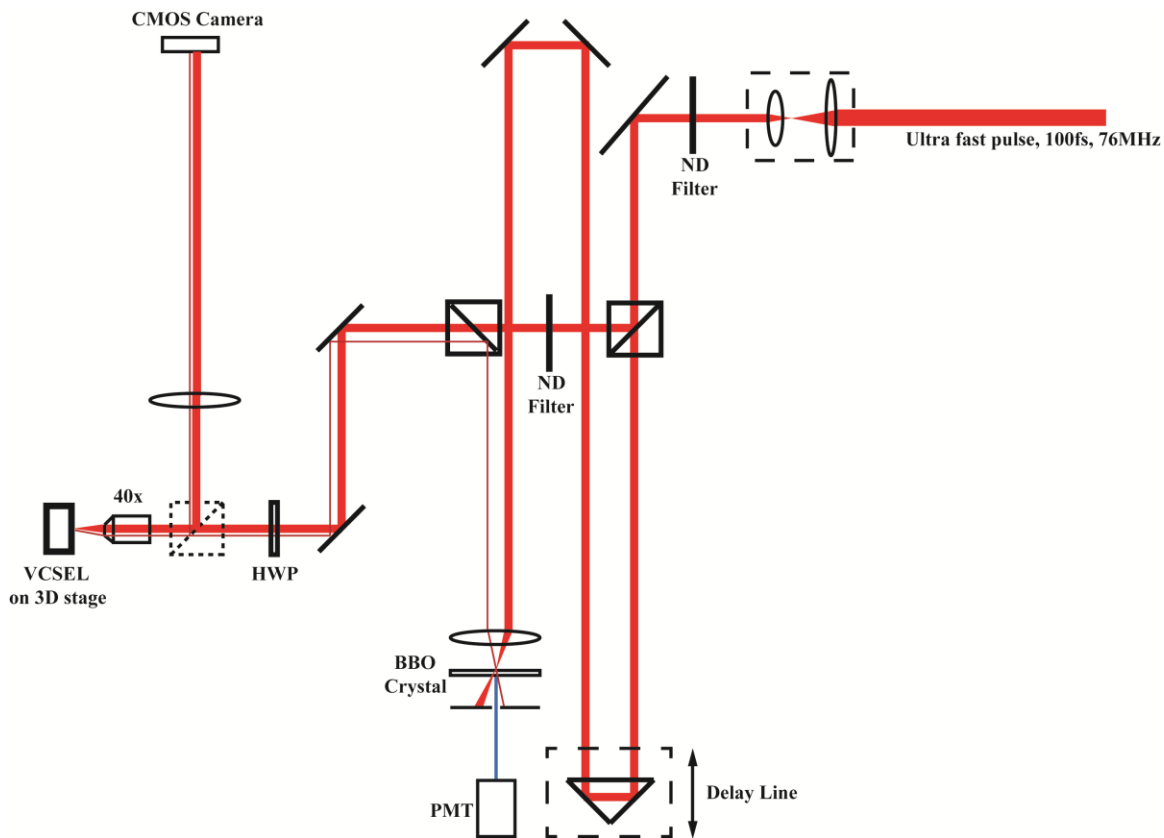


Figure 11. Pump probe experiment setup to measure the ultrafast dynamics of VCSEL.

The ultrafast pulses sent to the pump probe measurements are vertically polarized. The input laser beam are first sent to a beam compressor that consists of two plano-convex lenses with $f = 100$ mm and $f = 30$ mm, and the output laser beam is about 2 mm in diameter. Then it is split into a pump beam and a probe beam by a beam splitter. The probe beam is back reflected by a retroreflector that is mounted on a linear translation stage. By scanning the stage along the delay line, the delay of the probe beam relative to the pump beam when they are combined again on the BBO crystal can be controlled.

The polarization of the pump beam is tuned by a half wave plate so that it coincides with the polarization of VCSEL emission. The pump beam is focus by a 40X objective onto the center of VCSEL's emission window. A large part of the pump power ($>99.5\%$) is reflected by the distributed Bragg reflector (DBR) on the top of VCSEL, but the small portion that propagate through the DBR into the VCSEL cavity is enough to interfere with its emission.

The pump reflection, the VCSEL emission, and the probe beam are then focus onto a 1mm thick β -bariumborate (BBO) crystal which is cut for Type-I phase matching condition. The probe beam up-converts the weak signals of VCSEL emission subject to the injections of pump pulses, and generates a second harmonic generation (SHG) signal that resembles it. The pump and probe beam that pass through the BBO are blocked by an iris so that only the SHG signal is measured by a photomultiplier tube (PMT). As the retroreflector moves along the delay line near the zero delay position, the emission dynamics of VCSEL can be measured.

Coherent control offers the substantial speed improvements over traditional methods as it allows for switching between states on time scales much shorter than the limitation of the intrinsic relaxation oscillation [34]. As mentioned before, the spectrum of the ultrafast pulses is tuned to cover the span of VCSEL emission, so the pump pulse is resonant with the VCSEL

under test. Each resonant injected pulse provides the same absolute phase for all the transverse modes of VCSEL, synchronizing their emission.

Figure 12 shows two traces of the SHG signal measured with 1.8 mW pump power and the VCSEL operated at $I = 1$ mA and $I = 7$ mA respectively. For both plots, the strong signal at $t = 0$ is the SHG signal from the probe pulse and the reflected pump pulse, and it denotes the beginning of synchronized emission. Also shown in the plots are two peaks at $t = 10.8$ ps and $t = 136.1$ ps, which are due to the reflections from the neutral density (ND) filter and the half wave plate (HWP). These two peaks are much weaker than the peak at $t = 0$, so the influence of these injections into the VCSEL cavity are negligible.

When the bias current is 1 mA and there is no injection pulse, as shown in Figure 10(a), the VCSEL is lasing with only one transverse mode. After the injection of coherent pump pulses, as the gain in the VCSEL cavity is temporarily increased, the cavity is able to support one or more high order modes besides the fundamental mode; besides, since the phases of different modes are synchronized to the pump pulse, steady beating among the modes are observed within the first 50 ps. As the injected energy damps out, indicated by the decay of emission power down to the level before injection, the high order modes no longer sustain and no beating is observed.

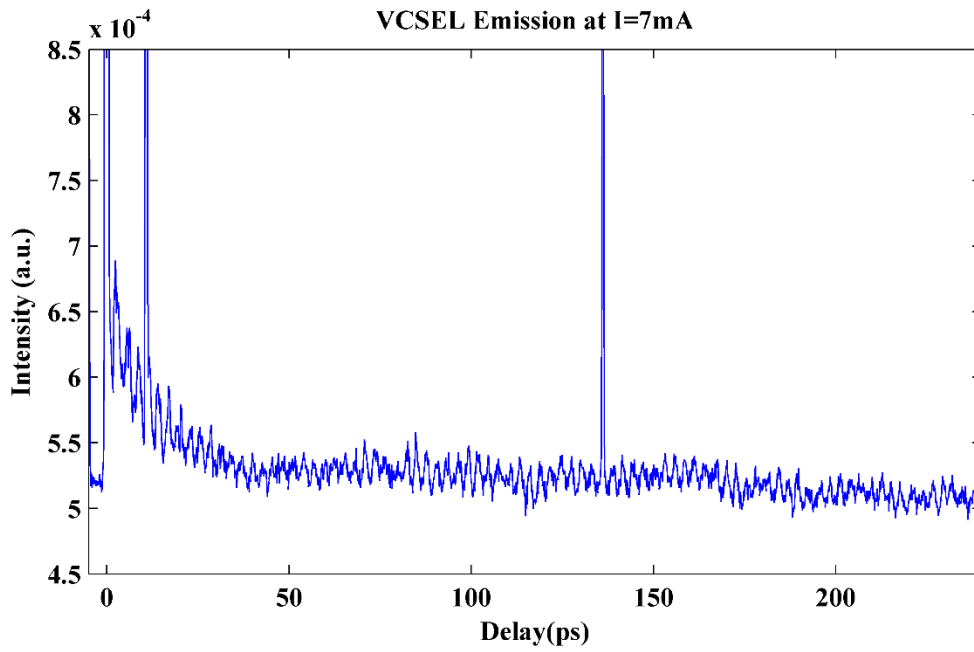
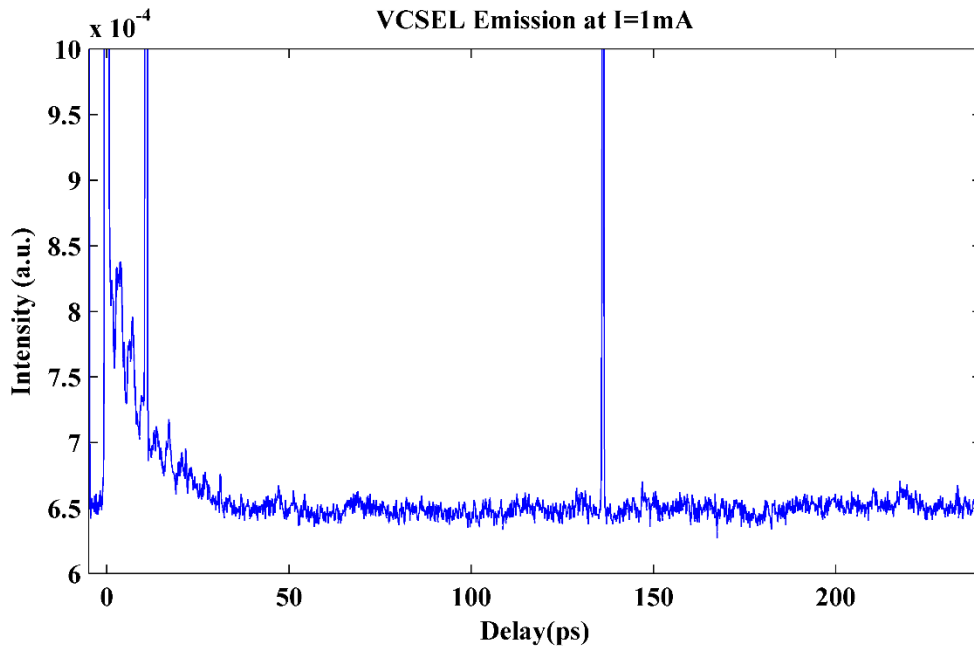


Figure 12. Pump-probe experiment results when the VCSEL operates at I = 1 mA and I = 7 mA respectively.

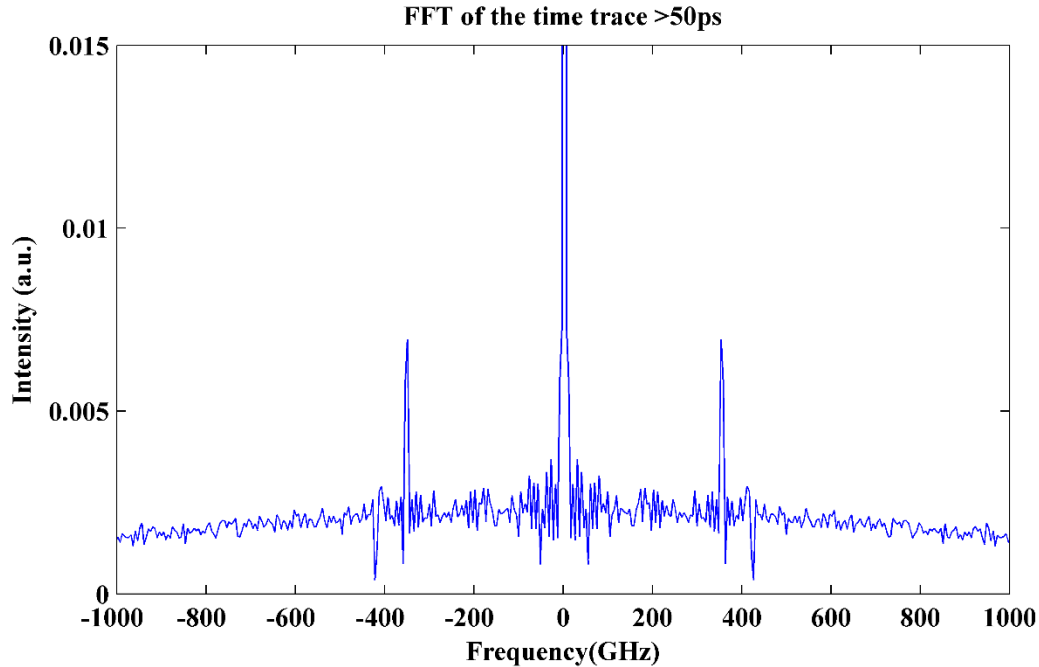


Figure 13. FFT of the time trace after the dissipation of injection energy for VCSEL operate at $I = 7.0\text{mA}$

When the bias current is 7 mA and there is no injection pulses, as shown in Figure 10(b), there are two major modes in VCSEL emission with a frequency difference of 351.5 GHz. After injection of pump pulses, beating is also observed since emissions of the two VCSEL modes are synchronized. However, different from the case with bias current $I = 1\text{ mA}$, the beating sustains even when the emission power is restored to the level before injection. These two VCSEL modes are lasing with the same phase defined by the pump pulse. To confirm that the beating are from the two VCSEL modes shown in Figure 10(b), a Fourier spectrum of the time trace after injection energy dissipation is calculated. As shown in Figure 13, there are side peaks at $\pm 351.2\text{ GHz}$ that correspond to the frequency differences between the major peaks of a free running VCSEL with bias current $I = 7\text{ mA}$.

In this pump-probe experiment, the ultrafast dynamics of a VCSEL with a small emission window that supports only 3 transverse modes are studied. With the two transverse modes of the VCSEL synchronized and beating between them observed, it demonstrates that the emission of VCSEL modes can be synchronized to a strong external pulse with the same initial phase.

2.4 SUMMARY

In this chapter, we investigate on the transverse mode lock of VCSEL to allow large modulation bandwidth of this optical signal source. The requirements for VCSEL mode locking are explored by measurements of its static emission and its ultrafast dynamics. While VCSELs could serve as active optical elements in the on-chip optical network, the following chapters will focus on the passive elements that are fabricated in chalcogenide glass substrate via ultrafast laser writing.

3.0 ULTRAFAST LASER WRITING IN CHALCOGENIDE GLASS

Besides a fast modulated laser source, passive waveguide elements are essential in a photonic integrated circuit (PIC) based network. In this thesis, PIC components are fabricated in chalcogenide glass substrates by ultrafast laser writing. An introduction is first given to the substrate material and the fabrication method respectively. As the most basic component in a lightwave circuit, optical waveguides formed by ultrafast laser writing in chalcogenide glass are characterized with its linear and nonlinear performances.

3.1 CHALCOGENIDE GLASS

3.1.1 Introduction

Chalcogenide glasses (ChGs) are a class of important optical materials useful for mid-infrared optical technology and nonlinear optics [35-38]. The formation of ChG is based on one or more of the chalcogen elements (sulfur, selenium and tellurium), with the addition of other elements such as Ge, As, Sb, Ga, and etc. Decided by the atomic structure of ChG, they can transmit light with wavelength beyond $20\mu\text{m}$, yielding a wide transparency window from visible to mid-infrared. The heavy atoms in the ChG also results in large glass densities, and in turn a high refractive index of $n = 2-3$ and a high nonlinear refractive index n_2 up to a thousand times that of

fused silica. The ultrafast Kerr nonlinearity associated with this large n_2 makes ChG attractive for applications in nonlinear photonic devices for all-optical signal processing. In this dissertation, we focus on the nonlinear properties of ChG.

A number of micro-fabrication techniques have been applied to produce ChG-based nonlinear optical waveguide devices, a popular fabrication technique of which is through thin-film deposition and various lithography schemes. Although a number of excellent waveguide devices have been demonstrated using thin-film based approach [39-42], performance of photonic devices is extremely sensitive to properties of ChG films. In many situations, thin optical films produced by state-of-the-art deposition techniques do not possess as good optical qualities as those found in bulk substrates. This challenge in fabrication diminishes the possibility of building three-dimensional photonic structures through a conventional layer-by-layer lithography technique.

Ultrafast laser writing technique is an alternative to produce optical structures in bulk ChG substrates. However, another challenge arise from the large refractive index and nonlinearity of the material. When the writing beam is focused inside the material, the large refractive index aggravate the spherical aberration; meanwhile, the focused short pulse with high peak intensity experiences large distortion in the material. Eventually it results in an enlarged modification area and undesired material changes along the direction of the writing beam [43]. The asymmetric profile of index change is usually accompanied by large propagation loss and poor light field confinement. Such guiding performance is undesirable for functional photonics devices. These challenges could be overcome by minimizing the spatial and temporal distortion of the writing beam by means of beam shaping [44] and temporal pulse tuning. Through these modifications we have demonstrated ultrafast laser fabrication of high-quality waveguide in ChG

glasses with highly symmetric waveguide profile and 0.65 dB/cm propagation loss at 1550 nm [45]. This opens possibility to produce three dimensional nonlinear lightwave circuits in bulk materials.

3.1.2 Material Nonlinearity and Application in All Optical Signal Processing

Due to the bandwidth hungry applications in modern communication network, it is highly desired to realize signal processing with high bit rates approaching 1 Tbit/s, which is only possible with all optical methods. Therefore, a lot of efforts have been devoted to the research on all optical signal processing, and it has been demonstrated in several platforms, including optical fibers, semiconductors, lithium niobates, and chalcogenide glass.

Different material nonlinearities are usually utilized for all optical signal processing. The laser-material interaction becomes nonlinear for intense electro-magnetic fields, and the total polarization \mathbf{P} induced is no longer in a linear relation with the electric field \mathbf{E} , but satisfies a more general relation [46],

$$\mathbf{P} = \varepsilon_0 (\chi_1 \cdot \mathbf{E} + \chi_2 : \mathbf{E}\mathbf{E} + \chi_3 \vdots \mathbf{E}\mathbf{E}\mathbf{E} + \dots) \quad (3.1)$$

where ε_0 is the vacuum permittivity and χ_j is the j th order susceptibility. Generally, the linear susceptibility χ_1 represents the dominant contribution to \mathbf{P} ; the second order susceptibility χ_2 vanishes as glass is an isotropic medium [46, 47]; the third order susceptibility χ_3 is the major nonlinear effects in chalcogenide glass, and it is responsible for phenomena such as nonlinear refraction, third-harmonic generation, and four-wave mixing. Nonlinear refraction is the nonlinear effect that is focused on throughout this dissertation. This phenomenon is also called Kerr nonlinear effect, and it refers to the intensity dependence of the refractive index, which can be described in its simplest form,

$$n(I) = n + n_2 I \quad (3.2)$$

where n is the linear refractive index, I is the optical intensity, and n_2 is the nonlinear refractive index.

Chalcogenide glass generally has large χ_3 nonlinearity, depending on its composition, its nonlinear refractive index n_2 can be over 1000 times that of silica glass. Besides, with its absorption wavelength edge around 500 nm, for middle infrared (MIR) or infrared (IR) light propagation, chalcogenide glass is a non-resonant nonlinear material. In this case, the Kerr nonlinear response time of chalcogenide glass is not limited by the carrier relaxation or slow thermal nonlinearity [47]. In fact, the Kerr nonlinear response is an instantaneous process with a response time less than 100 fs, showing great potential for ultrafast all optical processing. Beside the fast response time, the high nonlinearity of chalcogenide glass enables compact optical components that is suitable for integration on a single chip.

3.2 ULTRAFAST LASER WRITING

3.2.1 Background and Mechanism

Ultrafast laser writing [15] emerges as a promising technique for fabrication of optical devices in micrometer scales [48-55]. Such optical devices with different functionalities are essentially guiding structures in dielectric materials that are formed by inducing refractive index change along defined paths. During the ultrafast laser writing process, laser pulses are focused to a tight spot in the transparent material. In the presence of each laser pulse, the material will experience high intensity at that precise spot, and nonlinear absorption will occur. This nonlinear absorption

will induce localized ionization, which will further evolve into a process called avalanched ionization. Through this process, the ultrafast laser energy is transferred to the material lattice, and depending on the material type, this could cause the breakage of chemical bonds, micro-stress in the material, and there induce refractive index change. While positive index change is usually found in glass materials, negative index change at the focal spot accompanied by stress induced positive index change around it is found in crystalized materials. Inherent in this technique is the easy and rapid realization of arbitrary complex structures and three dimensional integrated circuits in transparent materials, which has been a major challenge for conventional fabrication methods based on photolithography.

Ultrafast laser writing can be applied to a broad range of materials, with the required threshold intensity I_{th} varies only slightly among materials of a wide range of bandgap energies. This is because that the energy transfer from the laser pulse to the material is caused not only by the nonlinear absorption of the material, but also by an avalanche ionization process that is not dependent on the bandgap energy [16]. However, the desired magnitude and profile of index change can only be obtained by optimizing experiment parameters for a certain material, depending on its optical and mechanical properties.

A lot of efforts have been devoted to the research on ultrafast laser writing in different materials, in which fused silica is one of the most widely investigated materials because of its large transparent window, high mechanical, thermal, and chemical stability, and the low propagation loss down to 0.3 dB/cm achievable for waveguides written by ultrafast laser [56]. A large variety of functional optical structures have been demonstrated in fused silica substrate owing to this low propagation loss, such as directional couplers [51, 57], Bragg gratings [49, 58], photonic lanterns [53], and so on.

3.2.2 Fabrication Challenges in ChG

Throughout this thesis, a transverse configuration is used in the ultrafast laser writing, as shown in Figure 14. For a general ultrafast laser writing process, the laser beam is focused by a microscope objective with large numerical aperture (NA), forming a tight laser spot beneath the sample surface. An imaging system is built to help identifying the sample surface and controlling the depth of laser spot. The sample is mounted on a 3D motion stage, whose movement can be programmed by a computer. In a transverse writing configuration, stages moves in the plane that is normal to the direction of writing beam propagation. With the writing beam tightly focused inside the material, and the relative translation between the laser focus and the sample, structures of refractive index change can be formed inside the material. Such a configuration allows more flexibility in the structure design and more uniform cross section along the waveguide.

However, when a transverse writing configuration is used, the formed waveguide cross section corresponds to the YZ plane of the writing laser beam profile. This feature could be problematic for ultrafast laser writing in ChG. Due to its large linear refractive index (about 2.44 at 800 nm) and large nonlinearity, considerable spherical aberration at the tight laser focus and self-focusing effects are induced, and elongation of the laser focus are observed. To estimate the waveguide cross section of ChG considering these effects, Gaussian beam propagation in ChG is simulated. As shown in Figure 15, in the XY plane which is normal to the beam propagation direction, the cross section of the laser focus is circular. However, in the YZ plane, the elliptical laser focus shows obvious distortion. Such a beam profile would result in a waveguide cross section in a similar shape.

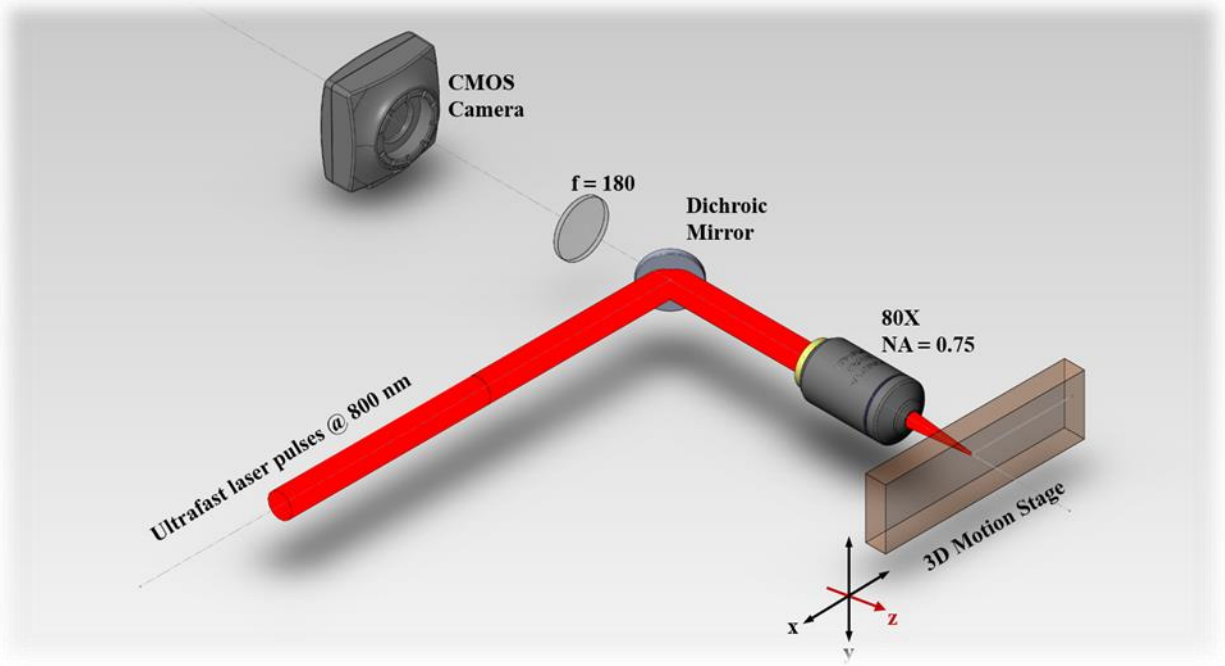


Figure 14. Transverse configuration for ultrafast laser writing.

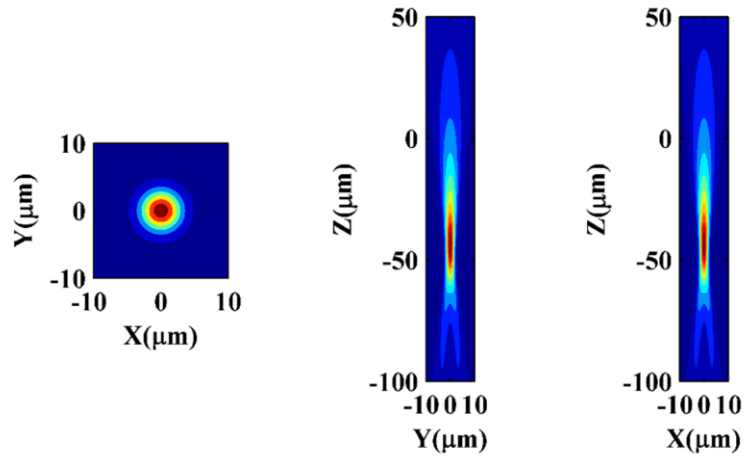


Figure 15. Simulated ChG waveguide cross section without spatial beam shaping.

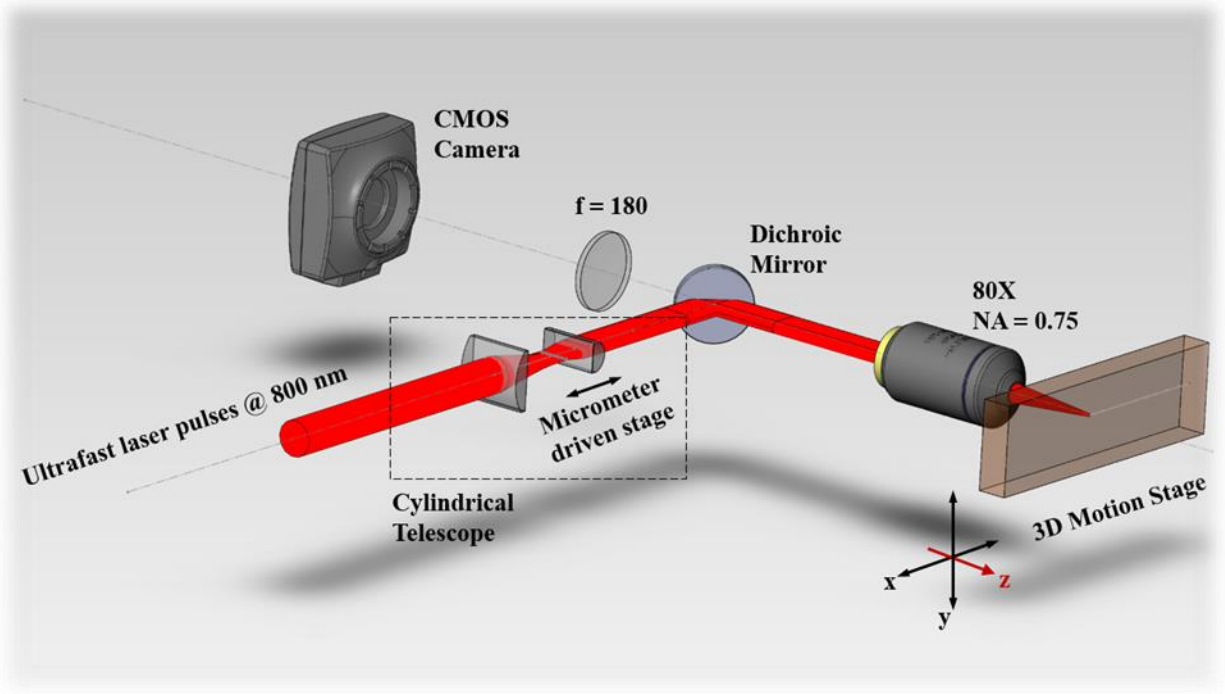


Figure 16. Ultrafast laser writing setup with spatial beam shaping.

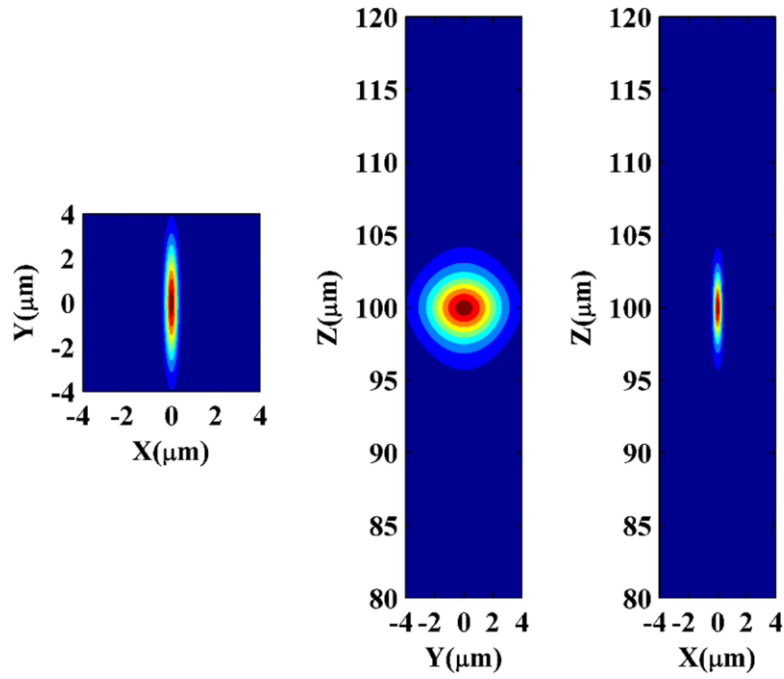


Figure 17. Simulated ChG waveguide cross section with spatial beam shaping.

3.2.3 Spatial Beam Shaping

To solve the problem inherent in this transverse writing configuration, a spatial beam shaping technique [44] is used to allow controllability over the waveguide cross section. A cylindrical telescope is added in the writing beam path (Figure 16), and it modifies the writing beams in two ways: firstly, it reduces the beam size in the y direction by 3 times; Secondly, it induces an offset of about 100 microns between the focus positions in the x and y directions. With these modifications, additional astigmatism is induced to compensate the spherical aberrations and nonlinear effects. It results in an elliptical laser focus in the XY plane, but in the YZ plane, the beam cross section is almost circular. The effects of this cylindrical telescope are simulated (Figure 17) and the beam profile in the YZ plane suggest a circular waveguide cross section in ChG.

3.3 PRELIMINARY TESTS ON CHG WAVEGUIDES

For the experiments throughout this dissertation, gallium lanthanum sulfide (GLS) chalcogenide glass is used as substrate material, for its good thermal stability, non-toxic nature, and its large nonlinear figure of merit (FOM). As preliminary experiments, simple optical waveguides are written in the ChG substrate and their performances are tested.

The waveguides in GLS ChG glass is written using a Coherent RegA 9000 laser system, producing pulse trains at 800 nm at a repetition rate of 250 kHz. An astigmatic beam shaping technique is used to spatially modify the input beam so as to write symmetric waveguides with low propagation loss in this highly nonlinear material. During the writing, the GLS sample is

mounted on a three-axis motion stage (Aerotech) and translated in the direction orthogonal to the writing beam. With polarization parallel to the writing direction, the writing beam is focused by an 80X objective (NA = 0.75) at 237 μm below the sample surface. The pulse width, pulse energy, and translation speed of the sample is manipulated to achieve best performance of the waveguides.

3.3.1 Temporal Pulse Tuning

Figure 18 and Figure 19 shows the cross sections of the waveguides written with 300 fs and 1.8 ps pulse widths, and the associated guiding profiles at 1040 nm. The pulse energy and translation speed are both optimized for each pulse width. When the pulse width is 300fs, with the optimized pulse energy at 400 nJ, and translation speed at 2 mm/s, the transmission is 23% and the mode field diameter (MFD) is $7.5 \times 10.1 \mu\text{m}^2$. When the pulse width is 1.8 ps, with the optimized pulse energy at 300 nJ, and translation speed at 2 mm/s, the transmission is 21% and the MFD is $6.7 \times 7.7 \mu\text{m}^2$. The performance of the two waveguides are similar in terms of loss, but the latter has a more symmetric and tighter confinement. Besides, the laser irradiation released in such a short duration of time not only induced confined index change around the tight focal volume, but also mild modifications of the material around the waveguide cross section. This could cause undesired performances for complex lightwave circuits where waveguides structures are closely integrated. Therefore, the pulse width is chosen around 1.8 ps for ultrafast laser writing in ChG in the work throughout this thesis.

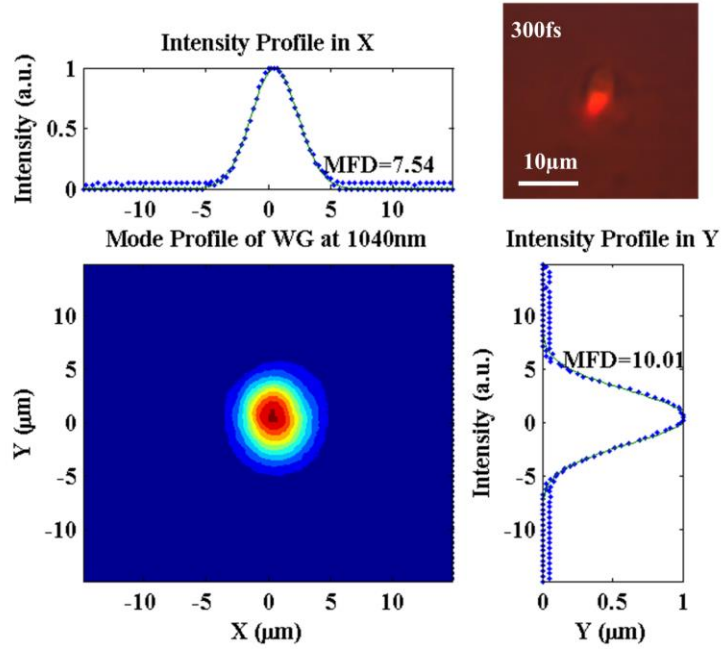


Figure 18. Guiding profile at 1040nm of a waveguide written with 300 fs pulse width and its cross section.

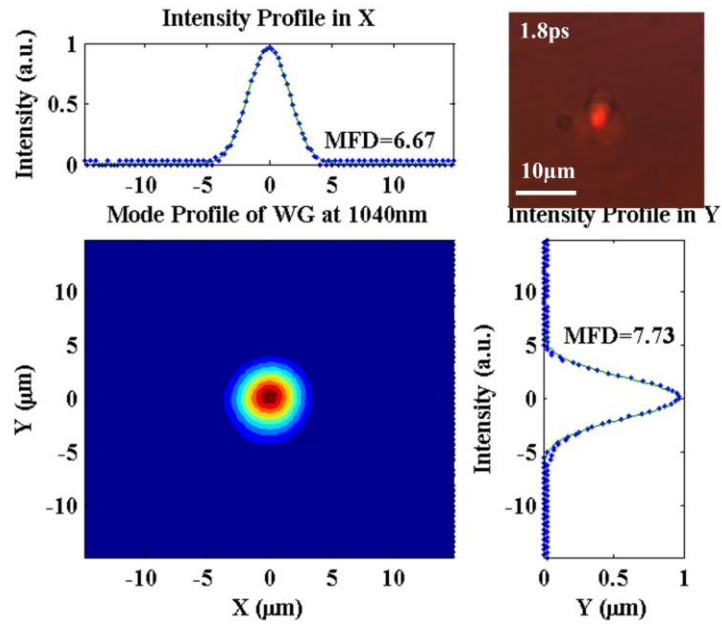


Figure 19. Guiding profile at 1040nm of a waveguide written with 1.8 ps pulse width and its cross section.

3.3.2 Pulse Propagation in ChG Waveguides

To study the pulse propagation, ChG waveguides written with 328 nJ, 1.8 ps chirped pulse at the translation speed of 1.5 mm/s are tested with ultrafast pulses. By launching ultrafast pulses at 1040 nm with 446 fs pulse width into the waveguides, the spectral and temporal evolution of the pulses are studied with inputs in two orthogonal polarizations. Input polarization along the writing beam direction is denoted as s-polarized input, and the orthogonal polarization is denoted as p-polarized input.

Both input polarizations experience a large amount of spectral broadening when the input peak intensity increases from 5 GW/cm² to 90 GW/cm², with the spectral width increasing from about 20nm to over 140nm (Figure 20). The pulse stretching is insignificant for the short propagation length inside the waveguide (Figure 21), but it is related to the input intensity due to the nonlinear index change in the waveguide: for p-polarized input, the pulse width is increased to 633 fs at 5 GW/cm², and to 1004 fs at 90 GW /cm²; for s-polarized input, the pulse width is increased to 558 fs at 5 GW/cm², and to 930 fs at 90 GW /cm². These results imply that nonlinear effect is dominant for 1040nm pulse propagation in the ChG waveguide, while the linear dispersion is negligible.

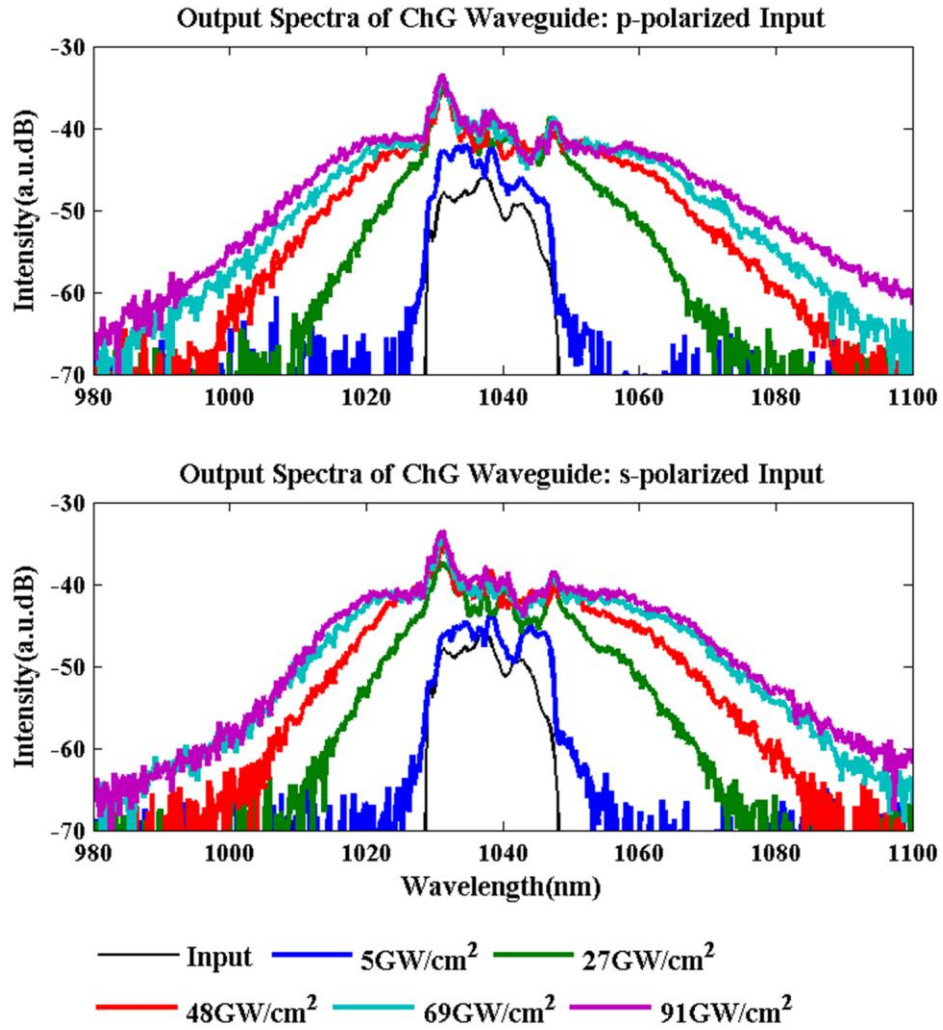


Figure 20. Spectral broadening with increasing input intensity.

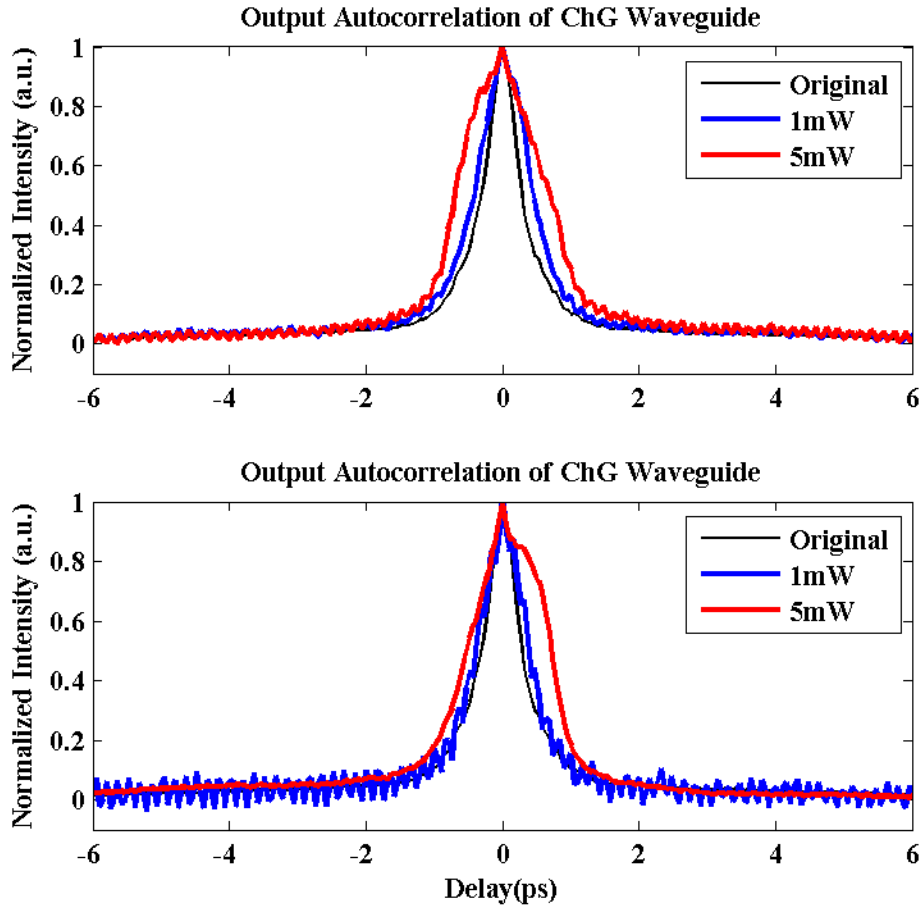


Figure 21. Pulse stretching with increasing input intensity.

3.4 MODE COUPLING IN WAVEGUIDE STRUCTURES AND NONLINEAR SWITCHING

With the capability to fabricate three dimensional arbitrary structures in nearly any transparent materials [16, 59], it serves as an alternative to fabrication techniques based on photolithography in making PIC components. At the very beginning stage of applying the ultrafast laser writing

technique to PIC fabrication, this dissertation focused on the basic nonlinear components for photonic integrated circuits that are fabricated by ultrafast laser writing.

PIC devices are built with optical waveguides that perform not only guiding, but also other important function such as coupling, switching, and splitting of optical signals. The basic nonlinear components under the scope of this thesis are based on the coupling among different waveguide modes or among adjacent waveguides. The coupled mode theory [60, 61] is used to simulate these phenomenon.

In the coupled mode theory, variations of the dielectric tensor, in both transverse and longitudinal planes, can be considered as a perturbation that couples the unperturbed modes in the structure, which otherwise are orthogonal to each other in a linear, lossless waveguide. The dielectric tensor can be expressed,

$$\varepsilon(x, y, z) = \varepsilon_a(x, y) + \Delta\varepsilon(x, y, z) \quad (3.3)$$

where $\varepsilon_a(x, y)$ is the unperturbed dielectric tensor, and $\Delta\varepsilon(x, y, z)$ represents the dielectric perturbation. The presence of this dielectric perturbation $\Delta\varepsilon(x, y, z)$ gives rise to additional polarization that is associated with the originally excited mode in the structure $E_0(x, y, z, t)$,

$$\Delta P = \Delta\varepsilon(x, y, z)E_0(x, y, z, t) \quad (3.4)$$

This additional polarization causes power redistribution among the orthogonal modes of the structure. The couple mode equations have a general form as follows,

$$\frac{d}{dz} A_k = i \sum_n \kappa_n A_n(z) e^{i\Delta\beta_n} \quad (3.5)$$

where A_n is the field amplitude of the n -th mode, $\Delta\beta_n$ is the phase mismatch between the k -th mode and the n -th mode, and κ_n is the coupling coefficient between the k -th mode and the n -th mode, which is decided by the additional polarization.

Two kinds of dielectric perturbations are considered in this dissertation: (1) a periodic index change along a single waveguide; (2) two or more waveguides in the vicinity of each other causing perturbations in the transverse plane of field propagation. The specific formulations of the coupled mode theory are presented in the corresponding chapters.

3.5 SUMMARY

This chapter introduces the chalcogenide glass substrate and the ultrafast laser writing technique used for making nonlinear photonic integrated circuit components. The challenges of ultrafast laser writing in ChG are overcome by the combination of the spatial beam shaping and temporal pulse tuning. The waveguide performance is tested with ultrafast pulse propagation at 1040nm. In the following chapters, several basic nonlinear optical waveguide structures are studied.

4.0 ULTRAFAST SWITCHING WITH WAVEGUIDE BRAGG GRATING

It is demonstrated in this chapter that all-optical switching with a waveguide Bragg grating inscribed by ultrafast laser in chalcogenide glass. The Bragg waveguide is a third order grating with resonant wavelength centered at 1551.51 nm. A cross-phase modulation scheme is utilized to observe all-optical switching, with a CW signal light at the grating's resonant wavelength, and pump pulses centered at 1040 nm. Exploiting the large nonlinear refraction index of chalcogenide glass, output signal modulation up to 12% is observed with this 2-cm long grating at pump pulse energy of 40 nJ, which is at least an order of magnitude improvement in the switching pulse energy compared to silica.

4.1 INTRODUCTION

Chalcogenide (ChG) glasses are among the most promising nonlinear optical materials as device substrates for all-optical signal processing [35, 38]. With ultrafast switching times of the χ_3 nonlinear process, the large nonlinear refractive index of ChGs, which is reported up to 1000 times that of fused silica, makes ChG devices available for switching times down to tens of femtoseconds and largely reduced operation power. Besides, the wide optical transparent window from visible to mid-infrared, negligible two photon absorption (TPA) and free carrier

absorption (FCA) at the telecom wavelength also add to the attractive characteristics of the material.

Waveguide Bragg gratings have been demonstrated in ChGs as an essential components in photonic integrated circuits for high-bit-rate signal processing, by allowing nonlinear operations such as 2R regenerations [39, 40] and all-optical switching [62, 63], and the required optical power for nonlinear operations is reduced due to the large Kerr nonlinearity of the material. Fabrication of the ChG gratings is usually a two-step process including the formation of ChG waveguide and the grating structure, respectively. As one of the most popular micro-fabrication techniques being applied to produce ChG-based nonlinear optic waveguide devices [39, 64], thin-film deposition combining with photolithography techniques have successfully fabricated a number of excellent ChG waveguide devices, whereas performance of the devices is extremely sensitive to properties of ChG films, which in many situations do not possess as good optical qualities found in bulk ChG substrates. Due to the limitations from thin-film processes, building three-dimensional photonic structures in ChG through a layer-by-layer lithography technique appears as a challenge.

The ultrafast laser writing technique is well-known for its capabilities of 3D fabrication and fast prototyping [16, 59]. It has been applied to the fabrication of waveguide Bragg gratings in silica glass in a single-step writing [49, 65]. These waveguide Bragg gratings show excellent linear performance with grating strength > 35 dB, but they are not suitable for all-optical switching due to the small nonlinear refractive index in silica, which suggests high switching power would be required. A reduction in the switching power can be expected with highly nonlinear materials as in the case of ChGs. However, the large nonlinear refractive index also incurs new challenges in the ultrafast laser writing process. Highly asymmetrical waveguides

with elongated cross section and multiple guiding regions are found after ultrafast laser writing [43, 66, 67], which are results of spherical aberrations induced by the high refractive index, as well as the self-focusing and filamentation from the material nonlinearity. Such waveguide features usually lead to poor mode confinement and large waveguide loss, and in turn a deteriorated grating strength, compromising the performance of the all-optical switching device. To mitigate the nonlinear effects during the ultrafast laser writing process, temporal pulse tuning and spatial beam shaping can be employed [44, 45].

In this paper, we report all-optical switching with a waveguide Bragg grating inscribed by ultrafast laser in chalcogenide glass. The Bragg waveguide is a third order grating with resonant wavelength centered at 1551.51 nm. A cross-phase modulation scheme is utilized to observe all-optical switching, with a CW signal light at the grating's resonant wavelength, and pump pulses centered at 1040 nm. Exploiting the large nonlinear refraction index of chalcogenide glass, output signal modulation up to 12% is observed with this 2-cm long grating at pump pulse energy of 40 nJ.

4.2 SWITCHING PRINCIPLES

The refractive index of a waveguide Bragg grating varies along the length of periodically, and can be described,

$$n(z) = n_0 + n_1 \cos\left(\frac{2\pi}{\Lambda} z\right) \quad (4.1)$$

where n_0 is the DC index of the waveguide, n_1 is the amplitude of periodic index change, and Λ is the period of the WBG. Based on the coupled mode theory, the effect of the grating is to

couple forward- and backward-propagating light with wavelength λ close to $2n_0\Lambda$, resulting in strong reflection for light with resonant wavelength $\lambda_B=2n_0\Lambda$ and total transmission for light with its wavelength far from the resonant wavelength.

When the propagating light in the WBG is strong, the nonlinear response of the material needs to be considered. Here we consider the condition where a weak signal with wavelength λ close to the resonant wavelength λ_B , and a strong pump with wavelength far from λ_B , so the nonlinear response from the weak signal can be neglected. Both the propagation direction and the polarization are the same for the pump and probe. Let $I(z,t)$ be the pump intensity, the refractive index of the WBG is thus described,

$$n(z) = n_0 + n_1 \cos\left(\frac{2\pi}{\Lambda} z\right) + n_2 I(z,t) \quad (4.2)$$

where n_2 is the nonlinear refractive index of the material.

The effect of the grating is still to couple forward- and backward-propagating light with wavelength λ close to $2n_0\Lambda$, since the nonlinear index change is small compared to n_0 . A set of coupled mode equations governs the effect of the grating,

$$\frac{\partial A_+}{\partial z} + \frac{n_0}{c} \frac{\partial A_+}{\partial t} = i\kappa A_- + i\delta A_+ + 2i\Gamma I(z,t) A_+ \quad (4.3)$$

$$-\frac{\partial A_-}{\partial z} + \frac{n_0}{c} \frac{\partial A_-}{\partial t} = i\kappa A_+ + i\delta A_- + 2i\Gamma I(z,t) A_- \quad (4.4)$$

with $\delta = \frac{\omega - \omega_B}{c/n_0}$, $\kappa = \frac{\pi n_1}{\lambda}$, $\Gamma = \frac{4\pi n_0}{\lambda Z} n_2$. A_+ and A_- are respectively the forward- and

backward-propagating light, z is the vacuum impedance. Modulations to the signal are different when the pump is continuous wave (CW) or pulsed, which are respectively described in the following.

When the strong pump propagating through the WBG is CW or can be treated as CW (its propagation time through the WBG is much smaller than its pulse width), a constant index change is applied to the waveguide, resulting in a fractional change in the wave vector of the WBG,

$$\frac{\Delta k}{k} = \frac{n_2}{n_0} I \quad (4.5)$$

And the resonant wavelength is shifted correspondingly by,

$$\frac{\Delta \lambda}{\lambda_B} = \frac{2n_2}{n_0} I \quad (4.6)$$

where the factor of 2 accounts for the cross phase modulation (XPM). Since the nonlinear refractive index of material is generally positive, the band gap is red shifted when a strong CW pump is propagating through the WBG. The output power of a weak probe initially tuned to the blue side of the band gap increases, while for probe initially tuned to the red side the band gap, the output power decreases.

When the strong pump propagating through the WBG is pulsed, the output power of the probe is time dependent, and its time trace can be obtained by numerically solve the coupled mode equations [68, 69]. Qualitatively speaking, the propagation of this short pulse induces a time-dependent phase change to both the forward- and backward-propagating probe, and induces frequency shift of the probe which is proportional to the gradient of the pump intensity profile. For forward-propagating light, with $n_2 > 0$, the leading edge of the pump pulse causes a red shift of the probe frequency, while its trailing edge causes a blue shift of the probe frequency. The situation for the backward-propagating light is opposite. The modulations of the probe output would be sensitive when its frequency is tuned to the edge of the WBG's band gap. In the

experiments below, short pump pulses are used to study the nonlinear switching of the WBG in chalcogenide glass.

4.3 WAVEGUIDE BRAGG GRATING IN CHG

4.3.1 Waveguide Bragg Grating Written by Ultrafast Laser

An arsenic-free gallium lanthanum sulfide (GLS) ChG with excellent environmental stability was used as the substrate material in the experiment. Ultrafast laser pulses centered at 800 nm were produced at a repetition rate of 250 kHz by a Ti: Sapphire regenerative amplifier system (Coherent RegA 9000). To mitigate focal distortions, so as to control the size and shape of the waveguide cross section and reduce propagation loss, the writing pulses were tuned to 1.5 ps in width and sent through a cylindrical telescope that provides about 3 times demagnification in the beam profile perpendicular to the writing direction and an astigmatic offset of about 21 μm . The writing beam were circularly polarized and focused at 275 μm beneath the ChG sample via an 80X microscope objective (NA = 0.75). With the ChG sample substrate ($25 \times 25 \times 1 \text{ mm}^3$) mounted on a three-axis motion stage (Aerotech), Bragg grating structures were formed in the substrate by programmed translations of the stage in relation to the fixed focal point.

With a single-scan technique, where periodic modulation of the writing beam induced a series of partially overlapping refractive index voxels that formed a waveguide and the Bragg structure at the same time, a third order waveguide Bragg grating was formed in the ChG substrate. The translation speed of the stage was set to 1 mm/s, while the output of the laser system is modulated by a periodic signal at 1.02 kHz with a 25% duty cycle. This induced in the

ChG substrate both the average DC index change sufficient to support guided modes, and the AC refractive index change with a period of $0.96 \mu\text{m}$, resulting in a third order waveguide Bragg grating with the resonant wavelength at about 1550 nm in ChG ($n = 2.37 @ 1550 \text{ nm}$). After the ultrafast laser writing process, the input and output facets of the ChG substrate were ground and polished, leaving a grating length of 20 mm .

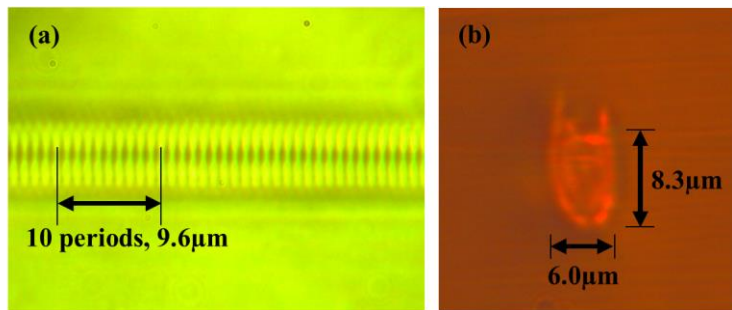


Figure 22. Microscope images of the WBG: (a) periodic structure; (b) cross section.

The grating structure of the formed waveguide Bragg grating in ChG was observed by an optical microscope (Figure 22 (a) and (b)). Ten periods of the grating structure were measured to be $9.6 \mu\text{m}$, corresponding to a third order grating at around 1550 nm , while a small offset from the designed wavelength can be expected due to increased refractive index in the ChG waveguide. Figure 22 (b) shows microscope image of end facet of the waveguide Bragg grating. The waveguide cross section was measured to be $8.3 \mu\text{m}$ in the direction along the writing beam and $6.0 \mu\text{m}$ in the orthogonal direction. This nearly symmetric waveguide cross section is a result of the combination of astigmatic beam shaping and temporal pulse tuning in the ultrafast laser writing process.

4.3.2 Guiding Performance and Grating Transmission

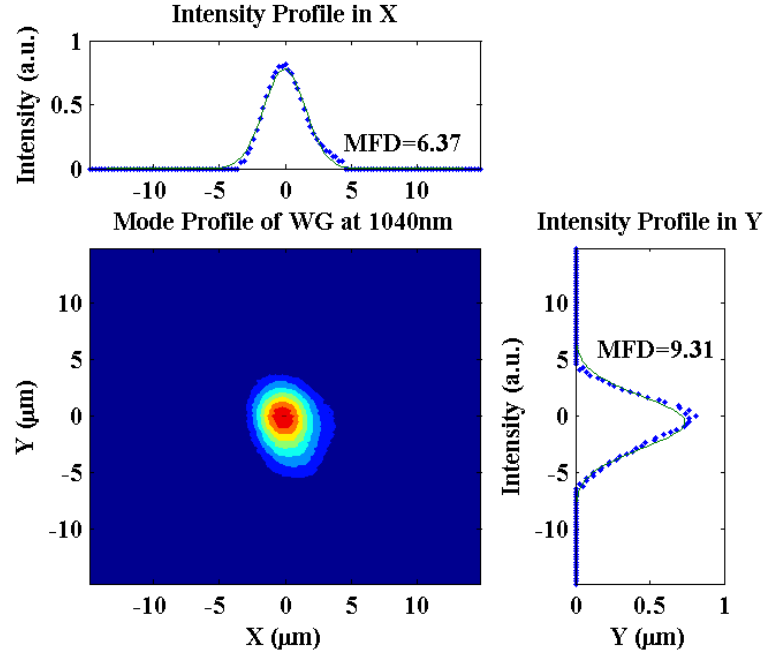


Figure 23. Near field guiding mode profile of the pump pulses centered at 1040 nm.

The waveguide Bragg grating is first characterized for their waveguide performances at the pump wavelength and the signal wavelength tuned away from the bandgap.

Pump pulses centered at 1040 nm are used in the experiment. The average power is set to 500 μW so that nonlinear absorption is negligible when measuring the insertion loss of the ChG waveguide. The insertion loss of the WBG at 1040 nm is 4.95 dB, in which 1.5 dB is from the reflection loss of the input and output facets of the sample. Thus the average pump power inside the WBG is estimated to be 66% of the input power. Single mode operation at 1040 nm is confirmed from the near field guiding mode profile, as shown in Figure 23. By Gaussian fitting

the intensity profile in the two orthogonal directions, the mode field diameters (MFDs) are found to be 6.37 μm and 9.31 μm , respectively.

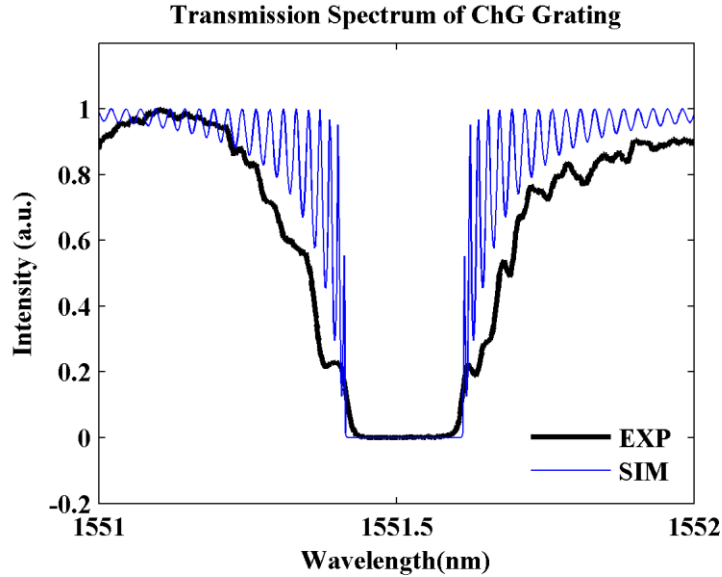


Figure 24. The measured transmission spectrum of the ChG WBG and simulation.

The probe wavelength is tuned to 1552 nm outside the bandgap of the WBG so that the probe signal can propagate through. The insertion loss at this wavelength is 4.98 dB.

The transmission spectrum of the ChG WBG is measured by an optical spectrum analyzer (ANDO OSA AQ6315B) when a broadband source is coupled into the WBG from free space. Figure 24 shows the measured transmission spectrum and its numerical approximation. The center wavelength of the WBG bandgap is $\lambda_B = 1551.51$ nm, the width of the bandgap is 0.2 nm, and the index modulation of the Bragg grating is estimated to be 3×10^{-4} .

4.4 NONLINEAR SWITCHING RESULTS

4.4.1 Pump Probe Experiment

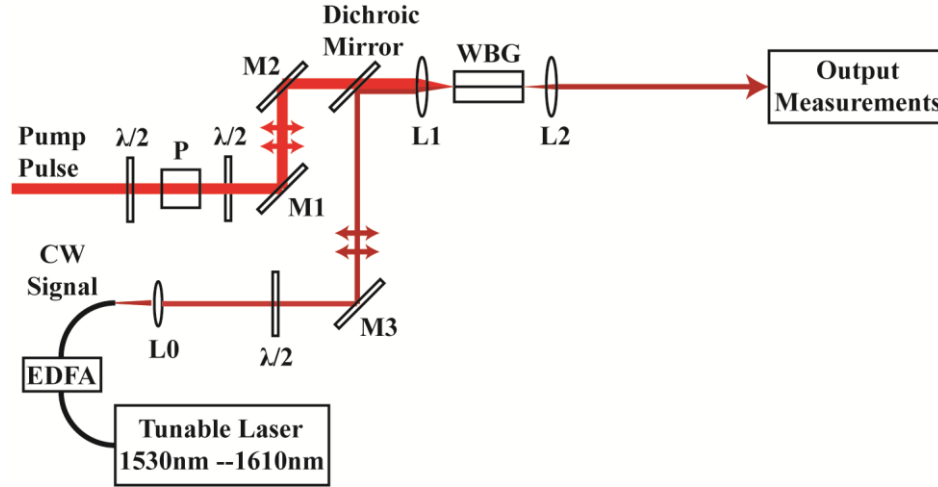


Figure 25. Schematic of the experimental setup using a cross phase modulation scheme.

A cross phase modulation scheme was utilized to observe all-optical switching in this ChG waveguide Bragg grating, with an experiment setup as shown in Figure 25. The IMPULSE™ femtosecond laser system produced pump pulses centered at 1040nm with a repetition rate of 200 kHz. After going through two half wave plates and a polarizer to control their power and polarization, the pump pulses were measured by an autocorrelator and their pulse width was found to be 446 fs. The CW signal was generated by a tunable laser in 1530 – 1610 nm and amplified by an erbium doped fiber amplifier (EDFA). The pump pulse and the CW signal were both linear polarized in the plane of the figure. They were combined by a dichroic mirror and launched into the ChG grating by an aspheric lens with $f = 13.86$ mm. The output CW signal from the grating was collected and collimated by another aspheric lens with $f = 13.86$ mm for

imaging and subsequent measurements. The insertion loss of the ChG waveguide Bragg grating was 4.95 dB for the pump pulses at 1040nm and 4.98 dB at 1552 nm, respectively.

4.4.2 Output Signal Modulations

Depending on the initial detune of the probe wavelength, ‘switch-on’ and ‘switch-off’ modulations are observed with input of short pump pulses. The modulation depth is related to the both the pump power and the detuning of probe wavelength. The ‘switch-on’ and ‘switch-off’ modulations are first studied with various input pump powers.

When the signal wavelength is tuned to 1551.70 nm, the ‘switch-on’ modulations are observed (Figure 26). And ‘switch-off’ modulations are achieved when the probe wavelength is set to 1551.62 nm (Figure 27). The probe wavelengths in both cases are indicated by the two vertical lines in Figure 28. In both transmission waveforms, the signal responses to each pump pulse with a sharp leading edge, which arises from the ultrafast Kerr nonlinear effect. The trailing edge of the output signal shows two time scales, a fast response corresponding to the trailing edge of the pump pulse and a slow response related to free carrier lifetime in ChG [70, 71]. Although ChG is known for its large nonlinear figure of merit (FOM), the two photon absorption (TPA) and hence free carrier generation is only negligible for wavelength far from its bandgap. As the bandgap energy of ChG corresponds to the wavelength at about 500 nm, pump pulses centered at 1040 nm still experience a certain amount of TPA and free carrier generation when going through the ChG waveguide. The free carrier recovery in the ChG causes the slow trailing edge in the output signal, limiting the ultrafast modulations. The influences of free carrier generation can be reduced by replacing the pump pulses with longer wavelengths or reducing its repetition rate.

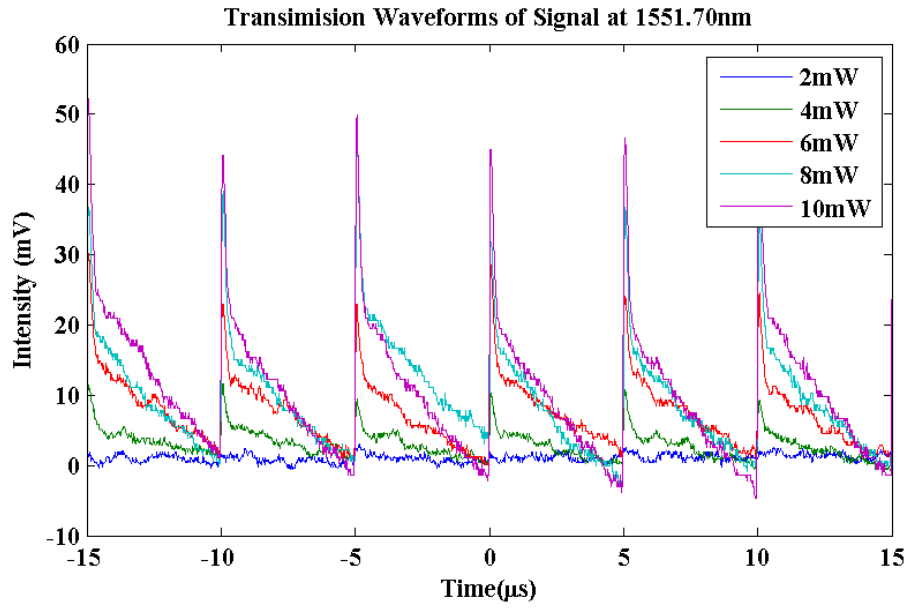


Figure 26. ‘Switch-on’ modulations for probe wavelength at 1551.70nm.

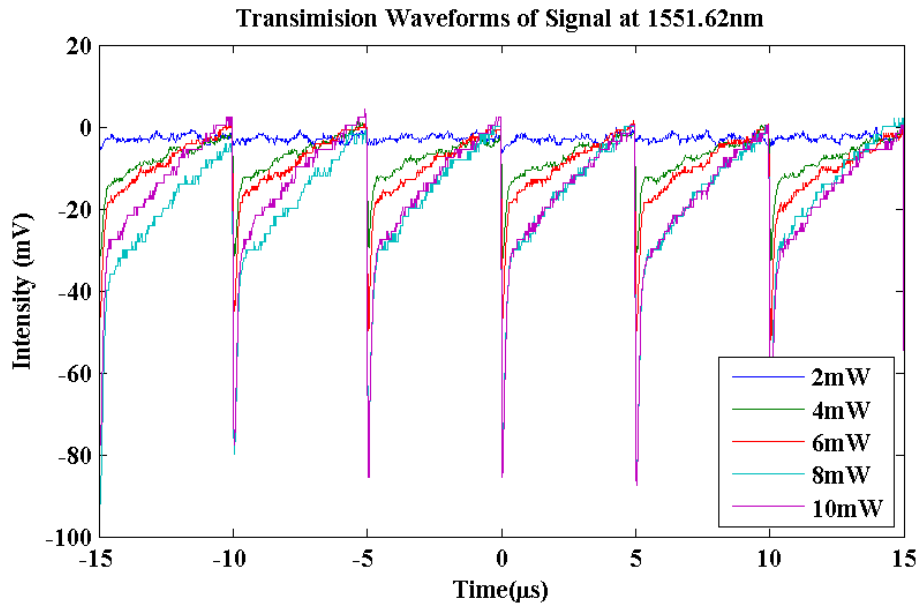


Figure 27. ‘Switch-off’ modulations for probe wavelength at 1551.62nm.

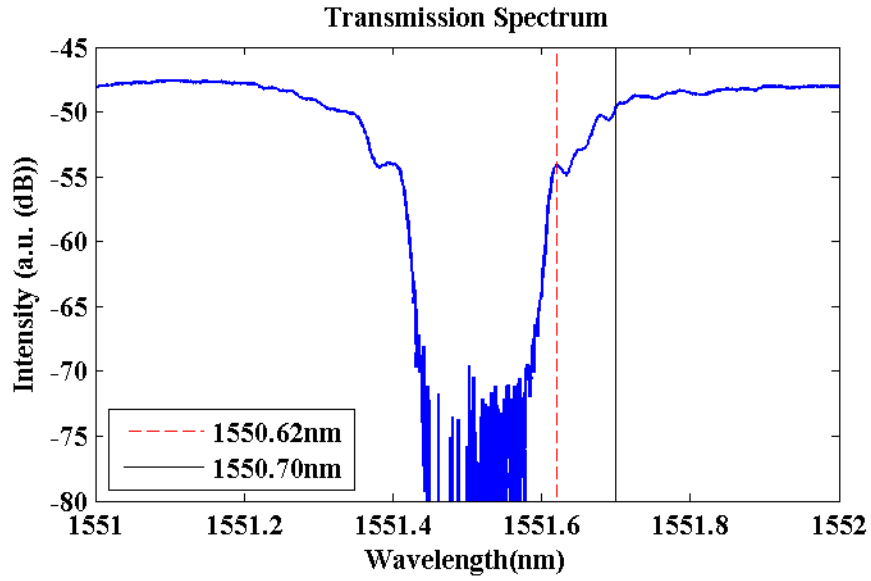


Figure 28. Probe wavelengths and the WBG bandgap.

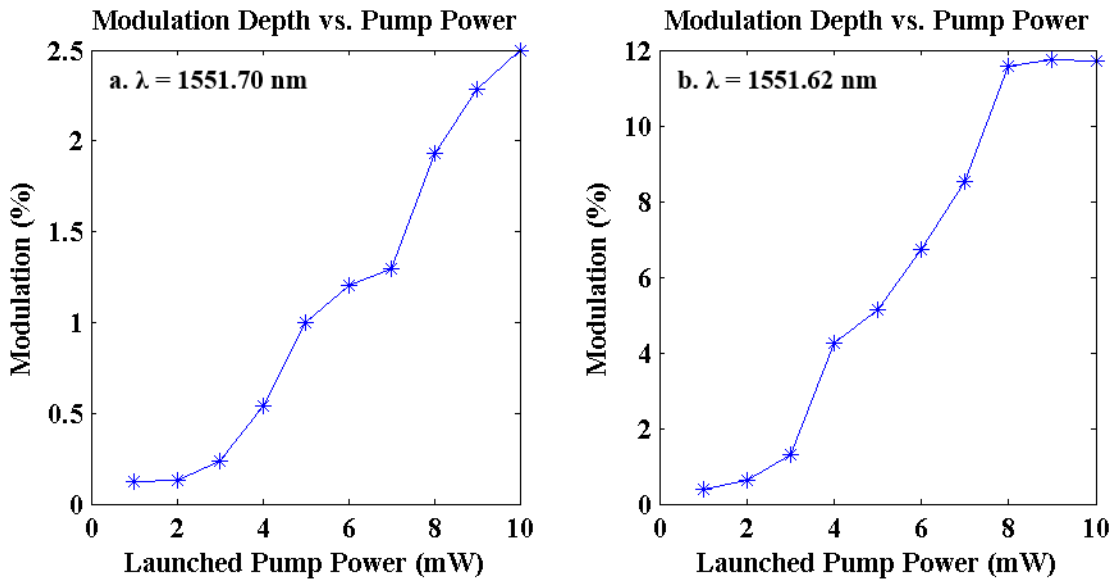


Figure 29. Modulation depths for the ‘switch-on’ and ‘switch-off’ cases.

The modulation depths for both cases are obtained by dividing the amplitude of modulated signal output and the initial output (Figure 29). In both cases, the modulation depths increases with the average pump power. The modulation response is more sensitive when the probe wavelength is close to the edge of WBG bandgap.

4.4.3 Detuning of the Signal Wavelength

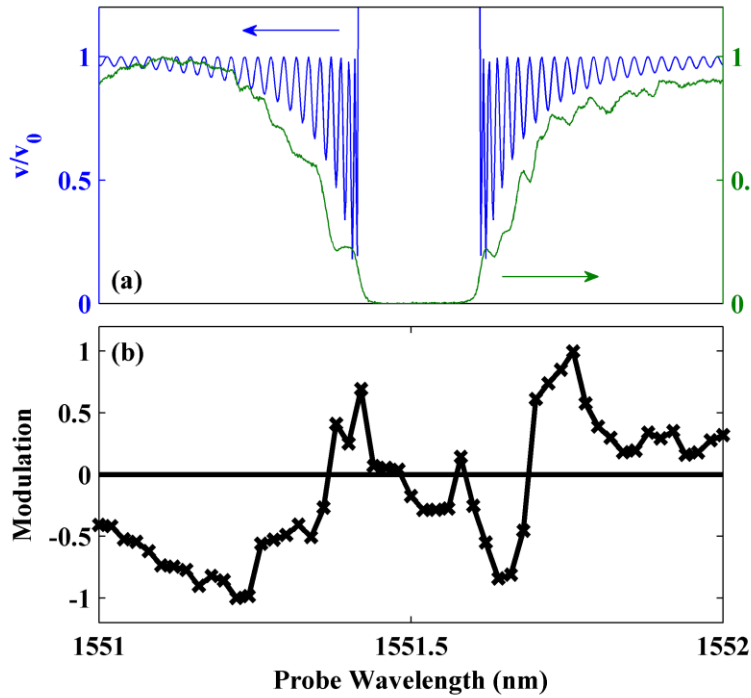


Figure 30. Dependence of modulation depth and direction on the probe wavelength.

Both the modulation depth and polarity are influenced by the initial detune of the probe wavelength, as shown in Figure 30. The pump pulse energy is set at 25 nJ, the output signals are measured with the initial detune changing from 1551 nm to 1552 nm across the bandgap of the

waveguide Bragg grating. The modulation depth are calculated at each tested wavelength. The maximum modulations are obtained at both edges of the band gap, with ‘switch-off’ operation at the red side, and ‘switch-on’ operation at the blue side. As the probe wavelength is detuned far away from the bandgap, the modulation depth decreases, and ‘switch-on’ modulation is observed at the red side, while ‘switch-off’ modulation is at the blue side. The same measurements are made with pump pulse energy at 10 nJ, 15 nJ, and 20 nJ. All four cases shows a similar trend in the transmission signal modulation with respect to initial probe wavelengths. An output signal modulation up to 12% is observed with this 2-cm long grating at pump pulse energy of 40 nJ was observed with probe wavelength at 1551.62 nm, where the static transmission is about 24.2% of the transmission of the out of bandgap signals.

As the pump pulse duration (~ 450 fs) is much smaller than the grating length (2 cm), the pump pulses modulate the output signal waveforms by inducing cross phase modulation effects that cause a frequency chirp on the probe. For a positive nonlinear refractive index n_2 as in ChG, the leading edge of the pump pulse causes a negative chirp on the probe (a red shift). When probe wavelength is far from band gap, this red shift results in an increase in group velocity of the probe signal (Figure 30(a)). Thus the probe energy is swept up onto the leading edge of the pump, appears as a temporary increase in the transmission output, as in the ‘switch-on’ operation. Similarly, at the blue side of the bandgap edge, this red shift also leads to an increase of group velocity, and hence a ‘switch-on’ operation. The modulation is reversed for probe wavelengths at the blue side far away from bandgap and at the red side of the bandgap edge, as the red shift probe leads to a decrease in group velocity, and hence a ‘switch-off’ operation.

4.5 SUMMARY

In conclusions, an ultrafast laser inscribed waveguide Bragg grating in chalcogenide glass was used for all optical nonlinear switching in a cross phase modulation setup. The ChG waveguide Bragg grating shows comparable linear performance as silica waveguide Bragg gratings, with a 22-dB strength at a 0.2-nm wide bandgap centered at 1551.51 nm. The low propagation loss and good mode confinement obtained in the highly nonlinear chalcogenide glass enables its use in all-optical switching, where output signal modulations with input of short pump pulses are achieved for both the ‘switch-on’ and the ‘switch-off’ cases, depending on the initial detune of the probe wavelength.

5.0 NONLINEAR DIRECTIONAL COUPLER

This chapter presents a nonlinear directional coupler (NLDC) written in gallium lanthanum sulfide (GLS) chalcogenide glass by ultrafast laser. The performance of the NLDC is investigated with laser pulses input in two orthogonal polarizations, and all optical switching at 1040nm between the two coupled waveguides is observed at a peak fluence of 16 GW/cm². The output spectra and the autocorrelation traces from both NLDC outputs show dominant nonlinear effects and negligible dispersion for light propagation in both channels.

5.1 INTRODUCTION

Directional coupler is an essential building block for integrated lightwave circuits. By allowing power exchange between the two adjacent parallel waveguides, basic functionalities of power division and power coupling can be realized. The functionality of directional coupler is governed by the following coupled mode equations [61],

$$\begin{aligned}\frac{dA}{dz} &= -i\kappa_{ab}Be^{i2\delta z} \\ \frac{dB}{dz} &= -i\kappa_{ba}Ae^{i2\delta z}\end{aligned}\tag{5.1}$$

$A(z), B(z)$ are the mode amplitudes in the two waveguides respectively. The coupling constants $(\kappa_{ab}, \kappa_{ba})$ form a complex conjugate pair, and describe the strength of coupling between the waveguides. 2δ is the phase mismatch given by,

$$2\delta = (\beta_a + \kappa_{aa}) - (\beta_b + \kappa_{bb}) \quad (5.2)$$

β_a, β_b are the two propagation constants of the two guiding modes, and κ_{aa}, κ_{bb} result from the dielectric perturbations to one of the waveguides due to the presence of the other waveguide and represent only a small correction to β_a, β_b .

With $|\kappa_{ab}| = |\kappa_{ba}| = \kappa$, the power distribution in two waveguides with input P_0 from only waveguide A is given by,

$$\begin{aligned} P_a(z) &= P_0 - P_b(z) \\ P_b(z) &= P_0 \frac{\kappa^2}{\kappa^2 + \delta^2} \sin^2 \left(z \sqrt{\kappa^2 + \delta^2} \right) \end{aligned} \quad (5.3)$$

The power exchange between the two waveguides varies with the coupling length z by a sine function. It is also related to the phase mismatch 2δ , and a complete power transfer is only possible when there is $2\delta = 0$, i.e. the two waveguides are symmetric and identical.

Nonlinear directional couplers (NLDC) are directional couplers where the input intensity plays a part in the power exchange between the two waveguides, by inducing the nonlinear refractive index change given by $\Delta n = n_2 I$, where n_2 is nonlinear refractive index of the material and I is the peak intensity in the waveguide. This nonlinear index change gives rise to an additional phase mismatch $d\delta$ and coupling coefficient $d\kappa$ between the waveguides, and in turn changes the power distribution. While $d\delta, d\kappa$ are both functions of coupling length, the coupled mode equations need to be solved numerically. However, in a typical configuration of

the NLDC, two identical waveguides with coupling length $L = \pi/2\kappa$, i.e., complete power transfer occurs in the linear case, the critical power required for switching is given by [72],

$$P_c = \kappa S \frac{\lambda n_0 c}{2\pi^2 n_2} \quad (5.4)$$

where S is the cross-section area of the waveguide, λ is the wavelength of propagating light, n_0, n_2 are the refractive and nonlinear index of the material, and c is speed of light.

As one of the key elements in the photonics circuit, NLDC is useful in a large variety of applications, such as all-optical switching [72, 73], all-optical logic gates [74], multiplexer and demultiplexer [75]. Directional couplers work in both the linear and nonlinear realms have been demonstrated in various material systems with different processing techniques [72, 73, 75-77]. Overcoming the challenges in processing highly nonlinear materials with the ultrafast laser writing technique, NLDC in chalcogenide glass substrate is demonstrated in this chapter.

5.2 NLDC WRITTEN IN CHG SUBSTRATE BY ULTRAFAST LASER

The NLDC in GLS ChG glass is written using a Coherent RegA 9000 laser system, with chirped laser pulses (1.7-ps) at 800 nm at a repetition rate of 250 kHz. An astigmatic beam shaping technique is used to spatially modify the input beam so as to write symmetric waveguides with low propagation loss in this highly nonlinear material. During the writing, the GLS sample is mounted on a three-axis motion stage (Aerotech) and translated at 1.5 mm/s in the direction orthogonal to the writing beam. With polarization parallel to the writing direction, the writing

beam has 328 nJ pulse energy, and is focused by an 80X objective (NA = 0.75) at 237 μm below the sample surface.

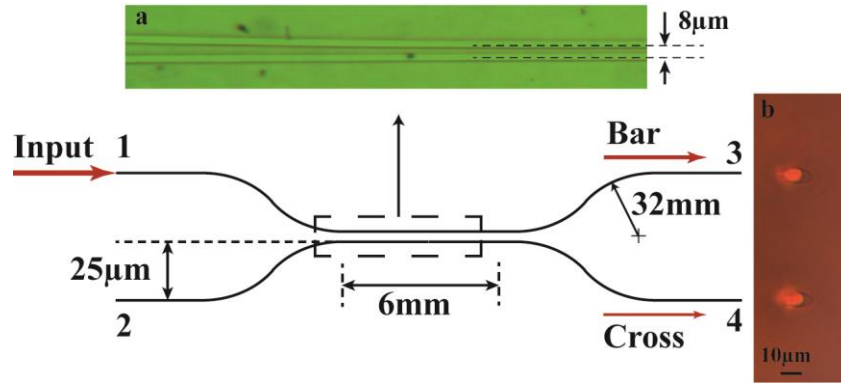


Figure 31. Schematic of the nonlinear directional coupler and microscope images of the merging region (inset (a)), and the output facet (inset (b)).

The configuration of the ChG coupler and its end facet is observed by optical microscopy. The schematic of the NLDC is shown in Figure 31, with microscope images of the merging region shown in inset (a) and the end facet shown in inset (b). The input and output facets of the sample are 10mm apart. At both facets, the input / output ports of the two coupler arms are separated by 58 μm ; in transition to the coupling region, double S-bend structures with 32 mm radius were used; the two arms are evanescently coupled at the center of the sample, where the center-to-center separation is set to 8 μm to allow maximum interaction between the two waveguides while minimizing the overlap of the modifications due to ultrafast laser writing; and the coupling length is set to 6 mm. From the microscope image of the end facets, the modified areas of both waveguides are measured to be $\sim 7.5 \mu\text{m}$ in the direction along the writing beam and $\sim 5.5 \mu\text{m}$ in the orthogonal direction.

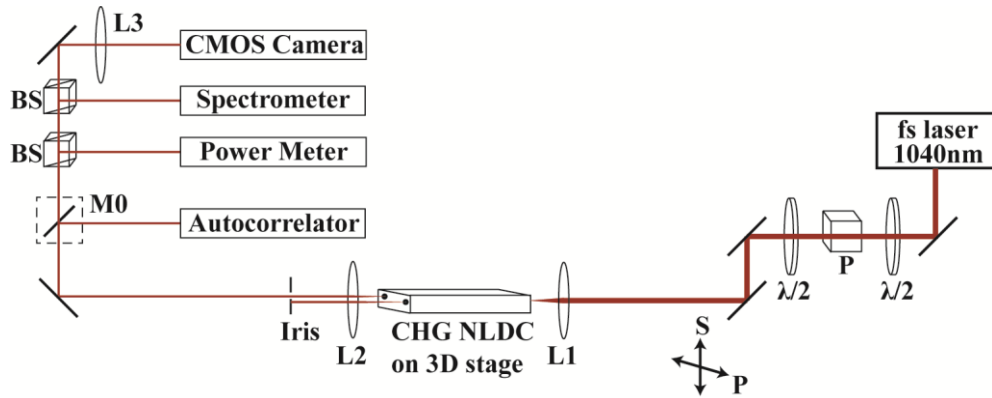


Figure 32. Schematic of the experimental setup for NLDC characterization.

The performance of the NLDC is measured using the setup in Figure 32. Before the measurements, the ChG NLDC is thermally annealed at 235 °C for an hour to prevent photoinduced effects of the material upon the input of high intensity pulses [38]. The IMPULSE™ femtosecond laser system is used in the test of the ChG NLDC. It produces laser pulses centered at 1040 nm. The repetition rate of laser pulses is 500 kHz and its pulse width is measured to be 446 fs by an autocorrelator after going through two half wave plates and a polarizer to control its power and polarization. An aspheric lens with $f = 13.86$ mm, $NA = 0.18$ is used to launch laser pulses into the coupler via one of the inputs ports. The outputs from both ports of the coupler are collected and collimated using another aspheric lens with $f = 4.51$ mm, $NA = 0.55$. One of the coupler outputs is selected to go through an iris for subsequent measurements. The selected output is split by two beam splitters and sent to a power meter, an optical spectrum analyzer (ANDO OSA AQ6315B), and imaged by a lens with $f = 300$ mm on a CMOS camera (Thorlabs DCC1240M). The selected output is also reflected by a mirror on a flip mount to an autocorrelator for pulse width measurement.

5.3 PERFORMANCE OF THE NLDC

5.3.1 Insertion Loss

As a reference, the ChG waveguides with the same writing parameters are first tested for both input polarizations. With 1.5 dB reflection loss from the input and output facets of the sample, the insertion losses for the two polarizations are similar, with 4.6 dB for p-polarized input and 4.4 dB for s-polarized input. The near field mode profiles shown in Figure 33 indicate that both p-polarized and s-polarized pulses propagate in the waveguide at the fundamental mode; the p-polarized light shows a better circular symmetry. Mode field diameters in two orthogonal directions are calculated by Gaussian fitting.

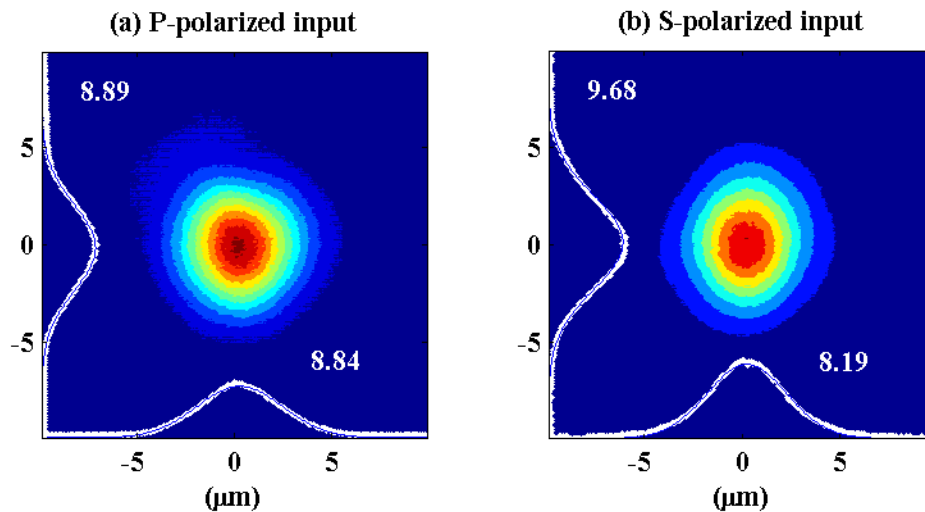


Figure 33. Mode profiles of an ultrafast laser written waveguide in GLS glass with: (a) p-polarized input; (b) s-polarized input.

The NLDC is then tested with both p-polarized and s-polarized inputs, and with laser pulses launched into port 1 and port 2, yielding four sets of experiment results. For each input polarization at low peak intensity (5 GW/cm²), the insertion loss for the NLDC is the same as that of the waveguide; the insertion loss rises to ~5.9 dB when the input peak intensity is increased to 90 GW/cm², due to nonlinear absorption of the material.

5.3.2 Nonlinear Switching

The NLDC shows the characteristic curve of nonlinear optical switching, while the switching peak intensities and splitting ratios vary among the four conditions (Figure 34).

Starting from low input peak intensity, due to linear evanescent mode coupling, the majority of input power is guided through the cross channel at this designed coupling length, until the input peak intensity reaches the switching point, where self-focusing from the Kerr nonlinearity of the material compensates the linear diffraction, and more input power is transmitted through the bar channel with the further increase of input intensity. Among the four experimental conditions, the minimum switching intensity is 16 GW/cm² for s-polarized laser pulses launched to port 1 (Figure 34 (b)). With a nonlinear refractive index up to 400 times that of silica [38], the NLDC in ChG has a switching peak intensity reduced by two orders of magnitude, comparing to the NLDC demonstrated in silica [72, 73]. The variation of the switching peak intensities and the split ratios among the four experimental conditions can be attributed to the birefringence and the asymmetry between the two waveguides, where the latter plays a major role as inferred from the resemblance between Figure 34 (a) and (b), as well as between Figure 34 (c) and (d).

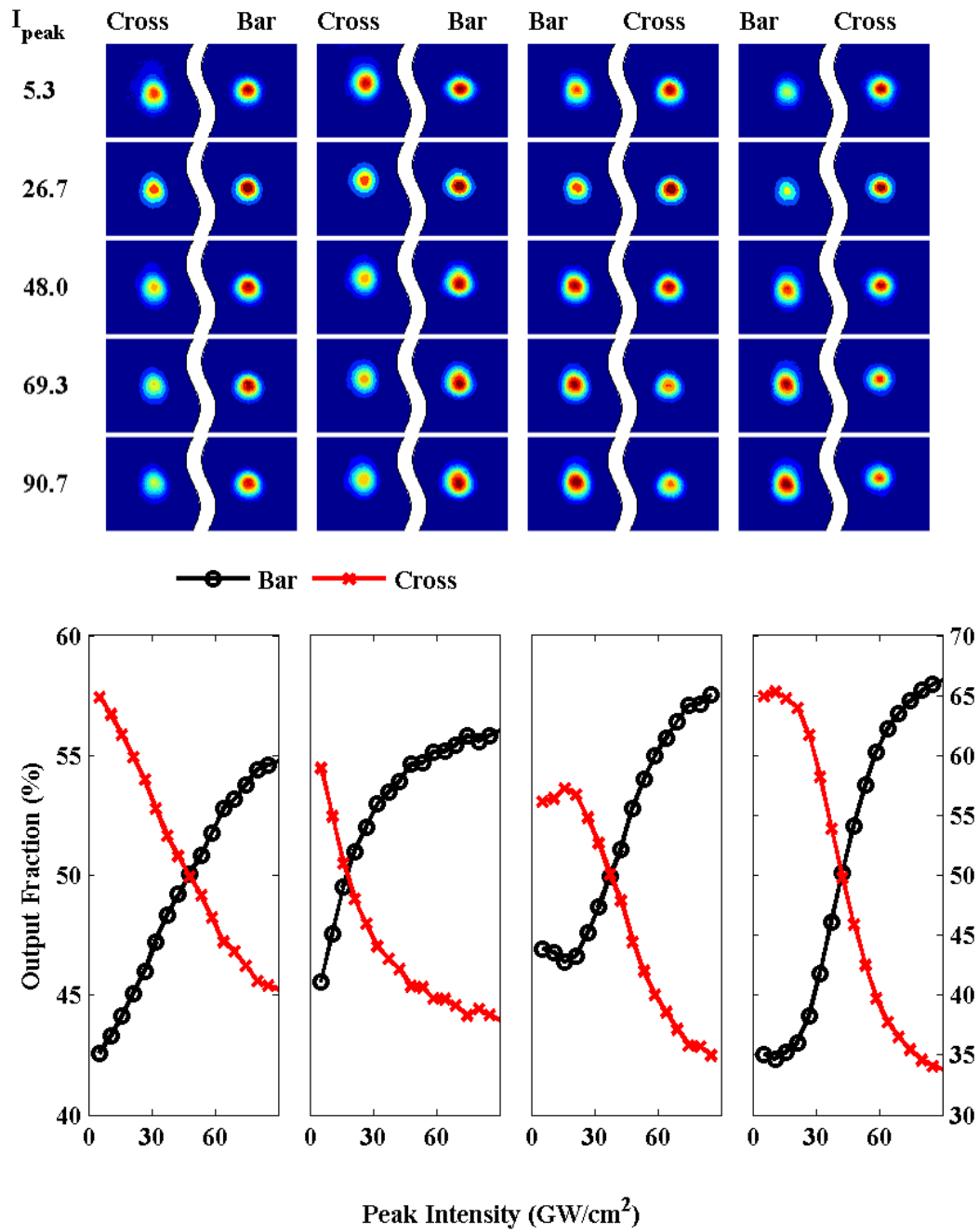


Figure 34. Output mode profiles and power switching curve for different experiment conditions: input to port 1 (a) p-polarized, (b) s-polarized; input to port 2 (c) p-polarized; (d) s-polarized.

5.3.3 Spectral and Temporal Changes

The output spectra and pulse widths of the two channels of the NLDC are also measured. Figure 30 shows the autocorrelation traces and the output spectra from both output ports of the NLDC when p-polarized pulses are coupled to port 2, corresponding to Figure 34 (c). The autocorrelation traces are measured when the input peak intensity is 90 GW/cm^2 , where the switching has occurred between the two ports and the power distribution is stabilized. In Figure 35 (a), compared to the input pulse, output pulses from both channels are stretched; the side wings are suppressed for the output pulse from the bar channel, since the center of pulse with higher intensity is confined within it while the sides with lower intensity are coupled to the cross channel; the output of the cross channel emerges as a doublet from the head and tail of the input pulse. From Figure 35 (b) and (c), propagation light from both channels experience spectral broadening. The spectral width is larger for output from the bar channel, as a larger fraction of power is transmitted through it at high input intensity. Besides, the spectral broadening is asymmetric for the output pulse from the cross channel, with more frequency components generated in the long wavelength side. This is because the switching power is related to wavelength by $P_c = \kappa S \frac{\lambda n_0 c}{2\pi^2 n_2}$. Longer wavelength components require higher switching power, thus they tend to be coupled to the cross channel while the short wavelength components are switched to the bar channel, resulting in the asymmetry of the output spectrum.

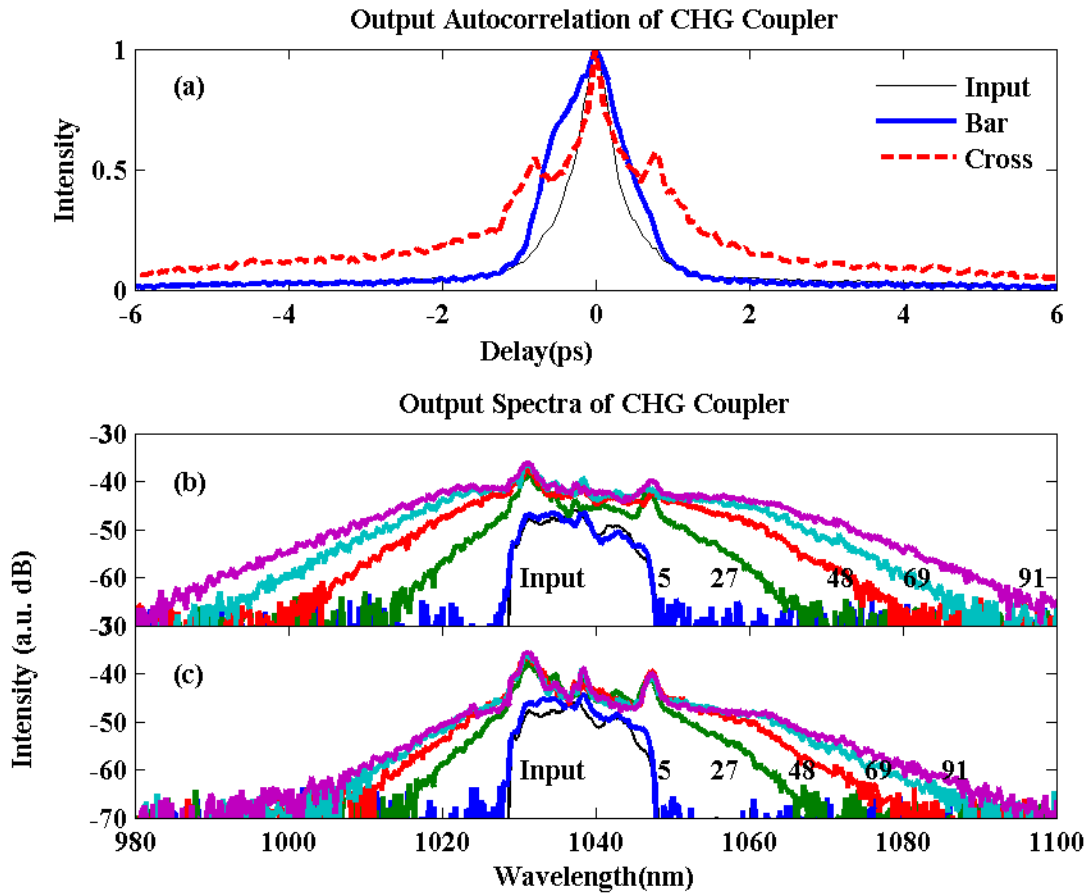


Figure 35. (a) Autocorrelation traces of the input pulse and output pulses from the two coupler channels with the peak intensity of the input being 90 GW/cm^2 . (b, c) Spectral evolution of the two coupler outputs, (b) Bar; (c) Cross. The input is p-polarized and coupled to port 2 of the NLDC. Each trace in the spectra is marked with the corresponding input peak intensity (unit: GW/cm^2).

5.4 SUMMARY

In conclusions, a nonlinear directional coupler is fabricated in gallium lanthanum sulfide chalcogenide glass by ultrafast laser. Compared to nonlinear directional coupler in silica, the ChG NLDC reported here has a reduced switching intensity of 16 GW/cm^2 . With increased input intensity, spectral width of the outputs of the NLDC is increased from 20nm to up to 140nm, while pulse stretching is insignificant for the short propagation length. The ultrafast writing parameters can be further optimized to enhance the symmetry of the NLDC so as to obtain uniform performance regardless of the input polarization or the input port.

6.0 NONLINEAR WAVEGUIDE ARRAYS

In this chapter, nonlinear optical localization in an embedded waveguide array fabricated in chalcogenide glass is presented. The array, which consists of seven waveguides with circularly symmetric cross sections, is realized by ultrafast laser writing. Light propagation in the chalcogenide waveguide array is studied with near infrared laser pulses centered at 1040 nm. The peak intensity required for nonlinear localization for the 1-cm long waveguide array was 35.1 GW/cm², using 10-nJ pulses with 300-fs pulse width, which is 70 times lower than that reported in fused silica waveguide arrays and with over 7 times shorter interaction distance. These results demonstrated that ultrafast laser writing is a viable tool to produce 3D all-optical switching waveguide circuits in chalcogenide glass.

6.1 INTRODUCTION

An important lightwave architecture for all-optical switching is to utilize spatial soliton schemes in optical waveguide arrays built in nonlinear optical substrates [78, 79]. Chalcogenide glasses (ChGs) [36, 70] are a class of important optical materials known for their large nonlinear refractive index, wide transparent wave window that spans from visible to mid-infrared, and negligible two photon absorption (TPA) and free carrier generation at the telecom wavelength. These attractive material traits lead to a large nonlinear figure of merit (FOM) for chalcogenide

glasses for all-optical signal processing applications. Kerr spatial soliton has been demonstrated in a slab ChG waveguide fabricated by thin-film deposition [80]. Moreover, a number of nonlinear waveguide devices in ChG have been realized through fabrication techniques based on thin-film deposition and various lithography schemes [39, 40, 42]. However, the current thin-film deposition and lithography techniques cannot produce multi-layer ChG waveguide structures, which are required for more complex optical interconnect architectures.

The ultrafast laser writing technique is an alternative way to fabricate waveguide structures in bulk optical substrates with proven optical properties [15]. With this technique, it is possible to form three-dimensional (3D) structures and waveguides in arbitrary arrangements [16]. This fabrication approach has been successfully applied to produce 3D waveguide array in fused silica substrates to control spatial soliton propagation [81, 82]. However, due to the small nonlinearity ($n_2 = 2.7 \times 10^{-20} \text{ m}^2/\text{W}$) in fused silica, the peak power required for nonlinear localization was reported at 1000 kW. Thus, it is highly desirable that spatial soliton waveguide arrays can be produced by ultrafast laser writing in large FOM materials such as ChGs to reduce the required intensity for switching.

Ultrafast laser writing has also been applied to waveguide fabrication in ChG. The combination of large nonlinearity and low melting point of ChG glasses leads to highly elongated and large laser modified areas [43, 66, 67], resulting in an asymmetric multi-mode waveguide cross section, large propagation loss, and poor light confinement. The multi-pass writing scheme forms ChG waveguides with improved symmetry in cross sections. However, the large waveguide cross-sections only support single mode operation at mid-infrared wavelengths [83].

In this chapter, we demonstrate a one-dimensional waveguide array formed in ChG substrate by ultrafast laser writing for spatial soliton all-optical switching. Both spatial beam shaping and temporal pulse tuning are employed to obtain optical waveguides with circularly symmetric cross sections to support single mode guiding at both 1040 nm (pump) and at the telecom wavelength [45]. Nonlinear optical localization in the waveguide array is demonstrated with over 70-fold reduction in switching intensity comparing to silica-based devices and 7.4 times shorter interaction distance, owing to the low waveguide loss (0.65 dB/cm), the large nonlinearity of the substrate material, and well-confined waveguide mode profiles.

6.2 PRINCIPLES

Light propagations in nonlinear waveguide arrays experience both linear diffraction and nonlinear self-focusing effects.

Consider a 1D array with N identical parallel waveguides. Each of these waveguides support only one confined mode, and their individual modes overlap. Hence, every waveguide in the array is evanescently coupled to its nearest neighbor, resulting in the propagation of supermodes in the array. The mode fields in each waveguide are governed by the coupled mode equations [81],

$$i \frac{dE_n}{dz} = \beta E_n + \kappa (E_{n-1} + E_{n+1}) \quad (6.1)$$

where β is the propagation constant, κ is the couple coefficient between adjacent waveguides.

When only one waveguide at the center of the array is illuminated, the input power redistributes within the array via evanescent wave coupling, resulting in power concentration at

the two sides of the array. Such diffraction in the discrete periodic structure is different from that in continuous bulk system, where most power is confined in the main lobe at the center.

When the input power launched into the waveguide is large, the nonlinear index change arises from the Kerr effect breaks the symmetry of the periodic structure. The increased index in the guiding area enhances mode confinement and hinders the evanescent wave coupling among the waveguides. When the field intensity in the waveguide arrays exceeds the threshold, the localization from nonlinear response cancels out the linear diffraction, discrete solitons (DS) are formed in the nonlinear waveguide array. In this case, the mode fields are governed by the discrete nonlinear Schrodinger equation:

$$i \frac{dE_n}{dz} = \beta E_n + \kappa (E_{n-1} + E_{n+1}) + \gamma |E_n|^2 E_n \quad (6.2)$$

where γ represents the χ_3 nonlinearity.

6.3 WAVEGUIDE ARRAY IN CHG

The substrate material used in the experiments is the arsenic-free gallium lanthanum sulfide (GLS) ChG. In the ultrafast laser writing process, a Coherent RegA 9000 laser system operated at 800 nm with a repetition rate of 250 kHz was used for the waveguide writing. By adjusting the pulse compressing grating pairs in RegA 9000, the pulse width of the laser output was tuned to 1.7 ps for optimal processing outcomes [45]. The polarization of the laser was parallel to the laser writing direction. A cylindrical telescope was used to shape the focal volume by introducing astigmatism normal to the waveguide writing direction [44]. An 80X objective (NA = 0.75) was used to focus the laser beam at 237 μm below the surface of the ChG sample. Both

the temporal adjustment of laser pulse width and the spatial control of focal volumes are critical to yield waveguide arrays with desired characteristics in terms of guided mode profiles and low propagation loss. GLS glass sample with size of $10 \times 10 \times 2 \text{ mm}^3$ were used for the waveguide inscription. A three-axis motion stage (Aerotech) was used to control the laser writing pattern. All waveguides were written at a rate of 2.4 mm/s.

A one dimensional waveguide array in ChG that consists of seven 1-cm long waveguides with a 9- μm separation is formed. Figure 36(a-b) show the microscope images of the output facet of the waveguide array and the array structure. With astigmatic beam shaping and temporal pulse tuning, symmetric waveguide cross section (Figure 36(c)) is obtained in this highly nonlinear material, while an un-shaped writing beam with transform-limited pulses at 300 fs results in an elongated waveguide cross section (Figure 36(d)).

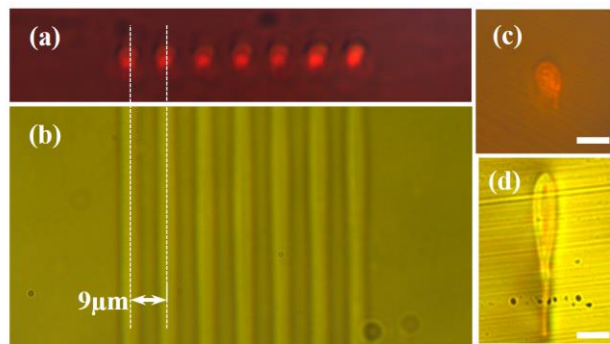


Figure 36. Microscope images of (a) the output facet of the waveguide array; (b) the top view of the array structure; (c) symmetric waveguide cross section formed with a shaped writing beam; (d) elongated waveguide cross section formed with an un-shaped writing beam. Scale bar in (c) and (d): 10 μm .

6.4 NONLINEAR OPTICAL LOCALIZATION IN WG ARRAY

6.4.1 Experiment Setup

Light propagation through the ChG waveguide array was studied using the IMPULSE™ femtosecond laser system that generates pulses centered at 1040 nm with a repetition rate of 200 kHz. The pulses are sent through a pair of parallel gratings to tune its pulse width to 300 fs. An aspheric lens with $f = 13.86$ mm, $NA = 0.18$ is used to launch laser pulses into the center waveguide in the array. The outputs from all waveguides are collected and collimated using another aspheric lens, and are imaged on a CMOS camera via a lens with 300-mm focal length.

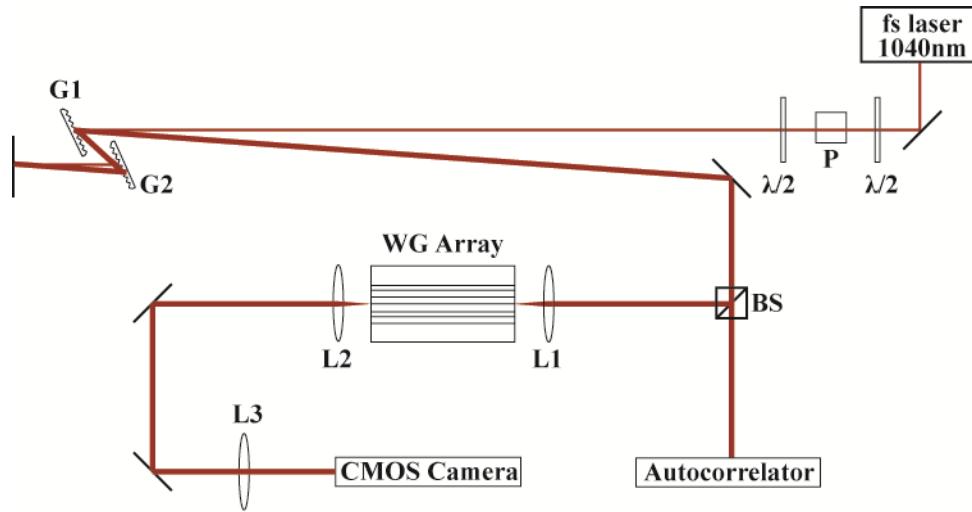


Figure 37. Schematic of the experiment setup for characterization of WG array.

As a reference, an individual waveguide is also formed using the same writing parameters, and characteristics of light propagation is first tested in this waveguide. The cross section of the waveguide is measured to be $5.9 \times 6.3 \mu\text{m}^2$, and its insertion loss and mode profile are measured for light propagation at 1040 nm. The insertion loss of the waveguide is 4.43 dB, which includes 1.5 dB reflection loss from the input and output facets of the ChG substrate, 0.65 dB propagation loss, and an estimated coupling loss of 2.28 dB. Figure 38 (a) shows its guided mode profile at 1040 nm. ChG waveguides formed with a spatially shaped writing beam at 1.7-ps pulse duration support only one confined mode. The mode field diameters ($1/e^2$ diameters) are found by Gaussian fitting of the intensity profile, with $10.46 \mu\text{m}$ along the writing beam direction, and $8.25 \mu\text{m}$ in the orthogonal direction. As a comparison, without spatial beam shaping or temporal pulse tuning, the resulted waveguide with elongated modified area (Figure 36 (d)) has two guiding areas and supports a much less confined guided mode profile, as shown in Figure 38 (b).

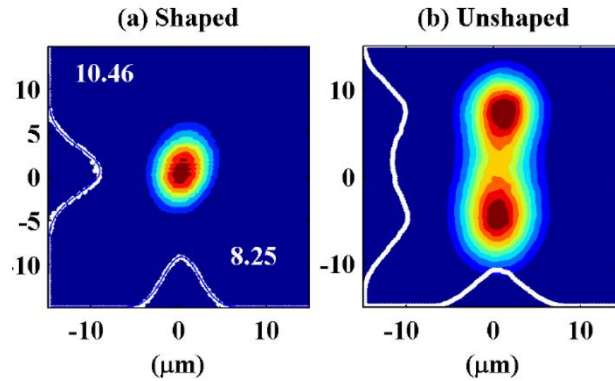


Figure 38. Guided mode profiles of an individual waveguide (a) formed with spatially shaped writing beam; (b) formed with un-shaped writing beam.

The laser pulse duration after propagation through the waveguide is also measured by a custom-built autocorrelator. The auto-correlation measurement results from an individual waveguide output are shown in Figure 39 (a) for 2-nJ and 10-nJ input pulses at 300 fs. Although the pulses experience normal group velocity dispersion (GVD) in ChG at the 1040-nm, due to the short propagation length, the laser pulses are preserved through the ChG waveguide. 12% and 40% pulse broadening were observed for 2-nJ and 10-nJ pulses, respectively. Significant frequency chirp imposed on the pulse by self-phase modulation appears to be the cause of the increased pulse broadening at higher pulse energy, which is evident in the output spectra measurements shown in Figure 39 (b).

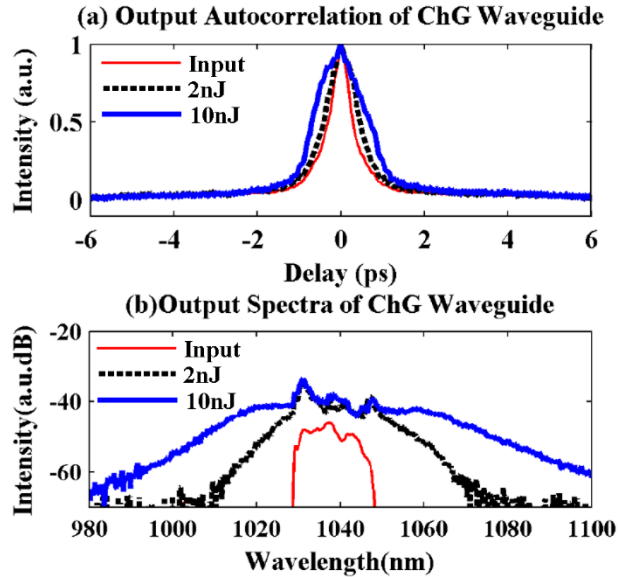


Figure 39. (a) Autocorrelation traces and (b) output spectra of individual waveguide outputs with input pulse energies of 2nJ and 10nJ.

6.4.2 Nonlinear Localization in ChG WG Array

To observe nonlinear optical localization, the pump pulses are tuned to 300 fs in width and launched into the center waveguide of the array. With the input pulse energy ranging from 1.125 nJ to 25 nJ, the output patterns of the ChG waveguide array were imaged by a CMOS camera and presented in Figure 40.

At low input pulse energies, pulse propagation through the waveguide array is dominated by linear diffraction. With only the center waveguide excited, the input power launched to the center waveguide is dissipated among the adjacent waveguides by evanescent wave coupling. The output power distribution shown in Figure 40 is slightly asymmetric about the center waveguide, probably due to writing conditions for the symmetric waveguides are not identical due to the different orders of laser writing in the fabrication process.

With the increased input pulse energy, the optical localization becomes prominent as the nonlinear self-focusing gradually overcomes the linear diffraction, as shown in Figure 40. The fractional optical power retained in the center waveguide increases from 3.8% to 44.5% when the input pulse energy changes from 1.125 nJ to 10 nJ. Considering the 40% broadening of pulse width at 10-nJ, the peak intensity for maximum nonlinear localization in the 1-cm long ChG waveguide array is estimated at 35.1 GW/cm². This is over 70-times less than the peak intensity required to achieve nonlinear localization in a 7.4-cm long waveguide array fabricated by the ultrafast laser in fused silica [81, 82].

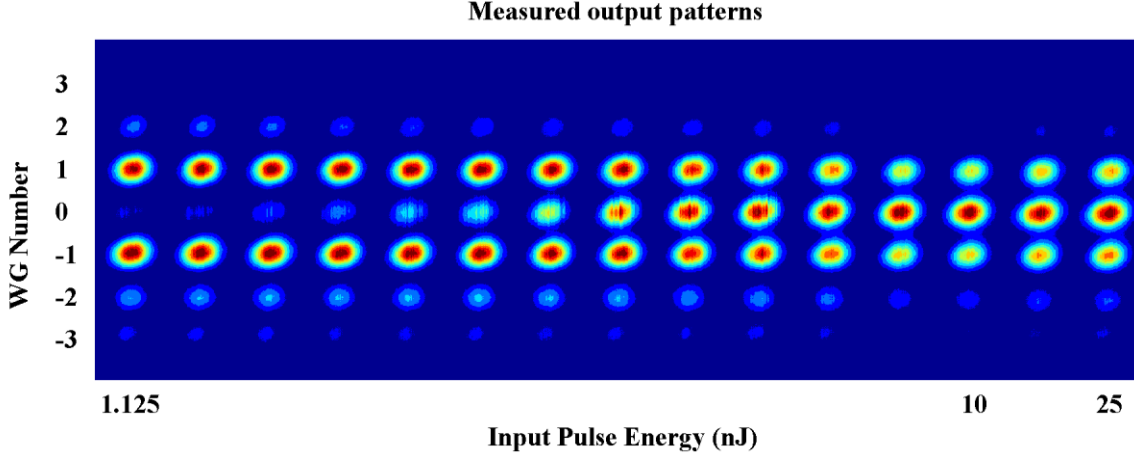


Figure 40. Measured output patterns of the ChG waveguide array with various input peak power.

6.4.3 Nonlinear Absorption in ChG WG Array

When the input pulse energy exceeds 10-nJ, the fractional optical power retained in the center waveguide starts to decrease as shown in Figure 40. This is probably due to the two-photon absorption of ChG at 1040 nm. Although negligible at 1550 nm, considerable two photon absorption in ChG is present for the 1040-nm laser pulses used in the experiment. This is confirmed by the numerical simulation shown in Figure 41.

To validate the experiment results, nonlinear optical propagation in the ChG waveguide array was numerically simulated. The evolution of the electrical field in each waveguide in the array can be described by a set of coupled mode equations [84]. With the presence of the nonlinear Kerr effect, the two-photon absorption, and the linear attenuation, the equation for the electrical field E_n in the nth waveguide can be described as,

$$idE_n / dz = \beta E_n + \kappa(E_{n+1} + E_{n-1}) + \gamma |E_n|^2 E_n - i(\alpha_1 + \alpha_2 |E_n|^2) E_n \quad (6.3)$$

where β is the propagation constant, κ is the coupling coefficient between adjacent waveguides, α_1 and α_2 are the coefficients corresponding to the linear and nonlinear waveguide loss, and γ is the nonlinear parameter that describes the Kerr nonlinearity in the waveguide. The linear attenuation $\alpha_1 = 0.65$ dB/cm, is the propagation loss in the ChG waveguide [45]. The coupling coefficient κ is 115 m^{-1} , which was determined experimentally by the output power distribution of the waveguide array in the linear propagation regime [81].

Both experimental results and simulation of the ChG waveguide array output as the function of input pulse energy are presented in Figure 41. The measured fractional powers of each waveguide output in the array are shown in Figure 41 (a) while the simulation results are shown in Figure 41 (b-c).

The purpose of the simulation is to understand why 100% nonlinear optical localization was not achieved in the experiment and the fractional optical power retained in the center waveguide decreased at higher pulse energy as shown in Figure 40. The nonlinear refractive index n_2 and two-photon absorption coefficient α_2 at 1040 nm for GLS glasses were used to best fit the experimental results shown in Figure 41 (a). The nonlinear refractive index n_2 at 1040 nm used to produce the simulation results shown in Figure 41 (b) is slightly larger than the reported value ($2.16 \times 10^{-18} \text{ m}^2/\text{W}$) measured at 1550nm [85].

Figure 41 (b-c) compare the effect of the two-photon absorption on the device performance. Simulation results shown in Figure 41 (b) were obtained using the two-photon absorption coefficient $\alpha_2 = 0.105 \text{ W}^{-1}\text{m}^{-1}$, while Figure 41 (c) shows the simulation results with no two-photon absorption ($\alpha_2 = 0$) but identical n_2 . It is clear that a complete nonlinear optical localization can be achieved at reduced input pulse energy if the two-photon absorption can be ignored. Figure 41 (b) also shows that the two-photon absorption is the cause of reduced optical

localization at high input pulse energy ($E > 10$ nJ), which is consistent with the experimental observations shown in Figure 40 and Figure 41 (a).

It is worth noting that the optical localization realized in the nonlinear ChG waveguide array is not caused by thermal optical effects. Based on the value of nonlinear refractive index of ChG inferred from the experiment results (2.16×10^{-18} m²/W), with input pulse energy at 25 nJ, the nonlinear refractive index change is estimated to be 1.9×10^{-3} . As the temperature dependence of chalcogenide glass's refractive index is 75×10^{-6} / °C [86], a local temperature change of over 25 °C would be required to result in such refractive index change. However, in the experiment, the ChG sample was placed on a passive heat sink to allow heat dissipation, and a low repetition rate at 200 kHz of the pump pulses was used to minimize heat accumulation, considering the diffusion of thermal energy is on a microsecond time scale [16]. Besides, the nonlinear ChG waveguide array was also tested with 600-fs pump pulses. Compared to using 300-fs pump pulses, about twice the average power of the pump beam was required to reach the same peak power of each pulse, and to realize nonlinear optical localization. This experiment result also corroborates that the optical localization was not a result of thermal optical effect in the ChG material.

6.5 SUMMARY

In conclusions, nonlinear optical localization is realized in a one dimensional waveguide array. Using temporal pulse tuning and spatial laser beam shaping, symmetric nonlinear waveguide arrays that preserve the large intrinsic material nonlinearity was realized by the ultrafast laser writing technique. Light propagation in the ChG waveguide array is studied with near infrared

laser pulses centered at 1040 nm. The peak intensity required to achieve the maximum nonlinear localization for the 1-cm long waveguide array was 35.1 GW/cm^2 , which is 70 times lower than that reported in fused silica waveguide arrays and with over 7 times shorter interaction distance. The comparison between the experimental results and the theoretical simulations also suggest that the waveguide array could achieve better performance at 1550 nm while two-photon absorption is negligible. Results reported in this paper demonstrated that ultrafast laser writing is a viable tool to produce 3D all-optical switching waveguide circuits in chalcogenide glasses.

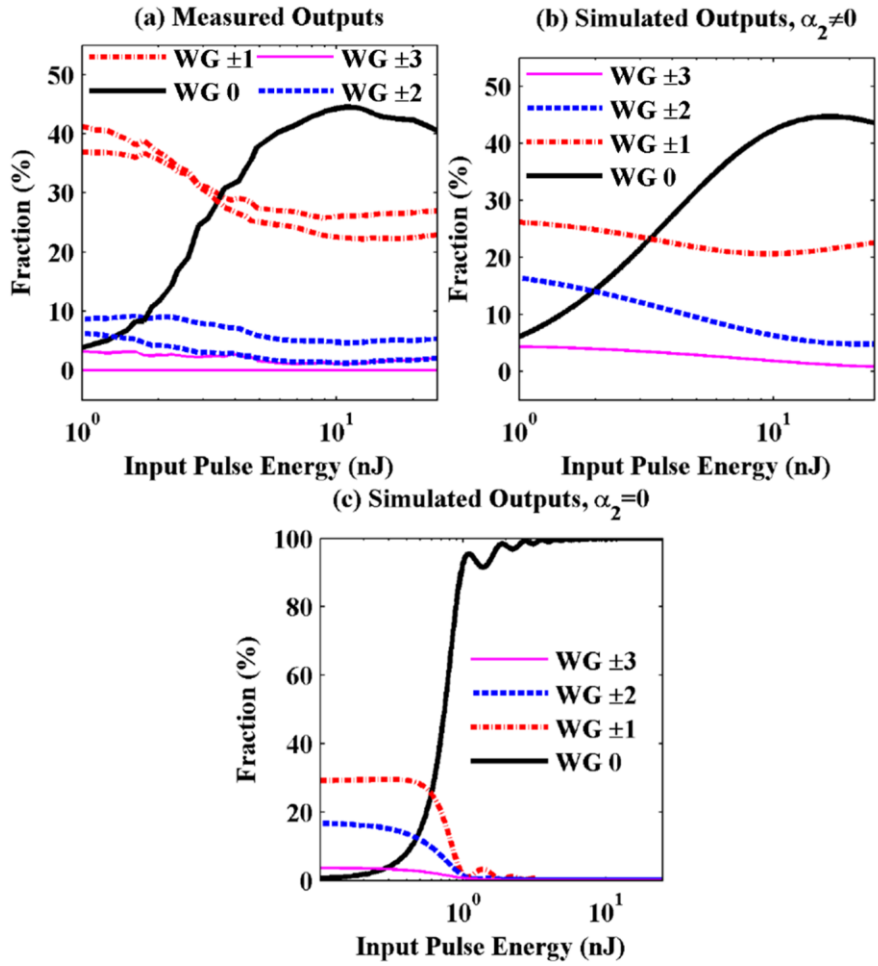


Figure 41. Fractional powers of outputs from ChG waveguide array. (a) Measured results; (b) Simulated results with two photon absorption; (c) Simulated results without two photon absorption.

7.0 CONCLUSIONS AND FUTURE WORK

The work presented in this dissertation includes the investigations on both active and passive optical components that could serve as building blocks for realization of on-chip optical network capable of high bit-rate optical signal processing and transmission.

Chapter 2 focuses on vertical cavity surface emitting laser (VCSEL) as the active optical signal source, and explores the transverse mode-locking of VCSEL. To satisfy the two requirements for mode-locking, operating conditions for VCSEL transverse modes to have equidistant spacing are found, and phase synchronization among VCSEL modes are achieved. To obtain stable pulsed emission of VCSEL with good beam quality, VCSEL cavity could be optimized to support transverse modes with similar emission intensities, and the fabrication process should be improved to guarantee the circular symmetry of VCSEL cavity.

Chapters 3 to 6 focus on nonlinear passive optical components in chalcogenide glass (ChG) substrates. In chapter 3, in consideration of the material properties of ChG and the characteristics of ultrafast laser writing, spatial beam shaping and temporal pulse tuning are utilized to allow control over the transverse geometry of ChG waveguides and hence their guiding performance.

In chapters 4 to 6, waveguide structures including waveguide Bragg gratings, nonlinear directional couplers, and nonlinear waveguide arrays have been designed in ChG substrate and fabricated by ultrafast laser writing. Nonlinear operations of the structures are numerically

simulated by solving the coupled mode equations that describe each structure. After fabrication, each of these structures are tested with their nonlinear functionalities. Fabrication simplicity is offered by the ultrafast laser writing technique, while smaller structure sizes and reduced optical power requirement for nonlinear operations are achieved due to the outstanding nonlinear properties of chalcogenide glasses.

However, the advantage of ultrafast laser writing for making 3D structures are not fully exploited. Chalcogenide glass offers superior material properties as substrates for nonlinear optical waveguide structures, but the relatively poor thermal stability causes difficulty in controlling the laser-material interaction, especially in material processing with changing depth. Meanwhile, writing power, sample translation speed, and focus depth all need to be carefully compensated when writing at different depths in the sample, so as to obtain uniform waveguide structures within the 3D structure. Therefore, a more thorough study on the laser-material interaction for ChG could help to gain better control over waveguide characteristics, as well as to enhance performance of the optical waveguide structures.

In this work, design and simulation of optical waveguide structures are based on coupled mode equations, with the assumption that uniform cross section along the waveguide. Exploiting the advantage of ultrafast laser writing, arbitrary waveguide cross section could also be obtained to accommodate the needs of structure design. And in order to account for the variation along the waveguides, finite element analysis together with beam propagation methods would be needed for structure simulations.

In the end, the work presented in this dissertation focused on the function and performance of several individual optical components, while the realization of an on-chip optical network would require integration between signal sources and passive optical components, as

well as integration among passive optical components. Optical signals can be passed along sequential components via optical interconnects, which are essentially optical waveguides, and their low insertion loss, integration compatibility, and ability to preserve signal integrity are crucial to ensure the performance of each individual component. Ultrafast laser writing makes it simple for the fabrication of photonic integrated circuit with several optical components within the sample substrate; for the connection between different substrates, it also allows flexible designs of optical interconnects and mode converters. Future work on the integration among individual optical components could further exploit the advantages of this fabrication technique and the chalcogenide glass materials.

APPENDIX A

PUBLICATIONS

A.1 PEER REVIEWED JOURNALS

1. **M. Li**, S. Huang, Q. Wang, H. Petek, and K. P. Chen, "Nonlinear Optical Localization in Embedded Chalcogenide Waveguide Arrays, " AIP Advances 4, 057120 (2014).
2. B. McMillen, **M. Li**, S. Huang, B. Zhang, and K. P. Chen, "Ultrafast laser fabrication of Bragg waveguides in chalcogenide glass," Optics Letters 39, 3579-3582 (2014).
3. **M. Li**, S. Huang, Q. Wang, H. Petek, and K. P. Chen, "Nonlinear lightwave circuits in chalcogenide glasses fabricated by ultrafast laser," Optics Letters. 39, 693-696 (2014).
4. **M. Li**, B. Zhang, K. P. Chen, D. W. Snoke, and A. P. Heberle, "Noncircular Refractive Index Profile and Breakdown of Mode Degeneracy of Vertical Cavity Surface Emitting Lasers," Quantum Electronics, IEEE Journal of 48, 1065-1068 (2012).

A.2 CONFERENCES AND PROCEEDINGS

1. S. Huang, **M. Li**, K. Chen, S. Garner, M.J. Li, "Ultrafast Laser Fabrication of 3D Photonic Components in Flexible Glasses", OFC/NFOEC 2014, San Francisco, California
2. **M. Li**, S. Huang, Q. Wang, and K. P. Chen, "Optical Switching by Nonlinear Lightwave Circuits Inscribed in Chalcogenide Glass by Ultrafast Laser," in Bragg Gratings, Photosensitivity and Poling in Glass Waveguides (BGPP) (2014)

BIBLIOGRAPHY

1. "Coriant and Allied Fiber Announce Successful 1 Terabit Super-Channel Trial" (2014), retrieved <http://www.fiercetelecom.com/press-releases/coriant-and-allied-fiber-announce-successful-1-terabit-super-channel-trial-0>.
2. Xiang Liu, Sethumadhavan Chandrasekhar, Peter Winzer, Thorsten Lotz, John Carlson, Jenny Yang, Geoffrey Cheren, and Scott Zederbaum, "1.5-Tb/s Guard-Banded Superchannel Transmission over 56x 100-km (5600-km) ULAF Using 30-Gbaud Pilot-Free OFDM-16QAM Signals with 5.75-b/s/Hz Net Spectral Efficiency," in *European Conference and Exhibition on Optical Communication*, OSA Technical Digest (online) (Optical Society of America, 2012), Th.3.C.5.
3. "Bell Labs breaks optical transmission record, 100 Petabit per second kilometer barrier" (2009), retrieved <http://phys.org/news173455192.html>.
4. "NEC and Corning achieve petabit optical transmission" (2013), retrieved <http://optics.org/news/4/1/29>.
5. "World Record One Petabit per Second Fiber Transmission over 50-km: Equivalent to Sending 5,000 HDTV Videos per Second over a Single Fiber," (2012).
6. "NEC and Corning Achieve Record-breaking Results in Optical Transmission Capacity" (2013), retrieved http://www.corning.com/opticalfiber/news_and_events/news_releases/2013/2013011501.aspx.
7. Asaf Somekh, "Use Photonics To Overcome The High-Speed Electronic Interconnect Bottleneck" (2013), retrieved <http://electronicdesign.com/design-solutions/use-photonics-overcome-high-speed-electronic-interconnect-bottleneck>.
8. G. Lifante, *Integrated photonics: fundamentals* (J. Wiley, 2003).
9. N. Kapany, *Optical Waveguides* (Elsevier Science, 2012).
10. Wolfgang Sohler, Hui Hu, Raimund Ricken, Viktor Quiring, Christoph Vannahme, Harald Herrmann, Daniel Büchter, Selim Reza, Werner Grundkäter, Sergey Orlov, Hubertus Suche, Rahman Nouroozi, and Yoohong Min, "Integrated Optical Devices in Lithium Niobate," *Opt. Photon. News* **19**, 24-31 (2008).

11. R. Nagarajan, C. H. Joyner, R. P. Schneider, J. S. Bostak, T. Butrie, A. G. Dentai, V. G. Dominic, P. W. Evans, M. Kato, M. Kauffman, D. J. H. Lambert, S. K. Mathis, A. Mathur, R. H. Miles, M. L. Mitchell, M. J. Missey, S. Murthy, A. C. Nilsson, F. H. Peters, S. C. Pennypacker, J. L. Pleumeekers, R. A. Salvatore, R. K. Schlenker, R. B. Taylor, Tsai Huan-Shang, M. F. Van Leeuwen, J. Webjorn, M. Ziari, D. Perkins, J. Singh, S. G. Grubb, M. S. Reffle, D. G. Mehuys, F. A. Kish, and D. F. Welch, "Large-scale photonic integrated circuits," *IEEE J. Sel. Topics Quantum Electron* **11**, 50-65 (2005).
12. W. Bogaerts, D. Taillaert, B. Luyssaert, P. Dumon, J. Van Campenhout, P. Bienstman, D. Van Thourhout, R. Baets, V. Wiaux, and S. Beckx, "Basic structures for photonic integrated circuits in Silicon-on-insulator," *Opt. Express* **12**, 1583-1591 (2004).
13. J. Deen and P.K. Basu, *Silicon Photonics: Fundamentals and Devices* (Wiley, 2012).
14. Alberto Politi, Martin J. Cryan, John G. Rarity, Siyuan Yu, and Jeremy L. O'Brien, "Silica-on-Silicon Waveguide Quantum Circuits," *Science* **320**, 646-649 (2008).
15. K. M. Davis, K. Miura, N. Sugimoto, and K. Hirao, "Writing waveguides in glass with a femtosecond laser," *Opt. Lett.* **21**, 1729-1731 (1996).
16. R. R. Gattass and E. Mazur, "Femtosecond laser micromachining in transparent materials," *Nat. Photon.* **2**, 219-225 (2008).
17. Masaki Kato, Radhakrishnan Nagarajan, Jacco Pleumeekers, Peter Evans, Arnold Chen, Atul Mathur, Andrew Dentai, Sheila Hurtt, Damien Lambert, Prashant Chavarkar, Mark Missey, Johan B äck, Ranjani Muthiah, Sanjeev Murthy, Randal Salvatore, Charles Joyner, Jon Rossi, Richard Schneider, Mehrdad Ziari, Fred Kish, and David Welch, "40-Channel Transmitter and Receiver Photonic Integrated Circuits Operating at a per Channel Data Rate 12.5Gbit/s," in *Optical Fiber Communication Conference and Exposition and The National Fiber Optic Engineers Conference*, OSA Technical Digest Series (CD) (Optical Society of America, 2007), JThA89.
18. E. Murphy, "The semiconductor laser enabling optical communication," *Nat. Photon.* **4**, 287-287 (2010).
19. Henryk Temkin Carl W. Wilmsen, Larry A. Coldren, *Vertical-Cavity Surface-Emitting Lasers: Design, Fabrication, Characterization, and Applications*, 1 ed., Cambridge Studies in Modern Optics (Cambridge University Press, 2001).
20. Chia-Chi Lin, Yu-Chieh Chi, Hao-Chung Kuo, Peng-Chun Peng, Connie J. Chang-Hasnain, and Gong-Ru Lin, "Beyond-Bandwidth Electrical Pulse Modulation of a TO-Can Packaged VCSEL for 10 Gbit/s Injection-Locked NRZ-to-RZ Transmission," *J. Lightwave Technol.* **29**, 830-841 (2011).

21. M. Muller, W. Hofmann, G. Bohm, and M. C. Amann, "Short-Cavity Long-Wavelength VCSELs With Modulation Bandwidths in Excess of 15 GHz," *Photonics Technology Letters, IEEE* **21**, 1615-1617 (2009).
22. P. Westbergh, J. S. Gustavsson, Ko, x, B. gel, A. Haglund, A. Larsson, A. Mutig, A. Nadtochiy, D. Bimberg, and A. Joel, "40 Gbit/s error-free operation of oxide-confined 850 nm VCSEL," *Electronics Letters* **46**, 1014-1016 (2010).
23. P. Westbergh, R. Safaisini, E. Haglund, Ko, x, B. gel, J. S. Gustavsson, A. Larsson, M. Geen, R. Lawrence, and A. Joel, "High-speed 850 nm VCSELs with 28 GHz modulation bandwidth operating error-free up to 44 Gbit/s," *Electronics Letters* **48**, 1145-1147 (2012).
24. Y. Satuby and M. Orenstein, "Limits of the modulation response of a single-mode proton implanted VCSEL," *Photonics Technology Letters, IEEE* **10**, 760-762 (1998).
25. Kenichiro Yashiki, Naofumi Suzuki, Kimiyoshi Fukatsu, Takayoshi Anan, Hiroshi Hatakeyama, and Masayoshi Tsuji, "1.1- μ m-Range Tunnel Junction VCSELs with 27-GHz Relaxation Oscillation Frequency," in *OSA Technical Digest Series (CD)* (Optical Society of America, 2007), OMK1.
26. E. S. Bjorlin, J. Geske, M. Mehta, J. Piprek, and J. E. Bowers, "Temperature dependence of the relaxation resonance frequency of long-wavelength vertical-cavity lasers," *Photonics Technology Letters, IEEE* **17**, 944-946 (2005).
27. R. Gordon, A. P. Heberle, and J. R. A. Cleaver, "Transverse mode-locking in microcavity lasers," *Applied Physics Letters* **81**, 4523-4525 (2002).
28. G. Ronald Hadley, "Effective index model for vertical-cavity surface-emitting lasers," *Opt. Lett.* **20**, 1483-1485 (1995).
29. P. Debernardi, G. P. Bava, C. Degen, I. Fischer, and W. Elsasser, "Influence of anisotropies on transverse modes in oxide-confined VCSELs," *Quantum Electronics, IEEE Journal of* **38**, 73-84 (2002).
30. A. Yariv and P. Yeh, *Optical Waves in Crystals: Propagation and Control of Laser Radiation* (Wiley, 2002).
31. M. Brunner, K. Gulden, R. Hovel, M. Moser, and M. Illegems, "Thermal lensing effects in small oxide confined vertical-cavity surface-emitting lasers," *Applied Physics Letters* **76**, 7-9 (2000).
32. M. Dabbicco, V. Spagnolo, M. Ferrara, and G. Scamarcio, "Experimental determination of the temperature distribution in trench-confined oxide vertical-cavity surface-emitting lasers," *Quantum Electronics, IEEE Journal of* **39**, 701-707 (2003).

33. S. F. Pereira, M. B. Willemsen, M. P. van Exter, and J. P. Woerdman, "Pinning of daisy modes in optically pumped vertical-cavity surface-emitting lasers," *Appl. Phys. Lett.* **73**, 2239-2241 (1998).
34. R. Gordon, A. P. Heberle, A. J. Ramsay, and J. R. A. Cleaver, "Experimental coherent control of lasers," *Physical Review A* **65**, 051803 (2002).
35. C. Quemard, F. Smektala, V. Couderc, A. Barthelemy, and J. Lucas, "Chalcogenide glasses with high nonlinear optical properties for telecommunications," *J. Phys. Chem. Solids* **62**, 1435-1440 (2001).
36. Benjamin J. Eggleton, Barry Luther-Davies, and Kathleen Richardson, "Chalcogenide photonics," *Nat. Photon.* **5**, 141-148 (2011).
37. A. Zakery and S.R. Elliott, *Optical Nonlinearities in Chalcogenide Glasses and Their Applications* (Springer, 2007).
38. A. Zakery and S. R. Elliott, "Optical properties and applications of chalcogenide glasses: a review," *J. Non-Cryst. Solids* **330**, 1-12 (2003).
39. S. J. Madden, D. Y. Choi, D. A. Bulla, A. V. Rode, B. Luther-Davies, V. G. Ta'eed, M. D. Pelusi, and B. J. Eggleton, "Long, low loss etched As₂S₃ chalcogenide waveguides for all-optical signal regeneration," *Opt. Express* **15**, 14414-14421 (2007).
40. V. G. Ta'eed, M. Shokooh-Saremi, L. B. Fu, I. C. M. Littler, D. J. Moss, M. Rochette, B. J. Eggleton, Y. L. Ruan, and B. Luther-Davies, "Self-phase modulation-based integrated optical regeneration in chalcogenide waveguides," *IEEE J. Sel. Top. Quantum Electron.* **12**, 360-370 (2006).
41. Nathan Carlie, J. David Musgraves, Bogdan Zdyrko, Igor Luzinov, Juejun Hu, Vivek Singh, Anu Agarwal, Lionel C. Kimerling, Antonio Canciamilla, Francesco Morichetti, Andrea Melloni, and Kathleen Richardson, "Integrated chalcogenide waveguide resonators for mid-IR sensing: leveraging material properties to meet fabrication challenges," *Opt. Express* **18**, 26728-26743 (2010).
42. Michael Galili, Jing Xu, Hans C. Mulvad, Leif K. Oxenløwe, Anders T. Clausen, Palle Jeppesen, Barry Luther-Davies, Steve Madden, Andrei Rode, Duk-Yong Choi, Mark Pelusi, Feng Luan, and Benjamin J. Eggleton, "Breakthrough switching speed with an all-optical chalcogenide glass chip: 640 Gbit/s demultiplexing," *Opt. Express* **17**, 2182-2187 (2009).
43. M. Hughes, W. Yang, and D. Hewak, "Fabrication and characterization of femtosecond laser written waveguides in chalcogenide glass," *Appl. Phys. Lett.* **90**, 131113 (2007).
44. Roberto Osellame, Stefano Taccheo, Marco Marangoni, Roberta Ramponi, Paolo Laporta, Dario Polli, Sandro De Silvestri, and Giulio Cerullo, "Femtosecond writing of

- active optical waveguides with astigmatically shaped beams," *J. Opt. Soc. Am. B* **20**, 1559-1567 (2003).
45. Ben McMillen, Botao Zhang, Kevin P. Chen, Antonio Benayas, and Daniel Jaque, "Ultrafast laser fabrication of low-loss waveguides in chalcogenide glass with 0.65dB/cm loss," *Opt. Lett.* **37**, 1418-1420 (2012).
 46. G.P. Agrawal, *Nonlinear Fiber Optics* (Academic Press, 2013).
 47. A. Zakery and S.R. Elliott, *Optical Nonlinearities in Chalcogenide Glasses and their Applications* (Springer Berlin Heidelberg, 2010).
 48. Jiaren Liu, Zhiyi Zhang, Shoude Chang, Costel Flueraru, and Chander P. Grover, "Directly writing of 1-to-N optical waveguide power splitters in fused silica glass using a femtosecond laser," *Opt. Commun.* **253**, 315-319 (2005).
 49. Graham D. Marshall, Martin Ams, and Michael J. Withford, "Direct laser written waveguide-Bragg gratings in bulk fused silica," *Opt. Lett.* **31**, 2690-2691 (2006).
 50. N. D. Psaila, R. R. Thomson, H. T. Bookey, A. K. Kar, N. Chiodo, R. Osellame, G. Cerullo, A. Jha, and S. Shen, "Er:Yb-doped oxyfluoride silicate glass waveguide amplifier fabricated using femtosecond laser inscription," *Appl. Phys. Lett.* **90**, 131102-131103 (2007).
 51. W. J. Chen, S. M. Eaton, H. B. Zhang, and P. R. Herman, "Broadband directional couplers fabricated in bulk glass with high repetition rate femtosecond laser pulses," *Opt. Express* **16**, 11470-11480 (2008).
 52. F. M. Bain, A. A. Lagatsky, R. R. Thomson, N. D. Psaila, N. V. Kuleshov, A. K. Kar, W. Sibbett, and C. T. A. Brown, "Ultrafast laser inscribed Yb:KGd(WO₄)₂ and Yb:KY(WO₄)₂ channel waveguide lasers," *Opt. Express* **17**, 22417-22422 (2009).
 53. R. R. Thomson, T. A. Birks, S. G. Leon-Saval, A. K. Kar, and J. Bland-Hawthorn, "Ultrafast laser inscription of an integrated photonic lantern," *Opt. Express* **19**, 5698-5705 (2011).
 54. Chao Zhang, Ningning Dong, Jin Yang, Feng Chen, Javier R. Vázquez de Aldana, and Qingming Lu, "Channel waveguide lasers in Nd:GGG crystals fabricated by femtosecond laser inscription," *Opt. Express* **19**, 12503-12508 (2011).
 55. J. C. Ng, C. B. Li, P. R. Herman, and L. Qian, "Femtosecond laser writing of a flat-top interleaver via cascaded Mach-Zehnder interferometers," *Opt. Express* **20**, 17894-17903 (2012).

56. Limin Tong, Rafael R. Gattass, Iva Maxwell, Jonathan B. Ashcom, and Eric Mazur, "Optical loss measurements in femtosecond laser written waveguides in glass," *Opt. Commun.* **259**, 626-630 (2006).
57. S. M. Eaton, W. Chen, L. Zhang, H. Zhang, R. Iyer, J. S. Aitchison, and P. R. Herman, "Telecom-band directional coupler written with femtosecond fiber laser," *IEEE Photonics Technol. Lett.* **18**, 2174-2176 (2006).
58. Graeme Brown, Robert R. Thomson, Ajoy K. Kar, Nicholas D. Psaila, and Henry T. Bookey, "Ultrafast laser inscription of Bragg-grating waveguides using the multiscan technique," *Opt. Lett.* **37**, 491-493 (2012).
59. G. Della Valle, R. Osellame, and P. Laporta, "Micromachining of photonic devices by femtosecond laser pulses," *J. Opt. A* **11**, 013001 (2009).
60. A. Yariv, "Coupled-mode theory for guided-wave optics," *IEEE J. Quantum Electron.* **9**, 919-933 (1973).
61. A. Yariv and P. Yeh, *Photonics: Optical Electronics in Modern Communications* (Oxford University Press, Incorporated, 2007).
62. H. C. Nguyen, T. Grujic, K. Finsterbusch, E. C. Magi, Fu Libin, B. T. Kuhlmeiy, C. M. de Sterke, and B. J. Eggleton, "All-Optical Switching and Two-Photon Absorption Effects in Long-Period Gratings in As₂Se₃ Chalcogenide Fibre," in *Optical Internet, 2007 and the 2007 32nd Australian Conference on Optical Fibre Technology. COIN-ACOFT 2007. Joint International Conference on*, 2007), 1-3.
63. Irina V. Kabakova, Dan Grobnic, Stephen Mihailov, Eric C. M ägi, C. Martijn de Sterke, and Benjamin J. Eggleton, "Bragg grating-based optical switching in a bismuth-oxide fiber with strong kai(3)-nonlinearity," *Opt. Express* **19**, 5868-5873 (2011).
64. Jean-Francois Viens, Chiara Meneghini, Alain Villeneuve, Tigran V. Galstian, Emile J. Knystautas, M. A. Duguay, K. A. Richardson, and T. Cardinal, "Fabrication and Characterization of Integrated Optical Waveguides in Sulfide Chalcogenide Glasses," *J. Lightwave Technol.* **17**, 1184 (1999).
65. Haibin Zhang, Shane M. Eaton, and Peter R. Herman, "Single-step writing of Bragg grating waveguides in fused silica with an externally modulated femtosecond fiber laser," *Opt. Lett.* **32**, 2559-2561 (2007).
66. Nicholas D. Psaila, Robert R. Thomson, Henry T. Bookey, Shaoxiong Shen, Nicola Chiodo, Roberto Osellame, Giulio Cerullo, Animesh Jha, and Ajoy K. Kar, "Supercontinuum generation in an ultrafast laserinscribed chalcogenide glass waveguide," *Opt. Express* **15**, 15776-15781 (2007).

67. J. E. McCarthy, H. T. Bookey, N. D. Psaila, R. R. Thomson, and A. K. Kar, "Mid-infrared spectral broadening in an ultrafast laser inscribed gallium lanthanum sulphide waveguide," *Opt. Express* **20**, 1545-1551 (2012).
68. Neil G. R. Broderick, Domino Taverner, David J. Richardson, and Morten Ibsen, "Cross-phase modulation effects in nonlinear fiber Bragg gratings," *J. Opt. Soc. Am. B* **17**, 345-353 (2000).
69. H. Lee and G. P. Agrawal, "Nonlinear switching of optical pulses in fiber Bragg gratings," *IEEE J. Quantum Electron.* **39**, 508-515 (2003).
70. Vahid Ta'eed, Neil J. Baker, Libin Fu, Klaus Finsterbusch, Michael R. E. Lamont, David J. Moss, Hong C. Nguyen, Benjamin J. Eggleton, Duk-Yong Choi, Steve Madden, and Barry Luther-Davies, "Ultrafast all-optical chalcogenide glass photonic circuits," *Opt. Express* **15**, 9205-9221 (2007).
71. Ophélie Caulier, David Le Coq, Laurent Calvez, Eugène Bychkov, and Pascal Masselin, "Free carrier accumulation during direct laser writing in chalcogenide glass by light filamentation," *Opt. Express* **19**, 20088-20096 (2011).
72. S. R. Friberg, A. M. Weiner, Y. Silberberg, B. G. Sfez, and P. S. Smith, "Femtosecond switching in a dual-core-fiber nonlinear coupler," *Opt. Lett.* **13**, 904-906 (1988).
73. A. Betlej, S. Suntsov, K. G. Makris, L. Jankovic, D. N. Christodoulides, G. I. Stegeman, J. Fini, R. T. Bise, and J. DiGiovanni, "All-optical switching and multifrequency generation in a dual-core photonic crystal fiber," *Opt. Lett.* **31**, 1480-1482 (2006).
74. J. W. M. Menezes, W. B. de Fraga, A. C. Ferreira, K. D. A. Saboia, Afgf Filho, G. F. Guimaraes, J. R. R. Sousa, H. H. B. Rocha, and A. S. B. Sombra, "Logic gates based in two- and three-modes nonlinear optical fiber couplers," *Opt. Quantum Electron.* **39**, 1191-1206 (2007).
75. A. Villeneuve, K. Alhemyari, J. U. Kang, C. N. Ironside, J. S. Aitchison, and G. I. Stegeman, "Demonstration of all-optical demultiplexing at 1555-nm with an AlGaAs directional coupler," *Electron. Lett.* **29**, 721-722 (1993).
76. A. Villeneuve, C. C. Yang, P. G. J. Wigley, G. I. Stegeman, J. S. Aitchison, and C. N. Ironside, "Ultrafast all-optical switching in semiconductor nonlinear directional-couplers at half the band-gap," *Appl. Phys. Lett.* **61**, 147-149 (1992).
77. Y. Ruan, B. Luther-Davies, A. Rode, V. Kolev, and W. Krolikowski, "All-optical directional coupler switching in chalcogenide glass," in *Lasers and Electro-Optics Society, 2005. LEOS 2005. The 18th Annual Meeting of the IEEE*, (2005), 609-610.

78. M. Heinrich, R. Keil, F. Dreisow, A. Tünnermann, A. Szameit, and S. Nolte, "Nonlinear discrete optics in femtosecond laser-written photonic lattices," *Appl. Phys. B* **104**, 469-480 (2011).
79. Robert Keil, Matthias Heinrich, Felix Dreisow, Thomas Pertsch, Andreas Tünnermann, Stefan Nolte, Demetrios N. Christodoulides, and Alexander Szameit, "All-optical routing and switching for three-dimensional photonic circuitry," *Sci. Rep.* **1**(2011).
80. Mathieu Chauvet, Gil Fanjoux, Kien Phan Huy, Virginie Nazabal, Frédéric Charpentier, Thierry Billeton, Georges Boudebs, Michel Cathelinaud, and Simon-Pierre Gorza, "Kerr spatial solitons in chalcogenide waveguides," *Opt. Lett.* **34**, 1804-1806 (2009).
81. Alexander Szameit, Dominik Blömer, Jonas Burghoff, Thomas Schreiber, Thomas Pertsch, Stefan Nolte, Andreas Tünnermann, and Falk Lederer, "Discrete Nonlinear Localization in Femtosecond Laser Written Waveguides in Fused Silica," *Opt. Express* **13**, 10552-10557 (2005).
82. Alexander Szameit, Jonas Burghoff, Thomas Pertsch, Stefan Nolte, Andreas Tünnermann, and Falk Lederer, "Two-dimensional soliton in cubic fs laser written waveguide arrays in fused silica," *Opt. Express* **14**, 6055-6062 (2006).
83. Airán Ródenas, Guillermo Martin, Brahim Arezki, Nickolas Psaila, Gin Jose, Animesh Jha, Lucas Labadie, Pierre Kern, Ajoy Kar, and Robert Thomson, "Three-dimensional mid-infrared photonic circuits in chalcogenide glass," *Opt. Lett.* **37**, 392-394 (2012).
84. H. S. Eisenberg, Y. Silberberg, R. Morandotti, A. R. Boyd, and J. S. Aitchison, "Discrete Spatial Optical Solitons in Waveguide Arrays," *Phys. Rev. Lett.* **81**, 3383-3386 (1998).
85. J. Requejo-Isidro, A. K. Mairaj, V. Pruneri, D. W. Hewak, M. C. Netti, and J. J. Baumberg, "Self refractive non-linearities in chalcogenide based glasses," *J. Non-Cryst. Solids* **317**, 241-246 (2003).
86. "GLS Glass Data Sheet", retrieved <http://www.chgsouthampton.com/products/bulk/>.